Evolution of Microstructure, Microtexture and Mechanical Properties in Linear Friction Welded Titanium Alloys

By

Elvi C. Dalgaard

February 2011

Department of Mining and Materials Engineering

McGill University

Montreal, Canada

A thesis submitted to the

Faculty of Graduate Studies and Research

in partial fulfillment of the requirements for the degree of

Doctor of Philosophy

To Laurie, for everything. To Elisabeth, Ilana, and Jacob, for your patience and encouragement. To Marjory, Lisbeth, and Lisa for your support and your faith in me.

In memory of my father, John W. Dalgaard, who would have been prouder than anyone.

Abstract

Two titanium alloys were welded using linear friction welding (LFW) techniques. The two alloys consisted of one α + β alloy, Ti-6Al-4V, and one near-β alloy, Ti-5553. The welding conditions were varied in order to assess the effect of each parameter on the mechanical properties, microstructure, and crystallographic texture of the materials. Axial pressures from 50 MPa to 150 MPa, oscillation frequencies from 30 Hz to 110 Hz, and oscillation amplitudes from 1.5 mm to 3 mm were employed.

The linear friction welded (LFWed) samples of Ti-6Al-4V and Ti-5553 were examined using electron backscatter diffraction techniques (EBSD) to relate the texture and phase changes to the thermomechanical conditions. Characterization of the welds included analysis of the microstructural features of the weld region and thermomechanically affected zone (TMAZ) in relation to the parent material. Mechanical properties were evaluated using tensile tests and microhardness measurements.

The maximum strains and strain rates experienced by the material during LFW for each set of welding parameters were estimated based on the process parameters and the measured time of oscillation. A heat input equation was developed in order to estimate the temperature at different points in the joint and temperature measurements were made during welding to corroborate the calculated temperatures. The strains, strain rates and temperatures measured and calculated for the welding conditions employed were found to be sufficient to initiate dynamic recrystallization in both alloys. This finding is in agreement with the microstructures and textures observed in the weld centres.

The near-β Ti-5553 alloy was examined not only in the as-welded state but also in two post-weld-heat-treated (PWHT) conditions. The TMAZ and weld centre of this alloy were

weakened by welding due to the reduction of the α phase volume fraction during rapid cooling from super-transus temperatures in and near the weld. With the restoration via PWHT plus aging of the α phase fraction, the UTS's for the welded samples were restored to the literature values for the heat-treated condition of this alloy.

In addition to the two titanium alloys comprising the main focus of the study, a number of other materials were examined in the context of linear friction welding. These were: IMI-834, a near-α titanium alloy (nominally Ti-5.8Al-4Sn-3.5Zr-0.7Nb-0.5Mo-0.3Si); CMSX-4, a single crystal Ni-based superalloy (Ni-9.5Co-6.4Cr-6.4Ta-6.4W-5.6Al-2.9Re-1Ti-0.6 Mo-0.1Hf wt %); stainless steel 316L; mild steel A42; as well as dissimilar pairs aluminum alloy 6063 to commercial purity Cu and stainless steel 316L to Zr alloy Zr702. All of these materials were successfully linear friction welded after some refinement of the welding parameters.

Résumé

Deux alliages de titane ont été soudés par friction linéaire (linear friction welding - LFW). Le premier alliage, Ti-6Al-4V, est biphasé α + β, alors que le second, Ti-5553, est principalement constitué d'une phase bêta. Différentes conditions de soudage (pression axiale variant de 50 à 150 MPa, fréquence d'oscillation entre 30 et 11 Hz et amplitude d'oscillation entre 1.5 et 3 mm) ont été utilisées afin d'étudier leur effet sur les propriétés mécaniques, la microstructure ainsi que la texture des deux alliages.

Les cordons de soudure ainsi que les régions adjacentes ont été analysés par microscopie électronique, plus particulièrement au moyen de la technique de diffraction des électrons rétrodiffusés, afin de mieux comprendre l'effet qu'ont les paramètres de soudage sur la texture et la transformation de phase cristallographique. Des essais de microdureté et traction ont aussi été effectués afin de déterminer les propriétés mécaniques des soudures.

Pour chaque combinaison de paramètres de soudage, les déformations et vitesses de déformation maximales obtenues durant la soudure par friction linéaire ont été estimées à partir des conditions de soudage et des temps d'oscillation. De plus, une équation paramétrique à été développée afin d'estimer la température aux différents endroits du cordon de soudure. La validité de cette équation à été confirmée à partir de mesures de la température effectuées lors de la soudure. Les déformations, les vitesses de déformation ainsi que les températures générées durant la soudure sont suffisamment élevées pour que la microstructure recristallise dynamiquement. L'analyse des microstructures et de la texture a en effet révélé des traces évidentes de recristallisation dynamique dans les deux alliages.

Les zones centrales et TMAZ de la soudure sur l'alliage Ti-5553 sont affaiblies par la diminution du volume de la phase α qui se produit lors du refroidissement rapide suivant le soudage. L'application de traitements thermiques après le soudage permet la restauration complète de la microstructure.

Finalement, des essais de soudure par friction linéaire ont été faits sur plusieurs autres matériaux, dont IMI-834 (Ti-5.8Al-4Sn-3.5Zr-0.7Nb-0.5Mo-0.3Si), mono cristal CMSX-4, (Ni-9.5Co-6.4Cr-6.4Ta-6.4W-5.6Al-2.9Re-1Ti-0.6 Mo-0.1Hf wt %), l'acier austénitique 316L, l'acier doux A42, etc.

Acknowledgements

As any Ph.D. candidate or graduate will tell you, the task of completing a Ph.D. is a monumental one which seems at times insurmountable. It was at those times especially that I was most grateful to those mentioned in these acknowledgements. When the academic work, combined with parenting three children, performing with various musical groups, and dealing with the financial constraints of being a 40+ year old grad student with a mortgage to pay, seemed like it was simply not possible; these are the people who got me through it, one way or another.

For tireless advice, assistance, brainstorming, corrections, and of course funding, I thank my advisors, official and unofficial: Professor John J. Jonas; Dr. Priti Wanjara; Dr. Mohammad Jahazi; and Professor Steve Yue. In addition to intellectual contributions, Dr. Wanjara and Dr. Jahazi provided me with material, equipment, and technicians to help me with welding, machining, tensile testing, and metallography.

Other faculty and researchers were also invaluable in my quest for knowledge, specifically Professor Mathieu Brochu; Professor Richard Chromik; Dr. Javad Gholipour; Dr. Xinjin Cao; Professor Hugh McQueen; Dr. Lee Semiatin; Professor Raynald Gauvin; and Dr. Jonathan Cuddy.

I am extremely thankful to have had the expert technical help of Max Guérin, Xavier Pelletier, Dan Chiriac, Eric Poirier, Helen Campbell, Slawek Poplawski, and Line Mongeon. You have all given of your time and shared your expertise to help me become a better scientist.

Apart from technical help, I don't know where I would be without the constant support and help of the clerical staff in the Materials Engineering department, especially Barbara Hanley. Barbara, I'll stop asking you about that credit transfer now!

Many fellow students and colleagues have given me support, advice and assistance and kept me sane while struggling with the challenges of being a student at my age: Étienne Martin, Lan Jiang, Dina Goldbaum, Holger Strauss, Frederik Coghe, Florent Bridier, Jennifer Cocle, Kiran Kumar, Salim Brahimi, John Roumeliotis, Erol Ozbakir, Tasneem Shariff, Ahmad Chamanfar, Steve Campellone, and Constantine Petropoulos are all deserving of special mention in this regard.

Finally, and in many ways most importantly, I thank my family for their patience, their emotional support, their love, their admiration, and their belief in me. My husband Laurie, and my children Elisabeth, Ilana, and Jacob have all sacrificed to allow me to pursue this dream, and done so willingly and graciously. My mother Marjory, my aunt Elisabeth, and my sister Lisa have also been rocks of support throughout my pursuit of this goal.

Table of Contents

Table of Figures

Table of Tables

Chapter 1

1 Introduction

Titanium alloys are widely used in aerospace applications due to their high specific strength and a balance of properties that can be tailored due to the allotropic transformation from the high temperature β phase (body centered cubic structure) to the low temperature α phase (hexagonal close packed structure). This transformation occurs in most titanium alloys and allows a variety of microstructures to be achieved, ranging from equilibrium structures of α and β to a non-equilibrium martensitic structure [1]. One important application of these alloys is in the compressor section of gas turbine engines, particularly for fan blades. The operating lives of these components are affected by erosion, cracking, and foreign object damage. BLaded Integrated diSKS (BLISKs) have found increased application in aircraft engines in recent years, since it has been estimated that the component weight can be reduced by 25% over traditional mechanically joined bladed disks [2]. However, BLISK manufacture through machining of a monolithic forged billet is associated with high costs and researchers are exploring processes to manufacture and/or repair these titanium alloy compressor components. Due to the high cost of engine fan blades, development of repair techniques is of particular interest for cost reduction through the salvaging of worn components [2].

Solid state welding techniques are essential to the success of manufacturing or repairing components such as BLISKs. Weldability is a classic problem with Ti and its alloys. The metal reacts rapidly with atmospheric gases in the molten state, requiring protective gas shielding in order to join it successfully using fusion welding methods. Its low thermal conductivity leads to longer weld times for low energy density processes such as TIG welding. The long weld times and high heat inputs lead to slow cooling, requiring gas protection for an extended time to protect the highly reactive Ti. High energy density methods, such as laser welding or electron-beam welding, partially solve this problem by allowing a rapid welding cycle (heating, melting and cooling) through highly localized heat input but still require protection (gas shielding or vacuum) during the time that the weld is molten. Clearly, Ti is a prime candidate for the development and application of solid-state welding methods.

Linear friction welding (LFW) is a solid-state joining process that uses the heat generated by friction at the interface between two parts in relative motion to reduce the flow stress of the material. Once the material is sufficiently plastic, a forging force is applied and a metallurgical bond is formed between the two parts. LFW eliminates the necessity for a protective environment when welding, since the material does not reach fusion temperatures; this is especially relevant to the joining of titanium alloys, which have a strong affinity for the atmospheric gases [3]. Due to the way that heat is generated directly at the interface, an even higher energy-density than that developed in laser or electron beam welding can be achieved [4]. This high energy-density, with the low thermal conductivity of Ti and its alloys, as well as the extensive mechanical deformation imposed by the friction welding process, creates a very narrow and extensively deformed TMAZ adjacent to the weld line [5]. Within this narrow region, significant changes in the microstructure have previously been observed [6]. Also, since titanium alloys are prone to texture heterogeneity, the microstructural changes can compound the anisotropy of the mechanical properties of the weld. As the recrystallization kinetics of a LFW'ed joint are affected by the original texture, this aspect must be considered as a component of the final texture at the joint. The formability and fatigue life, both important in aerospace applications, are strongly affected by the texture anisotropy.

Early research into LFW was largely driven by the aerospace industry's interest in using it for the manufacture and repair of BLISKs. Today, the technology is being more widely recognized as an efficient joining method with minimal impact on the material properties of the joint and is being looked at for many applications in industries such as the automotive, power generation and even structural engineering [7]. LFW offers a number of unique advantages, including equivalent-to-forged metal properties, low heat input, no need for a protective atmosphere and short cycle times. In addition to its engineering advantages, LFW is also a safe technology, in that it requires no special surface preparation (hence no solvent fumes for the operator), uses no consumables such as flux or shielding gases, and does not emit any smoke or fumes. It is 'green' as well - it has been estimated that using LFW to produce tailored blanks can result in average raw material savings of 70 per cent [8].

Although β titanium alloys are not of specific interest in the manufacture of aircraft engine components, this is not to say that they are not of interest in conjunction with linear friction welding. β and near-β titanium alloys are of increasing interest in the aerospace industry due to their better formability and toughness as compared with the more common α+β Ti-6Al-4V alloy. High-strength metastable β alloys such as Ti-5553 have the potential to replace steel as the preferred material for large components such as the landing-gear truck beam on the latest generation of airframes [9].

Chapter 2

2 Literature Survey

2.1 Linear friction welding

Linear friction welding (LFW) is a solid-state joining process. It involves oscillating one part in a linear fashion against another, which is stationary. No axial symmetry is required and parts can have quite complex geometries involving curves. An LFW process was first patented in 1969 [10] and in the early 1980's, The Welding Institute (TWI) demonstrated a working LFW process for metals. A typical weld is shown in Figure 2-1.

Linear friction welding (LFW) has greatly extended the commercial usefulness of conventional frictional techniques since non-round and round parts can be joined with precise angular alignment [11]. Most LFW development so far has been motivated by the aerospace industry's need to manufacture BLISKs, which exhibit better performance and reduced weight over the traditional "fir-tree" assemblies (see Figure 2-2) [5]. However, now that the technology has matured somewhat and equipment costs are lower due to the use of more efficient power sources and stored energy concepts [12], LFW is being studied in a much wider variety of materials and applications. Studies have been performed using such materials as gamma titanium aluminides [13-15], Ni-based superalloys [16, 17], Zr and its alloys [18], Al, and steel [19-21]. LFW can also be used to join dissimilar materials such as Al to Cu [22-24], Zircaloy to stainless steel [18], or polycrystalline superalloy to single crystal superalloy [25]. This allows component parts to be optimized separately; for example, high cycle fatigue-resistant, high temperature alloys can be employed for the blade and lower cycle fatigue-resistant materials for the disk [26]. Although a substantial amount of LFW research has been funded by manufacturers, very few publications concerning this research are available in the open literature [5].

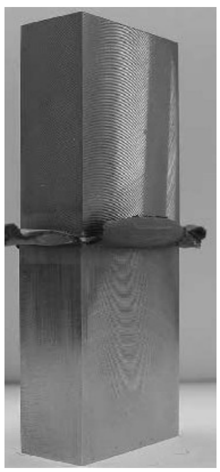

Figure 2-1: Linear friction weld of Ti-6Al-4V.[6]

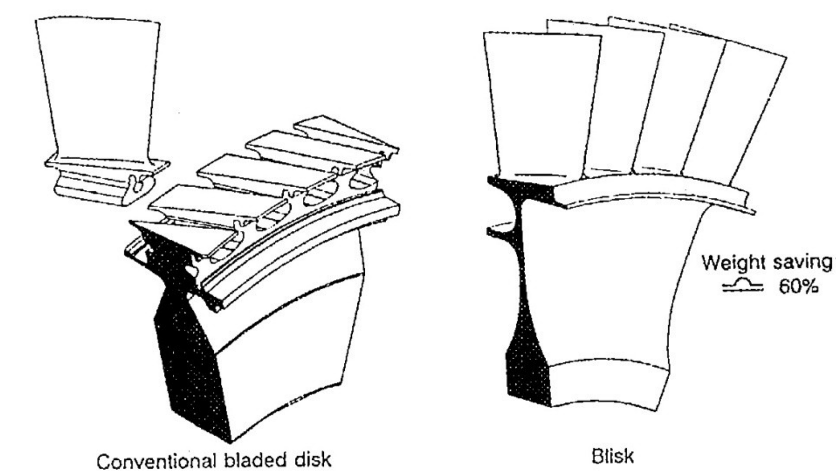

Figure 2-2: Conventionally produced bladed disk with ‘fir tree’ mechanical assembly vs. welded BLISK.[26]

2.1.1 Theory of Linear Friction Welding

Dr. A. Vairis has summarized friction welding in this elegant phrase: *"Friction welding is a solid-state process for joining materials together through intimate contact of a plasticized interface"* [27]. The material at the interface is heated by the friction produced as one component is moved relative to the other under axial pressure. Nearly all the energy expended in friction is dissipated as heat generated at the interface and the surrounding shearing material. The parts begin by undergoing dry friction and rapidly form a layer of plasticized material between the two surfaces due to microscopic local seizure and rupture. The points of contact adhere, shear and fracture and new junctions are created which are then subjected to the same process, generating additional heat [28]. The plasticized layer is effectively prevented from melting due to the nature of the process, as a liquid cannot transmit the stress required to generate heat and so no heat is generated when the material approaches this state. Instead of generating frictional heat, the material begins to behave as a lubricant. This leads to the self-regulating nature of the process [11].

A forging force applied after relative motion has stopped serves to eject most of the softened material (including any oxides or other contaminants that may have been on the surfaces before welding) and to consolidate the weld. The joint formed exhibits a narrow heat affected zone (HAZ) and features plastically deformed material adjacent to the weld in the thermomechanically affected zone (TMAZ) [27].

There are three basic varieties of friction welding [29]: rotary, orbital and linear (Figure 2-3). Rotary friction welding, often referred to as inertial welding, is the most extensively used, wherein one part is rotated as the two parts are brought together under pressure. It is used mainly for joining pipes and tubes. Orbital friction welding is characterized by its ability to weld non-circular parts. In this variation, the two components are rotated in tandem but offset to each other to create the necessary friction [27]. In linear friction welding, one part is held in a fixed position while the other reciprocates. Once frictional heating softens the interfaces, the reciprocating action stops and a forging force is applied to fuse the two parts. Linear friction welding produces a much more uniform heat generation profile than rotary friction welding over the area of the interface due to the more consistent velocity (and hence strain rate) of the parts relative to each other [30].

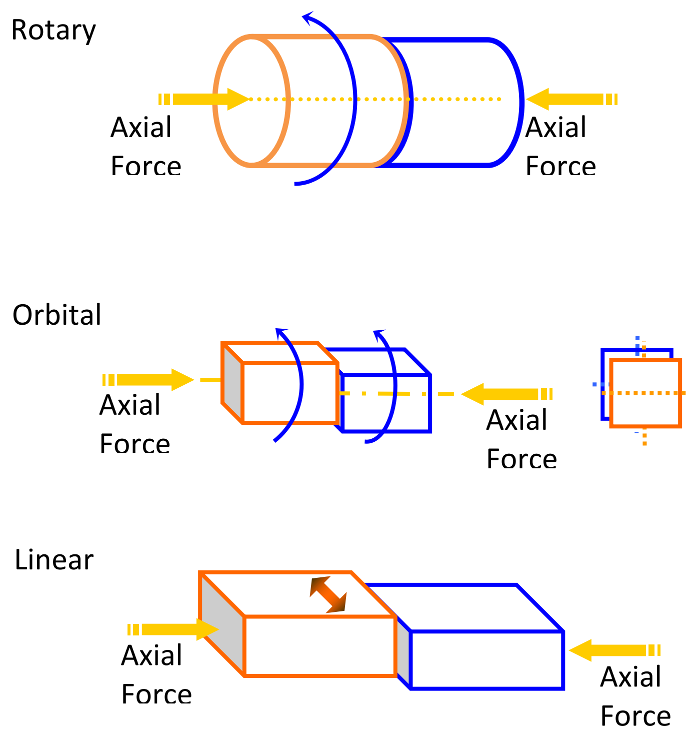

Figure 2-3: Common types of friction welding [31].

2.1.2 Phases of LFW

LFW is a self-regulating process, which is to say that specific conditions at the interface must be achieved in order for the process to continue through its phases [32]. The LFW process can be divided into four distinct phases that occur during welding (see Figure 2-4) [27]. The first phase, known as the initial or contact phase, begins with contact between the two pieces in order to initiate the wear of surface asperities. Heat is generated from the friction between the two bodies. During this phase, the true contact area between the two bodies increases as roughness is worn away [33]. The second phase, known as the transition or conditioning phase, begins when the large wear particles that were created during the first phase are extruded from the interface [34]. Frictional heat creates a plasticized region that cannot support the applied axial load and which begins to deform permanently [29].

When moving into the third phase, known as the equilibrium or burn-off phase, the flash begins to form. The axial pressure is increased and oscillation continues as in the prior phases. Frictional heat diffuses out from the interface and the plastic zone increases in size, extruding material out from the interface [27].

The last phase is known as the deceleration or forge phase, where the materials are brought to rest after the desired shortening has been attained. Once the materials have been brought to rest and aligned, the axial pressure is increased and the weld is consolidated [27].

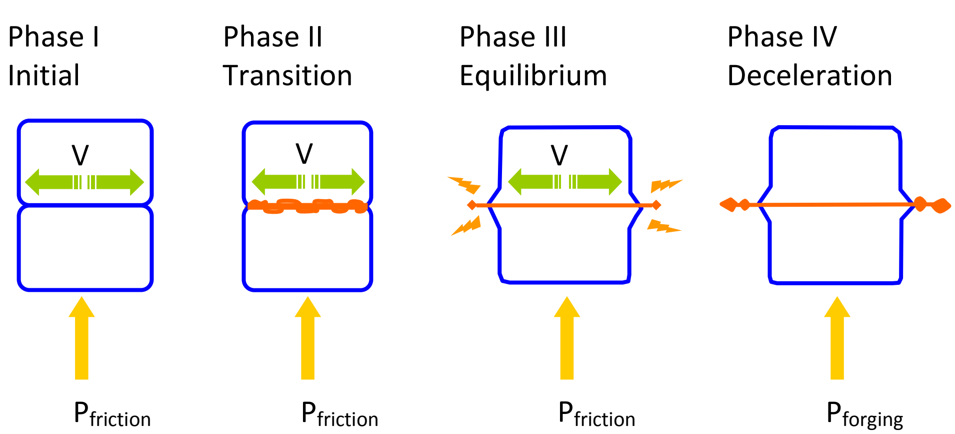

Figure 2-4: Four phases of linear friction welding [35].

The images in Figure 2-5 demonstrate an LFW process performed by TWI (The Welding Institute). The two parts are aligned at the end of the weld cycle and a forging force is applied to form the joint [10]. Figure 2-5a shows contact of the two workpieces and a spark, which is generated from the frictional pressure. This is the initial phase of the process. Figure 2-5b illustrates phases II and III, the transition and equilibrium phases respectively, where the interface becomes plasticized and the material starts to extrude as flash. The deceleration phase is shown in Figure 2-5c, where the forging pressure is applied on the workpieces and a flash protrudes around the weld.

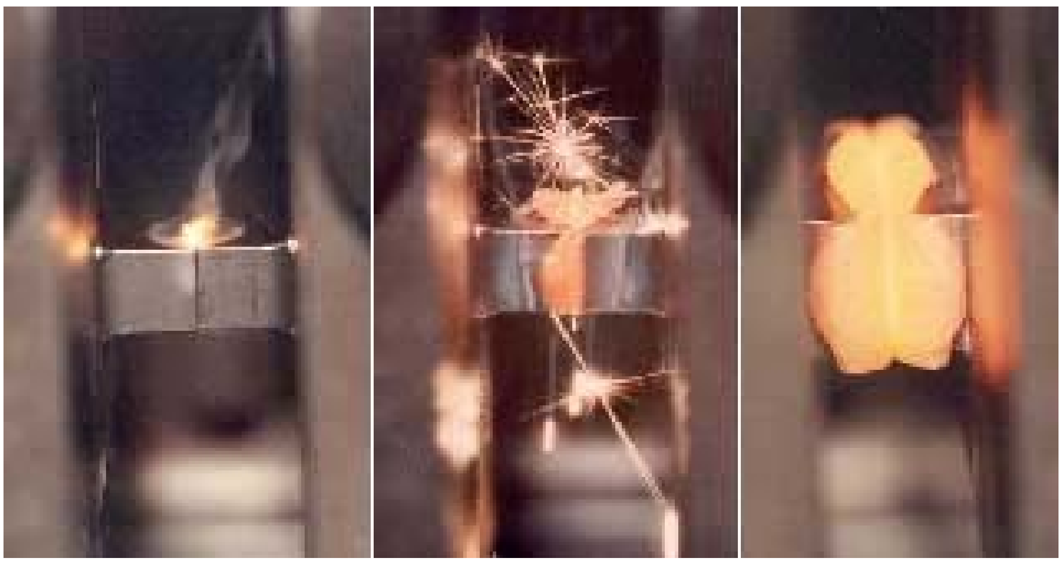

(a) Phase I (b) Phases II and III (c) Phase IV

Figure 2-5. Linear friction welding process [10]

2.1.3 Specific Power Input

Extrapolating from the self-regulating nature of the process and the physical changes that trigger phase transitions, it can be deduced that there is a specific power input minimum below which a sound weld will not be produced [6]. Hence if the critical operation limits are not achieved, due to, for example, the use of a low amplitude, a low frequency or an insufficient axial pressure, the interface will never achieve the conditions that will allow the production of a sound weld with sufficient flash [33].

The specific power input parameter (w) used to characterize the process parameters has been erroneously expressed as follows [27]:

$$w\ (\mathrm{kW/mm^2}) = a * f * P / 2\pi * \mathrm{A} \qquad \text{(Eq. 2.1)}$$

where the amplitude of oscillation (a) is measured in mm, the frequency of oscillation (f) is in Hertz, the frictional pressure (P) is in MPa, cross-sectional area (A) is in mm^2 and the units of the power input parameter (w) are kW/mm^2.

The above expression is based on combining the effective velocity, represented by amplitude times frequency, with a factor added to account for the varying velocity of the sinusoidally oscillating piece, and the pressure applied in the axial direction. The product is a value proportional to the frictionally induced power.

An amendment to the original expression has been proposed by the present author [3], as it appears that the cross-sectional area was employed twice: once in the pressure term (force divided by area) and then as the cross-sectional area itself. One of the two is sufficient.

In the current work:

$$w\ (\mathrm{kW/m^2}) = a * f * F / 2\pi * \mathrm{A} \qquad \text{(Eq. 2.2)}$$

where a,f, A are as above, and F = axial force applied in N (or $kg\cdot m/s^2$).

As predicted and as illustrated in Figure 2-6, experimental results [6] indicate that a minimum value of the specific power input seems to be necessary in order for a successful weld to be produced. This critical value has not as yet been modeled and must be determined empirically for each material (or set of materials) to be welded.

In addition, the amount of extruded material and the thickness of the TMAZ are also indications of weld integrity. Results obtained by Vairis and Frost [32] showed that successful welds with satisfactory bonding (i.e. no defects) expelled considerable flash from all sides of the joint due to the applied pressure and oscillatory movement.

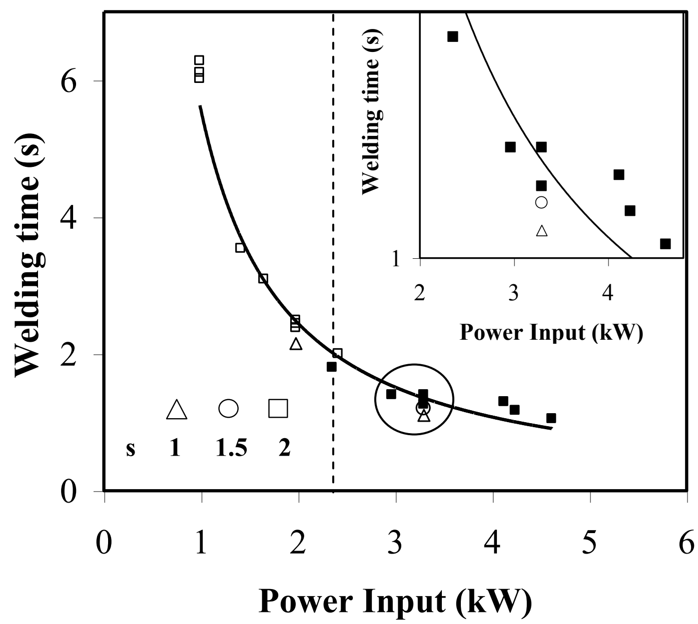

Figure 2-6: Dependence of weld success on specific power input; open markers designate unsuccessful welds [6].

In summary, LFW has several advantages over fusion welding methods, such as the possibility of joining dissimilar material [22], the elimination of the need for filler wire or shielding gas, the lack of fumes or spatter [10], and finally the fact that it is a solid state process resulting in high quality, repeatable results with a forged rather than cast microstructure. This last implies that defects associated with fusion welded (cast) structures such as pores, pinholes, shrinkage cracks, segregation, and grain coarsening can be avoided. The process does still have the disadvantage that specimen geometry is constrained by the weld chamber size and tooling available, which are not easily altered if a new configuration is required.

2.2 Titanium Alloys

Titanium alloys are ideal for applications requiring high strength, low weight, operating temperatures up to 600°C, and/or high corrosion resistance. The pseudo-binary phase diagram in Figure 2-7 shows some of the wide range of titanium alloys that have been developed. These are classified according to the phases present at room temperature, that is to say α, near-α, α + β, near-β, and β [1]. The divisions between these designations can be understood in terms of the levels of α and β stabilizers, expressed as aluminum equivalence and molybdenum equivalence (shown in Eq. 2.3 and Eq. 2.4) [36]. The specific levels can be found in Table 2-1 [37].

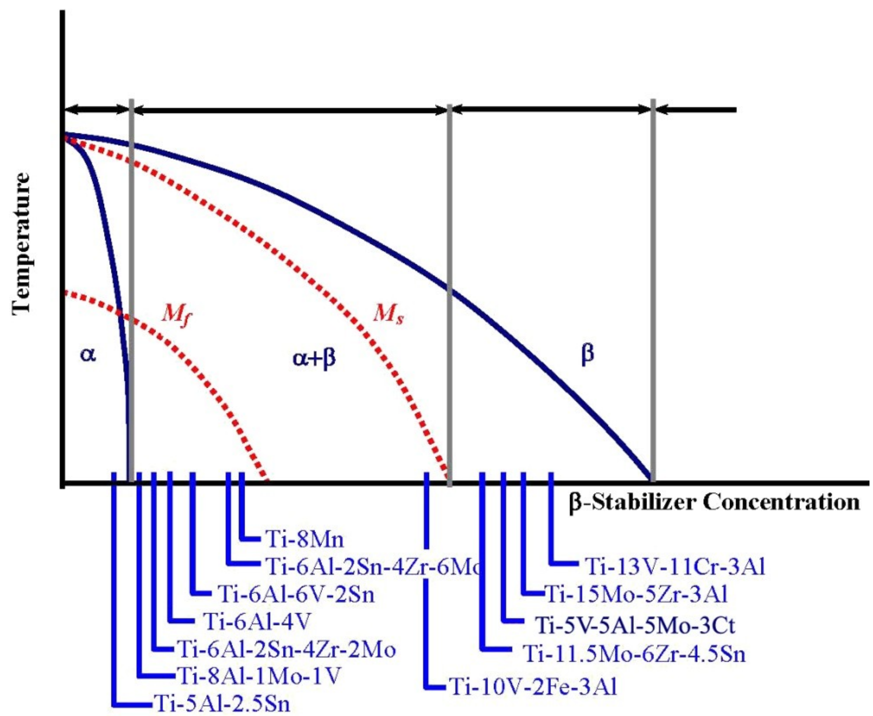

Figure 2-7: Pseudo-binary titanium phase diagram [28].

$$[Al]_{eq} = [Al] + \frac{[Zr]}{6} + \frac{[Sn]}{3} + 10[O] + 2[N] + [C]) \qquad \text{(Eq. 2.3) [36]}$$

$$[\mathrm{Mo}]_{eq} = [\mathrm{Mo}] + 0.6[\mathrm{V}] + 0.44[\mathrm{W}] + 0.28[\mathrm{Nb}] + 0.22[\mathrm{Ta}] + 1.25[\mathrm{Cr}] + 1.22[\mathrm{Ni}] + 1.7[\mathrm{Co}] + 2.5[\mathrm{Fe}] \qquad \text{(Eq. 2.4) [36]}$$

Table 2-1: Aluminum and molybdenum equivalence levels in titanium alloy types [37].

α alloys	$[Al]_{eq} < 8$ and $[Mo]_{eq} < 1$
near-α alloys	$8 < [Al]_{eq}$, 10 and $[Mo]_{eq} < 2$
α + β alloys	$5 < [Al]_{eq} < 10$ and $2 < [Mo]_{eq} < 8$
near β alloys	$[Al]_{eq} < 8$ and $10 < [Mo]_{eq} < 15$
β alloys	$[Al]_{eq} < 6$ and $15 < [Mo]_{eq}$

Due in large part to the crystal structure of the room-temperature α phase, hexagonal close-packed (HCP), titanium is highly prone to texture heterogeneity (see Figure 2-8). This results in anisotropy of the mechanical properties. The crystallographic structure and texture of titanium alloys is described in more detail in section 2.4, "Texture of Ti alloys". The recrystallization kinetics of an LFW joint may be affected by the original texture of the material, leading to microstructural changes at the joint

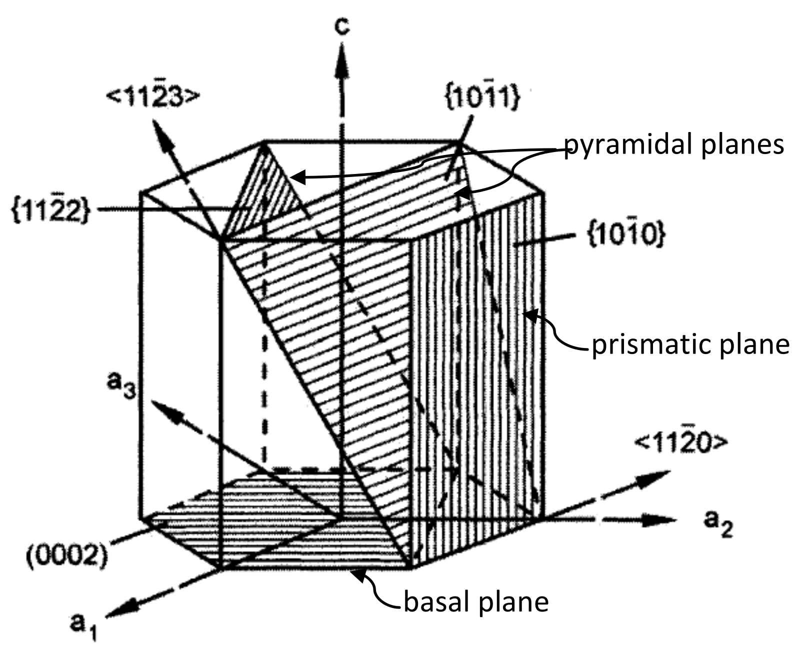

Figure 2-8: Possible slip planes in the HCP structure [38].

The formability and fatigue life, both important in aerospace applications, are also strongly affected by anisotropy. Although the dual phase nature of titanium alloys enables extensive tailoring of the properties, in general, their cost limits their application to situations where it can be justified for high performance requirements, such as for aerospace-related components.

Titanium and its alloys have a strong affinity for the atmospheric gases oxygen, nitrogen and hydrogen and thus care must be taken when welding so that the molten metal does not come into contact with them. LFW, as a solid-state process, eliminates the necessity for a protective environment when welding, since the material does not reach fusion temperatures. Due to the way that heat is generated directly at the interface in friction welding, a high heat density, comparable to that developed in laser or electron beam welding, can be achieved. This, with the low thermal conductivity of Ti and its alloys, creates a very small HAZ [26]. Friction welding processes also create a narrow and extensively deformed TMAZ adjacent to the weld zone. Accordingly, substantial microstructural and textural variations will be produced in this region [5].

Since the manufacturing cost of titanium alloys remains relatively high compared to that of other materials, such as aluminum and steel for example, maximizing the service life cycle of titanium-based components is particularly attractive. For the case of a compressor assembly, using LFW to join blades to the disk offers a cost-effective alternative to machining blade/disk assemblies from solid billets [29]. This technique is also well-suited to repair and refurbishment [39].

During the processing of titanium alloys, the allotropic transformation between α (HCP) and β (BCC) structures (and back) affords scope for microstructural manipulation via control of the phase field within which the alloy is being deformed. In particular, the α-β category of alloys has the ability to be heat treated over a wide range of temperatures. From Figure 2-7 it can be seen that the composition of an α + β alloy causes α to transform to β on heating up to the β transus temperature (about 980°C) and to then transform back to α plus transformed β at lower temperatures.

2.3 Texture of Ti alloys

Pure (i.e. α) titanium is a hexagonal close-packed (HCP) material at room temperature and has a *c/a* ratio of 1.587, slightly less than the ideal c/a ratio for a hexagonal material (which can be calculated as $c/a = \sqrt{8/3} = 1.633$) [40]. Slip can occur on the basal, prismatic, and pyramidal planes in their respective close-packed directions (see Figure 2-8 and Table 2-2). As the β transus temperature of approximately 890°C is reached, the titanium undergoes an allotropic transformation to a body-centred cubic (BCC) β phase (see Figure 2-9 and Figure 2-10). This phase is stable up to the melting point [41]. This transformation takes place more gradually in titanium alloys than in pure titanium, as can be seen in Figure 2-11, representing the percentage of β in the material at temperatures up to the transus.

Table 2-2: Slip planes in the HCP crystal structure [38].

Slip system type	Burgers vector type	Slip direction	Slip plane	Total slip systems	Independent slip systems
1	$\vec{a}$	$\langle 1\,1\,\bar{2}\,0\rangle$	$(0\,0\,0\,2)$	3	2
2	$\vec{a}$	$\langle 1\,1\,\bar{2}\,0\rangle$	$\{1\,0\,\bar{1}\,0\}$	3	2
3	$\vec{a}$	$\langle 1\,1\,\bar{2}\,0\rangle$	$\{1\,0\,\bar{1}\,1\}$	6	4
4	$\vec{c}+\vec{a}$	$\langle 1\,1\,\bar{2}\,3\rangle$	$\{1\,1\,\bar{2}\,2\}$	6	5

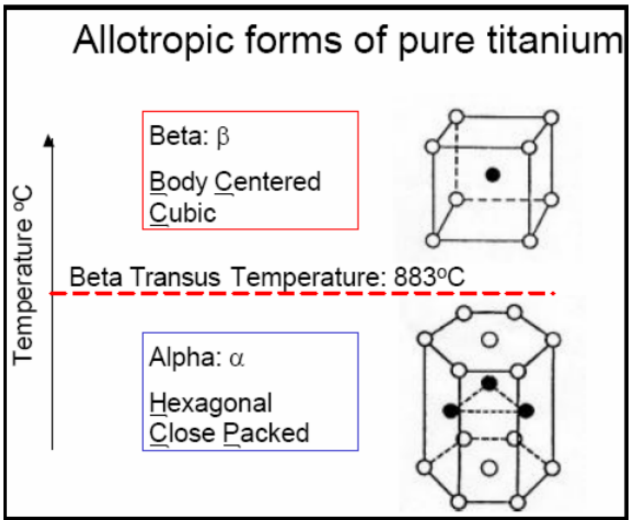

Figure 2-9: Crystallographic structure of phases in pure titanium [42]

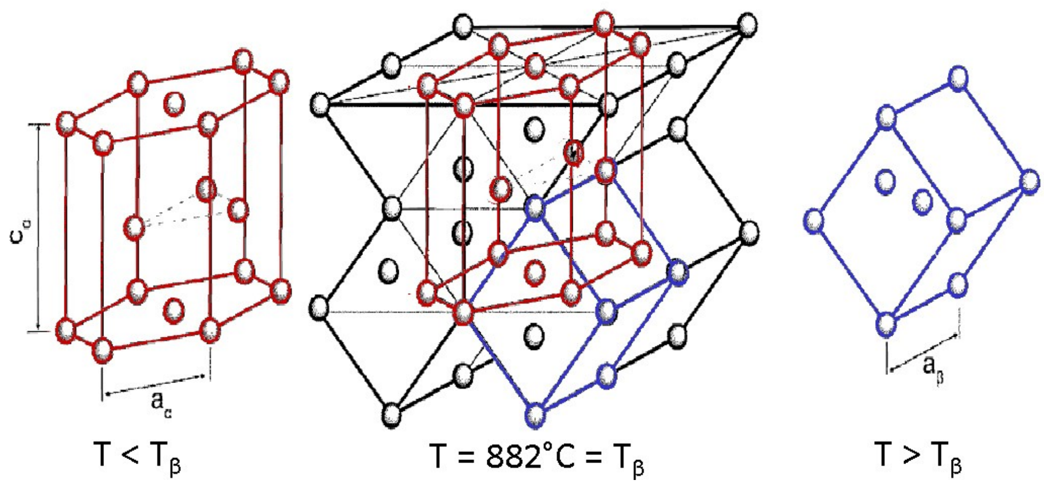

Figure 2-10; Illustration of the transformation from HCP to BCC in pure titanium [37].

The slip behaviour for the β phase is quite different, naturally. The slip planes in β titanium alloys are {110 }, {112 }, and {123 }, with Burgers vectors of the type < 111 >. This is consistent with the expected slip modes in bcc materials [38].

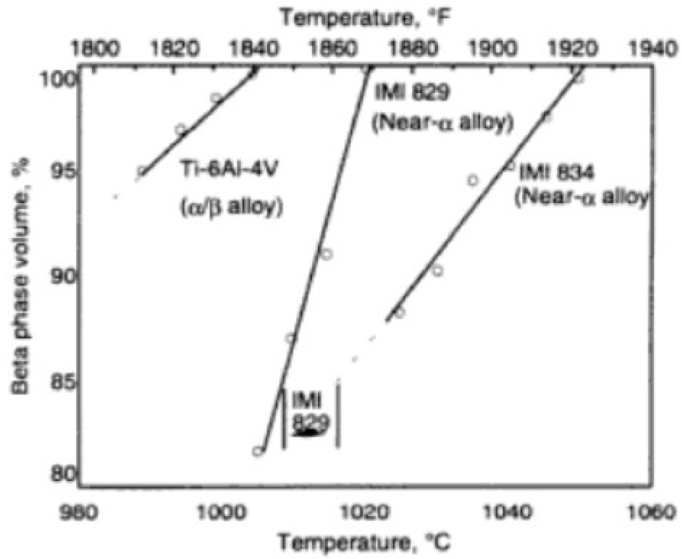

Figure 2-11: Beta transus approach curves for several Ti alloys [1].

The texture of the HCP α phase formed during decomposition of the high-temperature BCC β phase typically follows a relationship in which there are twelve variants that can form from one prior β-phase grain. The transformation texture thus formed will depend on the original texture of the β phase and on the local stress and strain fields present during cooling [43]. In titanium, the local transformation from α -> β and β -> α generally is governed by the Burgers relationships:

$(1\ 1\ 0)_{\beta}\ //\ (0\ 0\ 0\ 1)_{\alpha}$;

$[1\ \bar{1}\ 1]_{\beta}\ //\ [1\ 1\ \bar{2}\ 0]_{\alpha}$; [44]

$(\bar{1}\ 1\ 2)_{\beta}\ //\ (0\ 1\ \bar{1}\ 0)_{\alpha}$; [37]

Titanium alloys will not transform in exactly the same way as pure titanium. Any retained β phase in the room temperature structure can influence the transformation during heating [45].

In a previous study of LFWed Ti-6Al-4V, EBSD scans performed from one side of the weld interface to the other resulted in a map showing a well-defined variation of texture in the TMAZ [5]. At the weld line, a strong $\{1\ 0\ \bar{1}\ 0\}\langle 1\ 1\ \bar{2}\ 0\rangle$ transverse texture was observed both in the as-welded and post-weld heat treated condition (see Figure 2-12, Figure 2-13, and Table 2-3). Lab scale welding and full sized welding (about 12 times the size) were both performed. The specimens were analyzed and it was reported that the lab-scale welds showed a noticeable change from near-random to a strong transverse texture in the TMAZ. The full-scale welds were also characterized by a transverse texture at the weld interface; however, this was accompanied by bands of transverse and rolling texture in the TMAZ. It may be that these differences are due to the ways in which variant selection during the α->β differed between the lab-scale and the full-scale samples [5].

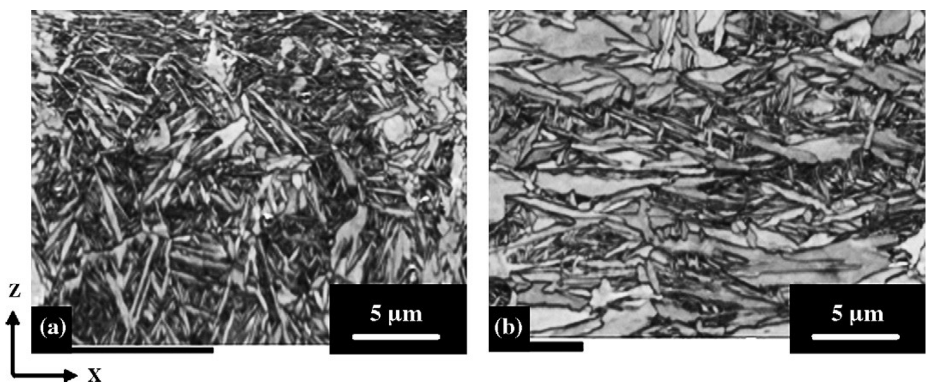

Figure 2-12: Band contrast EBSD maps showing weld zone in (a) lab-scale and (b) full-scale linear friction welded Ti-6Al-4V [5].

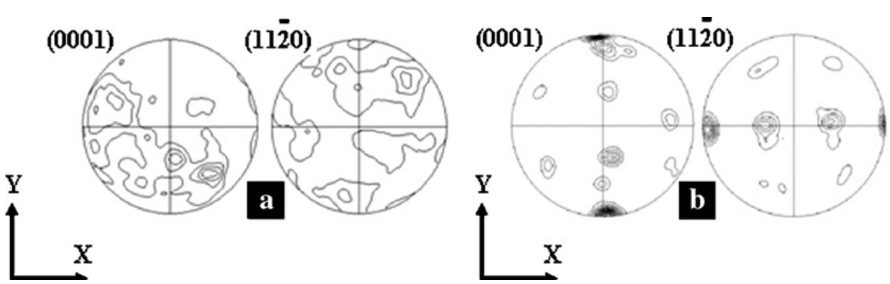

Figure 2-13 : Textures observed in Ti-6Al-4V; (a) as-received material; (b) lab-scale welded material [5].

In the work of Lütjering [46] on Ti-6Al-4V, it was found that the deformation temperature determines the texture type, as illustrated in Figure 2-14. Deformation imposed in the high α fraction temperature range (relatively low temperatures) will result in a texture based on the α phase, thus a basal/transverse texture. At higher deformation temperatures, where a high fraction of β is present, the texture that develops is based on the β phase and the transformation texture upon cooling depends on variant selection and results in a transverse (T) type of transformation texture.

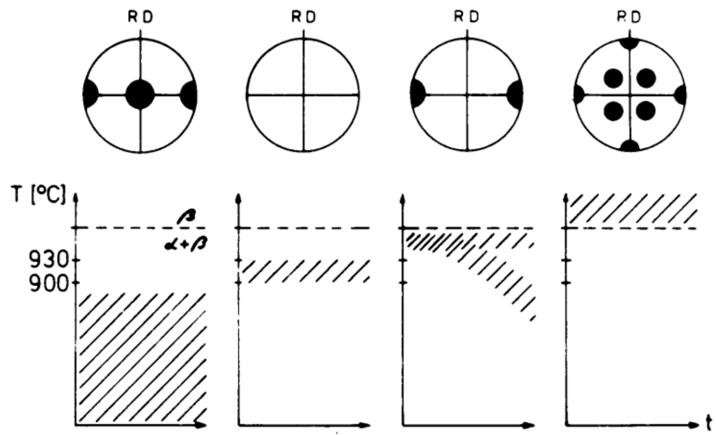

Figure 2-14 : (0002) pole figures formed in (α+β) titanium alloys at different rolling temperatures [46].

Table 2-3: Textures observed in lab- and full-scale linear friction welded Ti-6Al-4V [5].

Specimen	Location	Transverse	Rolling	Basal	R1
Lab-scale (PWHT, T_{sr}/1 h)	Weld line	36X	5X	7X	2X
	60 µm	20X	3X	5X	3X
Full-scale (PWHT, T_{sr}/1 h)	Weld line	21X	14X	4X	8X
	180 µm	18X	27X	6X	6X

Variant selection takes place during the transformation from α to β (and the reverse) within the variants called for by the Burgers relationship. If the α-to-β-to-α transformations occurred with all possible combinations of this orientation relationship, a single initial α orientation could follow 72 different paths to a final orientation.

However, the transformation paths are not equivalent, so that some final orientations predominate, while others are largely absent [47].

2.3.1 *Texture influence on deformation*

Unlike cubic materials, hexagonal materials have a small number of available slip systems with large differences in their critical resolved shear stresses (CRSS's). The strong texture in rolled Ti sheet, illustrated in Figure 2-15, results in the active slip systems being determined by the relation between the direction of the applied tensile or compressive stress and the orientations of the grains. Activity on a given slip system depends on the magnitude of the Schmid factor, given by $\sigma_s/\sigma_n = \cos\phi*\cos\lambda$, where σ_s is the shear stress on the system, σ_n is the applied tensile or compressive stress, ϕ is the angle between the stress axis and the slip plane normal and λ is the angle between the stress axis and the slip direction. Given knowledge of the strengths of the various texture components with respect to the loading direction in a given material, the Schmid factors can be readily calculated [48].

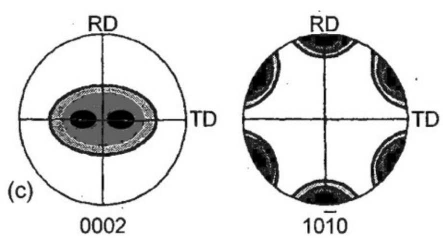

Figure 2-15: Typical rolled texture pole figures for HCP materials with c/a ratio of less than 1.6333, such as α Ti [41].

In hot-rolled titanium, the basal poles tend to lie within an angle of about 30° from the normal to the sheet, while for cold-rolled titanium the poles tend to spread along the transverse direction [48]. As a result of this texture and of the various CRSS's involved, prismatic slip has been found to dominate as the deformation mechanism in α titanium, followed by pyramidal slip. Basal slip rarely occurs. The CRSS for prismatic slip at room temperature has been reported to range from 2 MPa to 5 MPa, while that for basal CRSS has been reported to range from 8 to 11 MPa [48].

2.3.2 Ti-6Al-4V

This extensively used alloy uses aluminum to promote α stabilization for strengthening as well as a slight decrease in density, while vanadium increases the hot workability and heat treating capability by stabilizing the β phase. To date, Ti-6Al-4V is the most used of all Ti alloys, both for engine and for airframe applications [49]. This alloy is characterized by an optimum combination of properties: high strength at low temperatures and excellent machinability, while having a large processing window [1]. Ti-6Al-4V is available in forgings, sheet, and as investment castings. Much has been published on the linear friction welding of Ti-6Al-4V due to its prevalence as an aerospace alloy [3-6, 26, 27, 31, 32, 50]. According to Vairis and Frost, for Ti-6Al-4V, the minimum specific power input required to achieve sound welding conditions (the absence of defects) has been observed to increase with increasing frequency of oscillation due to strain rate sensitivity effects [27].

The morphology of the transformed β grains depends on the cooling rate, leading to a range of possible transformation structures. Upon rapid quenching, a martensitic structure forms via the diffusionless transformation of β [1]. At a lower cooling rate, there is time for diffusion to occur and the resulting microstructure develops a Widmanstätten structure, as shown in Figure 2-16. This Widmanstätten microstructure is produced through the nucleation of primary α-particles at the prior-β grain boundaries, followed by the growth of these particles into α lamellae. These lamellae have a crystallographic relationship with the parent β grain, such that the basal plane of the α phase is parallel to the |110| trace in the β [31].

As illustrated in Figure 2-16, the darker regions representing the β phase (in the optical micrographs) are left between the α plates that have formed. The final microstructure consists of plates of α delineated by the β phase between them (see Figure 2-17). The cooling rate then influences the thickness and orientation of the α plates. Cooling rates that are sufficient to produce a diffusionless transformation produce a martensitic microstructure, which is represented by α′ or α′′ depending on whether the crystal structure is hexagonally close packed or orthorhombic, respectively.

The main differentiating feature between the martensitic and Widmanstätten structures is the change in the lattice parameter of the c-axis of the HCP structure. As the cooling rates are decreased, the resulting transformation microstructures are termed basket-weave, acicular, and lamellar, respectively [1].

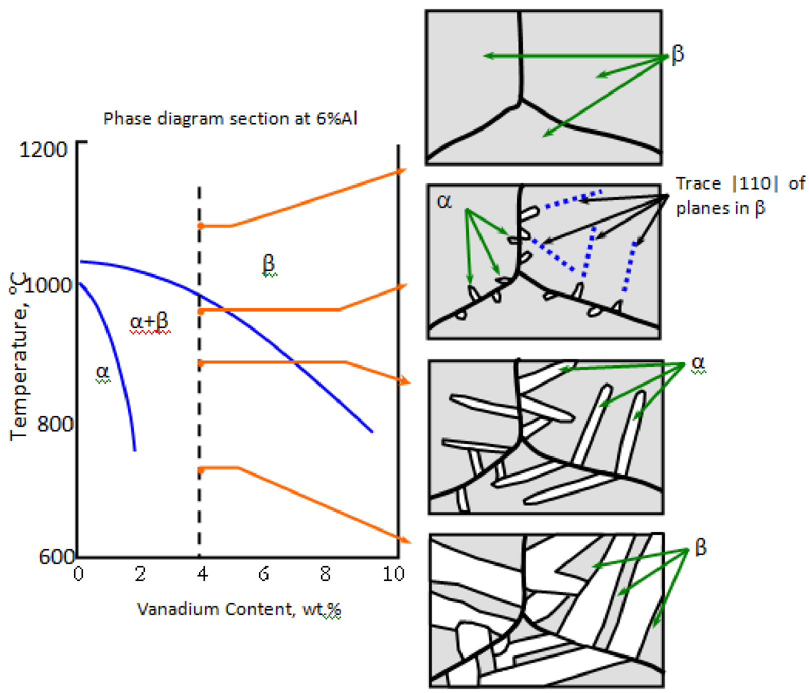

Figure 2-16: Schematic drawing showing the development of a Widmanstätten structure in an α-β alloy [23].

The practice of mill-annealing Ti-6Al-4V is used to form a bimodal microstructure with balanced mechanical properties (such as good tensile strength and fatigue resistance) by relying on grain size refinement during processing. The alloy is processed in the β phase and/or α-β phase region followed by cooling to form a martensitic (α') or Widmanstätten structure. Subsequent working and low temperature aging are applied to decompose the martensitic or Widmanstätten microstructure. The final mill-annealed bimodal microstructure consists of equiaxed or globular α grains and transformed β grains with a lamellar morphology, as illustrated in Figure 2-18.

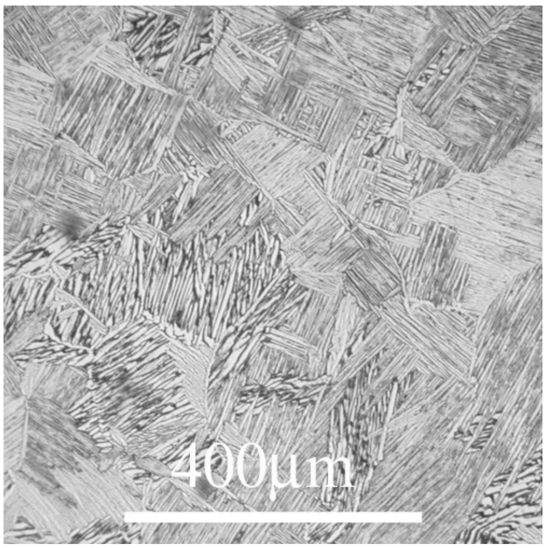

Figure 2-17: Ti6Al-4V specimen displaying Widmanstatten microstructure with α plates oriented according to β matrix [51].

Other alloys, such as Ti-6242 (6Al-2Sn-4Zr-2Mo) and Ti-6246 (6Al-2Sn-4Zr-6Mo), have higher strength and temperature capabilities. At present, the best performing Ti alloy for disk applications (up to 550° C) is IMI834 (Ti-5.8Al-4Sn-3.5Zr-0.7Nb-0.5Mo-0.35Si-0.06C) [52]. Above 450° C this alloy is superior to any other Ti alloy. However, it costs about twice as much as Ti-6Al-4V due to its complex metallurgy and the thermomechanical processes needed to optimize the microstructure and mechanical properties. In addition, due to dwell fatigue issues IMI834 is not currently used for high pressure compressor sections [53].

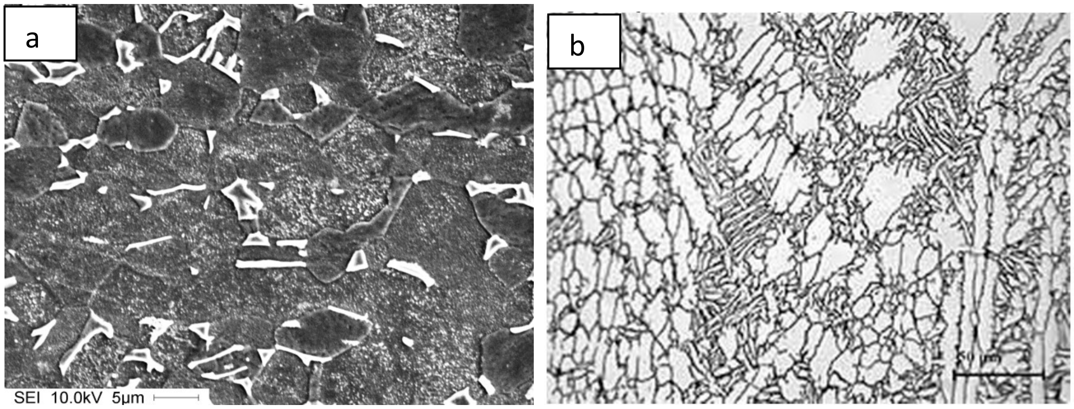

Figure 2-18. Mill annealed Ti-6Al-4V microstructures: (a) as-rolled [1] (b) forged [54].

2.3.3 Ti-5553 (near-β alloy)

Although β and near-β titanium alloys have been on the market since the 1950's, apart from the Lockheed SR-71 Blackbird military aircraft in the 1960's not much use was made of these materials until the 1980's. Once again, this was an aerospace application in the military [55]. Since that time, β Ti alloys have been of increasing interest in the aerospace industry due to titanium's high specific strength (compared to steel), low modulus of elasticity, and good corrosion resistance, as well as better formability and toughness compared to the more common α-β alloys [55]. The low modulus in particular gives Ti an enormous advantage over steel in the manufacture of springs, one of the most prevalent applications of the β alloys. As can be seen in Figure 2-19, Ti springs have a huge weight advantage over comparable steel springs [55].

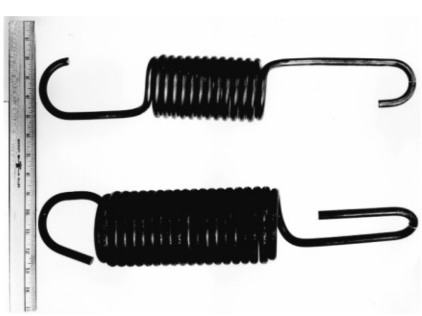

Figure 2-19: The Ti spring above carries the same load as the steel spring below. The steel spring weighs 4.35 kg, while the Ti spring weighs 1.45 kg [55].

The β and near-β alloys of titanium are not usually used in the as-forged or as-quenched condition, due to the relative weakness of a fully β grain structure even in a retained martensitic condition. In these alloys, the strength of the material depends on the shape, scale, distribution and fraction of primary α and decomposition products of the β phase [42]. Reheating below the eutectoid temperature is used to decompose the retained β into a mixture of α and β. Other decomposition products may also occur (as shown in Figure 2-20) depending on the alloy, such as $TiCr_2$ or ω, a hexagonal metastable phase. These non-β phases increase the strength of the material [56].

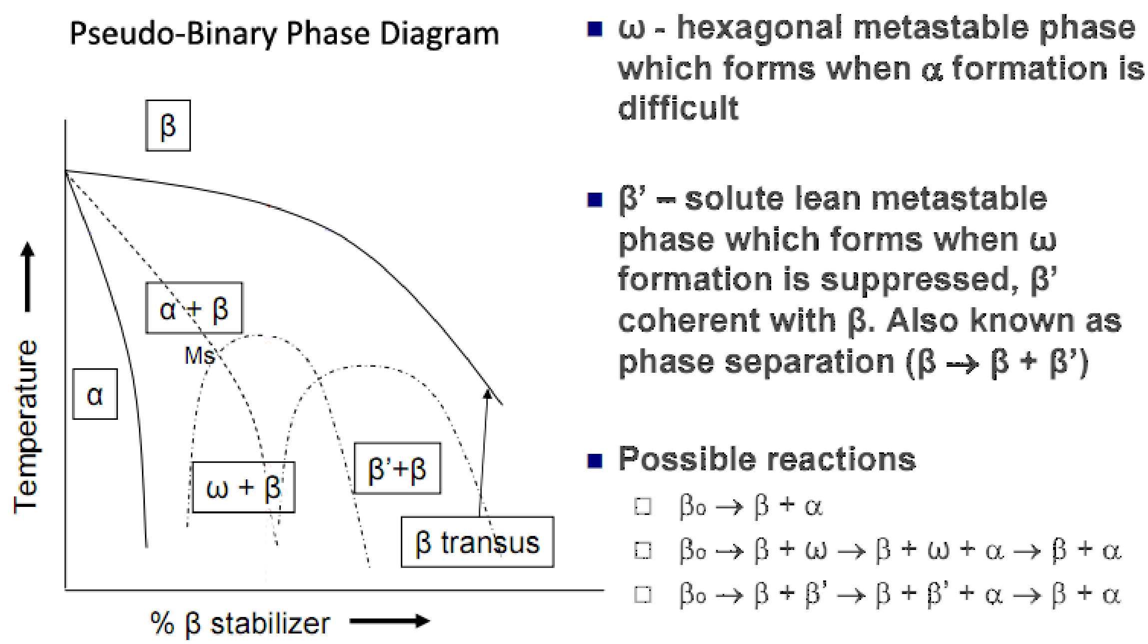

Figure 2-20: Decomposition products in β Ti alloys [42]

β Ti alloys offer the ability to heat treat sections of greater thickness than those containing higher phase fractions of the α phase. The disadvantages of this alloy system include a greater likelihood of segregation during melting than in an α-β alloy and potentially less advantageous crack growth and toughness characteristics; also, these alloys may be difficult to weld using conventional fusion joining technologies [55]. Considering these factors, solid-state joining processes have the advantage that they limit the segregation effects and also form more integral welds.

High-strength metastable β alloys, such as Ti-5553, have the potential to replace steel as the preferred material for large components such as the landing-gear truck beam on the latest generation of airframes [9]. In 1995-1996, Boeing worked with the Russian company VSMPO to develop a higher strength, lower cost alloy to replace Ti-10V-2Fe-3Al [57]. The alloy VST-5553 was the result. The North American version of the alloy, Ti-5553, was introduced in 1997 by TIMET and has a nominal composition of 5 wt% Al, 5 wt% V, 5 wt% Mo, 3 wt% Cr, with the balance being Ti. The alloy falls into the "forging alloys" subcategory of Ti near-β alloys, along with Ti-6246 (6Al-2Sn-4Zr-6Mo), Ti-10-2-3, and Ti-17 (5Al-2Sn-2Zr-4Mo-4Cr) [56]. Ti-5553 is solution treated at 28 - 66 °C below the β transus for a minimum of 30 minutes followed by cooling in air. Subsequent aging is implemented at temperatures of 566-677°C for up to 8 hours [56]. It has been shown (see Figure 2-21) that the material properties do not change significantly beyond an aging time of one hour, though α plates do thicken [42].

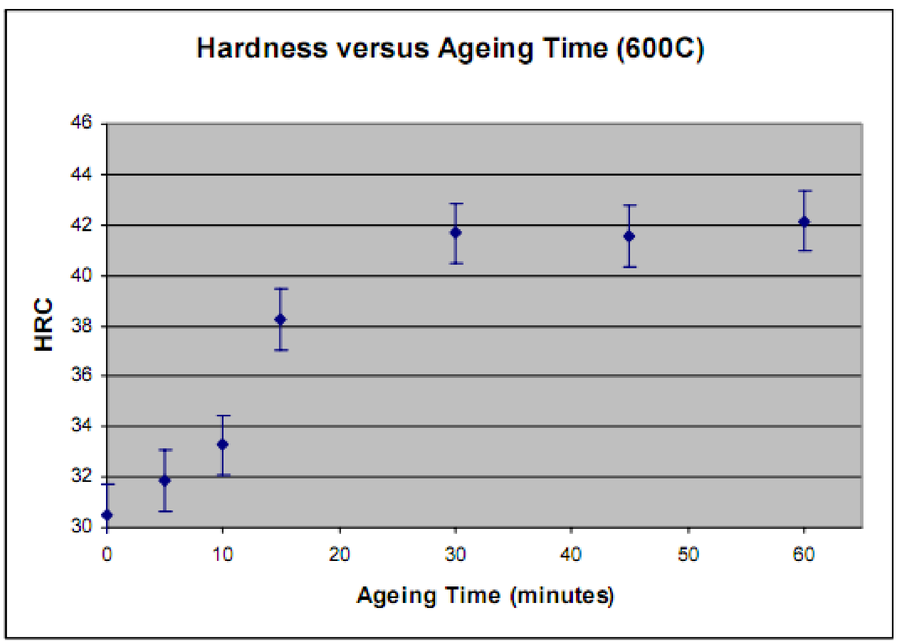

Figure 2-21: Hardness vs. aging time for alloy Ti-5553 [42].

Ti-5553 typically has a bimodal structure composed of equiaxed and lamellar grains (see Figure 2-22) but the specific microstructure of a given piece will be heavily dependent on the deformation and heat treatment history [1]. Typical physical and mechanical properties of this alloy in the solution treated and aged (STA) condition can be seen in Table 2-4. Unfortunately, industry-wide standards for the tensile properties of Ti-5553 are not available because it is currently manufactured to proprietary customer requirements [56]. The forging behaviour of Ti-5553 is similar to that of the alloy's predecessor, Ti-10-2-3, although the higher β transus temperature of the former (856°C) versus the latter (800°C) allows for higher forging temperatures [58]. Both alloys are typically used in a service environment of up to 315°C [56].

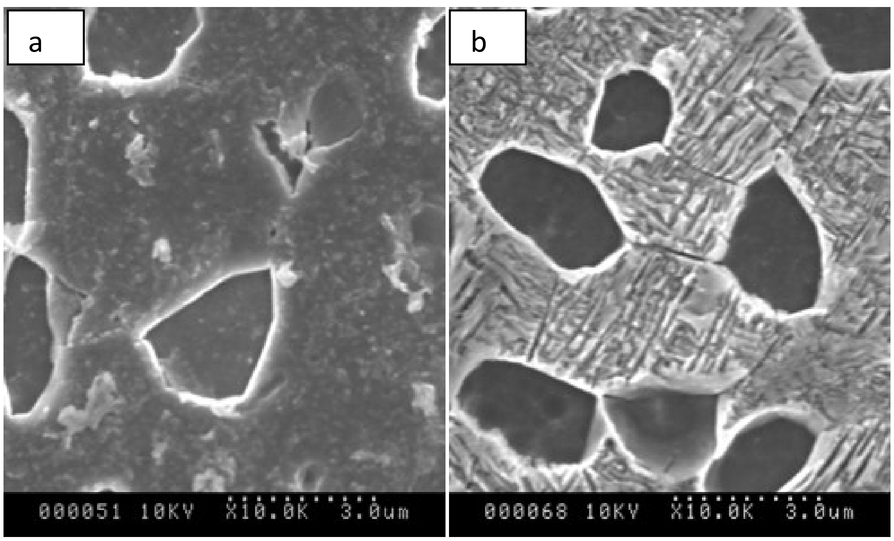

Figure 2-22: SEM images of (a) solutionized and (b) solutionized and aged one hour Ti-5553 [42].

Table 2-4: Physical and tensile properties of Ti-5553 in the STA condition [58].

Average β transus, °C	856
Density, kg/m^3	4650
Tensile elastic modulus, GPa	112
Compressive elastic modulus, GPa	113
Ultimate tensile strength (UTS), MPa	1236
Yield strength (YS) @ 0.2%, MPa	1174
Percent elongation at fracture (%. El.), with gauge length of 4D	13

Chapter 3

3 Experimental Procedure

3.1 Materials

One α + β and one β titanium alloy were examined in this study. Ti-6Al-4V, an α + β alloy, is the most commonly used alloy in the aerospace industry and was the primary focus. Initial microstructures shown in Figure 3-1 indicate that the material consists of a mixture of lamellar α and equiaxed α, with β appearing as a darker phase mainly at grain boundaries. Bands of the two grain shapes appear horizontally in the cross-sections taken perpendicular to both the rolling and transverse directions, as seen on the front and side faces of the representation in Figure 3-1.

Ti-5553, a β titanium alloy recently developed and proposed for use in landing gears, was also examined. A micrograph showing the very large β grain size can be seen in Figure 3-2a, while a close-up of the acicular substructure is presented in Figure 3-2b. Nominal compositions of both alloys are shown in Table 3-1.

The Ti-6Al-4V was received in mill-annealed (hot rolled) form and the Ti-5553 material in ingot form. These were sectioned to obtain weld coupons 13 mm in width (W), 26 mm in length (L), and 35 mm in height (H), as illustrated in Figure 3-3. An additional series of samples was sectioned with dimensions 11.1 mm (W), 12.73 mm (L), and 13 mm (H), in order to extend the load limits of the welding equipment by reducing the welding cross-section. The baseline welding parameter values for both alloys were established from optima reported for Ti-6Al-4V [6], since there is little in the literature regarding the friction welding of β or near-β Ti alloys and no specific parameters have been published [50]. Prior to welding, the contact surfaces of the samples were ground and cleaned with alcohol.

Table 3-1: Nominal compositions of starting materials (wt%)

	C	Fe	N	O	H	Al	V	Mo	Cr	Ti
Ti-6Al-4V	<0.06	0.19	<0.04	0.15	<0.01	6.0	4.0			Balance
Ti-5553	<0.06		<0.04	0.15	<0.01	5	5	5	3	Balance

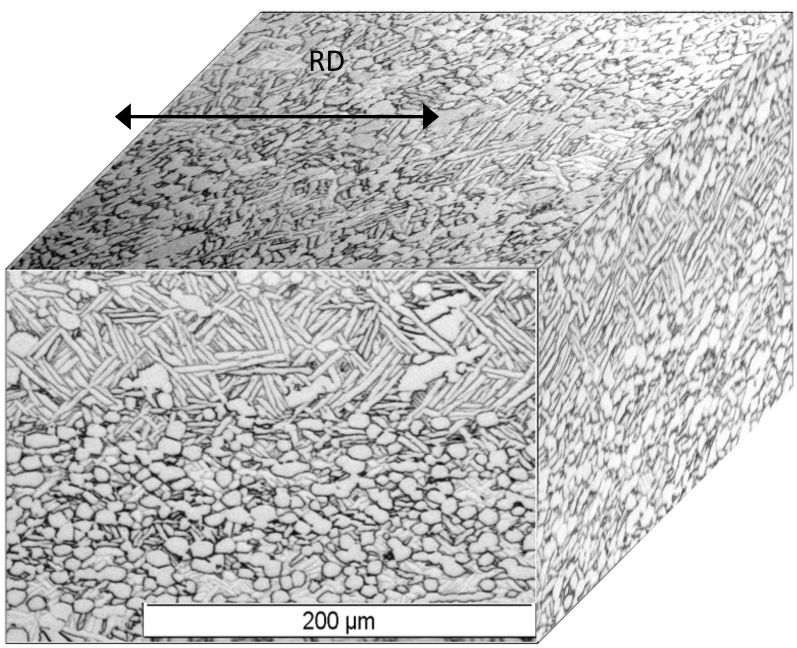

Figure 3-1: Ti-6Al-4V as-received microstructures.

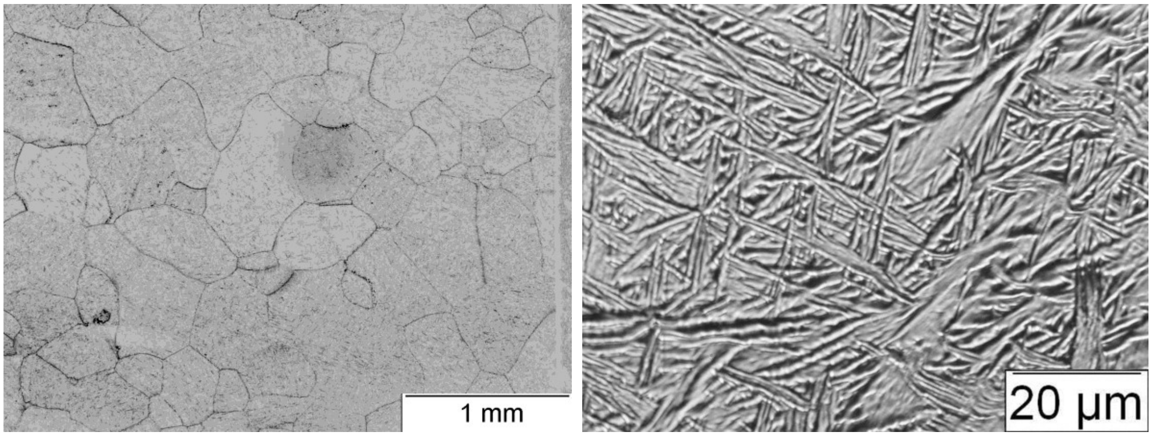

(a) (b)

Figure 3-2: (a) As-received microstructure of Ti-5553 (ingot structure); (b) as-received microstructure of Ti-5553, detailed view.

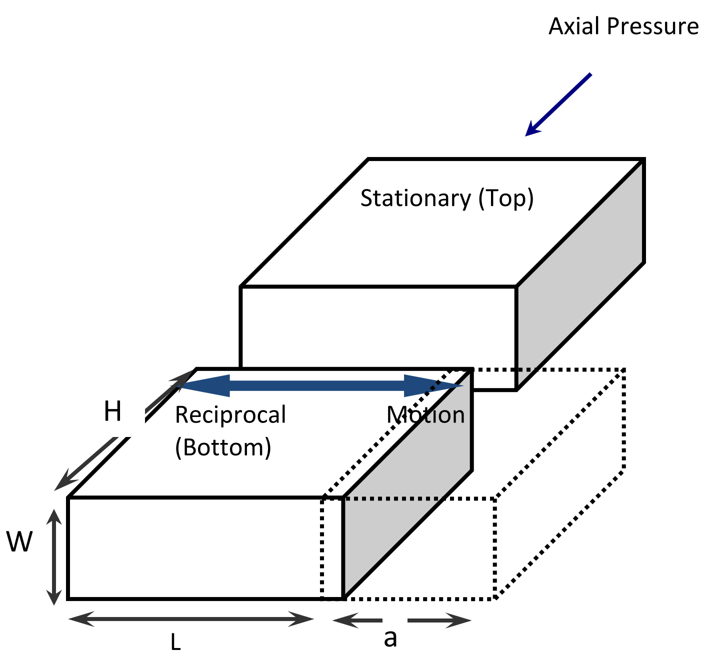

Figure 3-3: Sample geometry and oscillation direction [59].

3.2 Welding

3.2.1 LFW Equipment

The MTS linear friction welder (Figure 3-4) used in this work is hydraulically powered and is designed for weld process development. The LFW machine consists of two actuators, which provide i) the reciprocating motion and ii) the upsetting force, and tooling, which allows the positioning and clamping of the specimens during welding.

The first hydraulic actuator is the in-plane device that oscillates the lower workpiece horizontally; the second is the forge actuator that applies a downward load through the top stationary workpiece. The tooling allows specimens of up to 13 mm x 26 mm in cross-section to be held in clamping blocks one on top of the other and for them to be loaded manually into the welder.

During the welding process, the MTS software records a variety of values such as actuator position command and feedback, velocity, acceleration and load command and feedback at a rate of 1024 readings per second. The system specifications [60] are shown in Table 3-2.

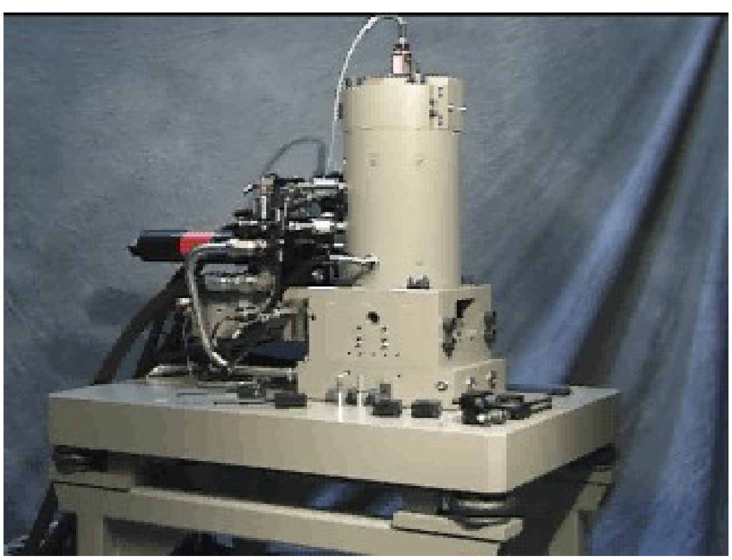

Figure 3-4. MTS linear friction welder [60].

Table 3-3 shows the experimental plan used for Ti-6Al-4V, while Table 3-4 shows the plan for Ti-5553. Initial values of the welding parameters were based on literature values [6]. These initial values are referred to hereafter as the baseline parameters, and are indicated in Table 3-3 and in Table 3-4 in bold. The parameter range was chosen with the goal of employing as high a heat input rate as possible in order to shorten the welding time and thus reduce the effect of welding on the welded structure. The maximum values of the welding parameters were determined by the limitations of the equipment.

The Ti-6Al-4V odd-numbered samples designated “welded parallel to RD” were cut so that the oscillation of the moving piece was parallel to the rolling direction; it was perpendicular on even-numbered specimens, designated “welded perpendicular to RD”.

Table 3-2: MTS linear friction welder system specifications

	Specification	Maximum
Forge Actuator:		
Forge Load	60KN (13,500lbs)	90KN (20,250lbs)
Displacement	± 6mm (1/4in.)	± 6mm (1/4in.)
In-Plane Actuator:		
Friction Force	50KN (11,250lbs)	50KN (11,2550lbs)
Displacement	± 10mm (3/8in.)	± 10mm (3/8in.)
Amplitude Range	±0.2mm (1/128in.) to ± 5mm (3/16in.)	± 5mm (3/16in.)
Frequency Range	15Hz to 100Hz	125Hz
Weld Duration Time	Up to 10sec	10sec

Table 3-3: Ti-6Al-4V all samples prepared

Sample ID	Orientation relative to RD	Amp. (mm)	Freq. (Hz)	Pressure (MPa)	Upset Dist. (mm)	Normalized Specific Power Input (kW/mm^2)	Est. Max Strain rate s^{-1}
#1	**Parallel**	**2**	**50**	**50**	**1.75**	**1**	**2.3**
#2	**Perpendicular**	**2**	**50**	**50**	**1.75**	**1**	**3.8**
#3	Parallel	2	30	90	1.75	1.08	3.8
#4	Perpendicular	2	30	90	1.75	1.08	2.3
#5	Parallel	2	50	50	1.75	1	2.3
#6	Perpendicular	2	50	50	1.75	1	2.3
#7	Parallel	2	50	90	1.75	1.8	3.8
#9	Parallel	2	50	90	1.75	1.8	7.9
#11	Perpendicular	2	50	110	1.75	2.2	7.9
#15	Parallel	2	70	90	1.75	2.52	11.0
#12	Perpendicular	2	50	70	1.75	1.4	7.9
#17	Parallel	2	70	110	1.75	3.08	11.0
#18	Perpendicular	2	50	90	1.75	1.8	7.8
#19	Parallel	2	50	50	1.75	1	7.8
#20	Perpendicular	2	50	90	1.75	1.8	7.9
#22	Perpendicular	2	50	90	1.75	1.8	7.8
#21	Parallel	2	70	70	1.75	1.96	11.0
#24	Perpendicular	2	50	150	1.75	3	7.9
#26	Perpendicular	2	110	90	1.75	3.96	17.3
#25	Parallel	2	110	90	1.75	3.96	17.3
#28	Perpendicular	2	50	150	1.75	3	7.9
#30	Perpendicular	2	110	90	1.75	3.96	17.3
#32	Perpendicular	1.5	50	90	1.75	1.35	5.9
#34	Perpendicular	3	50	90	1.75	2.7	11.8
#36	Perpendicular	1.5	50	50	1.75	0.75	5.9
#38	Perpendicular	3	50	50	1.75	1.5	11.8
#40	Perpendicular	2	110	150	1.75	6.6	17.3
#42	Perpendicular	2	90	150	1.75	5.4	14.2

Table 3-4: Ti-5553 all samples prepared

Sample ID	Amplitude (mm)	Freq. (Hz)	Pressure (MPa)	Upset (mm)	Specific Power Input (normalized)	Estimated max strain rate s^{-1}
#1	**2**	**50**	**50**	**1.75**	**1.0**	**3.6**
#2	**2**	**50**	**50**	**1.75**	**1.0**	**3.6**
#3	**2**	**50**	**50**	**1.75**	**1.0**	**3.6**
#4	2	30	90	1.75	1.1	2.2
#5	2	30	90	1.75	1.1	2.2
#6	2	30	70	1.75	0.8	2.2
#7	2	30	70	1.75	0.8	2.2
#8	2	50	70	1.75	1.4	3.6
#9	2	110	50	1.75	2.2	17.3
#10	2	110	50	1.75	2.2	17.3
#11	2	150	50	1.75	3.0	23.5
#12	2	150	50	1.75	3.0	23.5
#13	2	50	50	1.75	1.0	7.9
#14	2	50	50	1.75	1.0	7.9
#15	2	50	50	1.75	1.0	7.9
#16	2	50	50	1.75	1.0	7.9

3.3 Thermal Analysis

Several techniques were used to attempt to accurately measure the temperature of the material during welding. In Vairis and Frost's work [30], thermocouples were spot welded to the outside face of the stationary block at a specific distance from the interface. Axial shortening was measured to compensate for the changing distance of the thermocouple from the interface and then interface temperatures were calculated from the measured temperatures and distances using FEM. In addition to being somewhat inaccurate and dependent on the reliability of the FEM model, this technique proved too fragile to maintain contact (and hence data acquisition) during welding.

Using the technique developed at NRC-IAR-AMTC by Maxime Harvey and Maxim Guérin, holes were drilled in the stationary specimen vertically from the bottom (cool) end of the block. A channel was created as shown in Figure 3-5a to prevent the thermocouple from being crushed or causing a short circuit via contact with the material. In order to maintain the thermocouple tip pressed against the top of the hole, a spring (Figure 3-5b) was attached to the thermocouple, lightly compressed, and then glued to the specimen to maintain the pressure. Despite these precautions, upon sectioning after welding, it was found that (as shown in Figure 3-5c) the thermocouple had been pushed down the hole by the pressure of the plasticized material being compressed by the axial force during welding.

To solve the problem, holes were next drilled laterally such that the thermocouple tip could not be pressed downwards through an existing hole. Upon sectioning, it was determined that the thermocouple tip still did not enter the plasticized material of the interface but was consistently moved outside the interface zone. Thus thermal analysis results cannot help but underestimate the actual temperature experienced by the material in the weld interface.

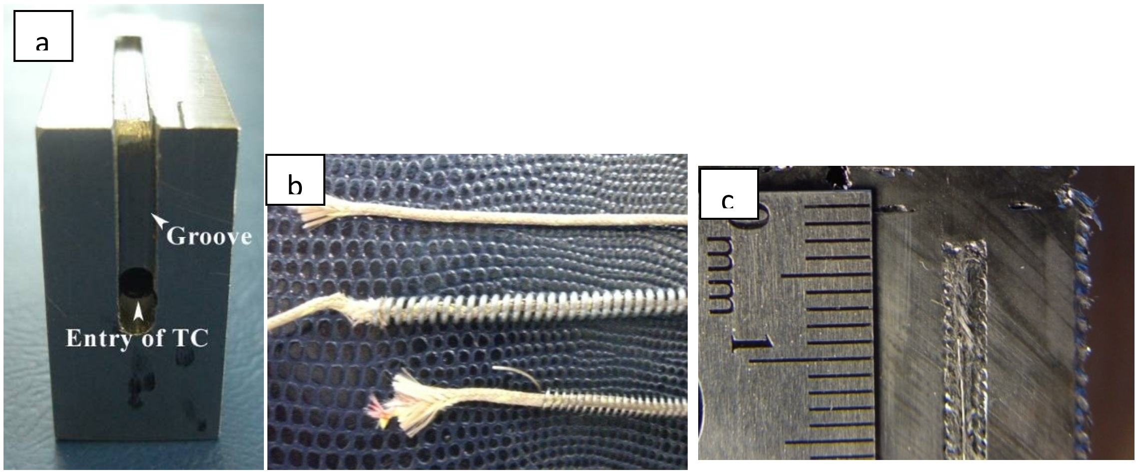

Figure 3-5: Thermal analysis technique: a) channel machined in sample block; b) thermocouple wire bare and inserted into two spring sizes; c) plasticized material pushed down into thermocouple hole during welding, displacing thermocouple from desired location.

3.4 Metallography, SEM and EBSD

LFWed samples were sectioned both parallel and transverse to the oscillation direction through the weld zone for metallographic and EBSD investigation. Polishing procedures (detailed in Table 3-5) were developed to prepare samples for optical microscopy and for the preliminary preparation of the EBSD samples. Between each grinding/polishing step, samples were fully rinsed and dried and between grinding and polishing, ultrasonic cleaning was performed. Final EBSD polishing was carried out in a Buehler Vibro-Met vibratory polisher for 12 hours using colloidal silica. These materials required an extensive and sensitive polishing procedure, as electropolishing is not recommended if the β phase is to be preserved [5]. For examination of the microstructure using optical microscopy, etching was done using Kroll's reagent. Microstructural examination was then performed using an inverted optical microscope (Olympus GX71) equipped with digital image analysis software (AnalySIS Five). Back-scatter imaging and EBSD mapping were performed at 20 kV on a Hitachi S-3000N VP-SEM equipped with an Oxford (HKL) EBSD data acquisition system (polished surface). Additional EBSD data were acquired using a Philips FEG-SEM equipped with the EDAX TSL OIM EBSD detector and software.

Table 3-5: Grinding and polishing procedure for Ti alloys

Step	Surface	Abrasive	Speed (rpm)	Load (N/samp)	Lubricant	Time (min)	Direction (rel. to cloth)
1	SiC paper	320 grit	200	20	water	1 (until planar)	same
2	SiC paper	500 grit	200	20	water	2	same
3*	SiC paper	800 grit	200	20	water	3	same
4	Composite napping disk	9 µm diamond suspension	150	25	alcohol-based	4	same
5*	Porous rubber	0.4 µm colloidal silica	150	30	water for last 30 seconds	5	opposite

*Step may be repeated if surface is not ready.

Low magnification overview scans across the entire weld area were performed at a step size of 1 µm, while higher magnification scans were performed at a step size of 0.2 µm using beam scan and not stage scan mode. It was found that pattern quality was very susceptible to small changes in microscope settings; thus the settings shown in Table 3-6 were chosen for optimal results and not varied. Reference patterns used for Ti α and β crystals were those included with the HKL Channel5 or TSL OIM Data Collection IV software, respectively.

Table 3-6: EBSD settings

Voltage	20 kV
Working Distance	15 mm
Tilt	70°
Aperture	3 (100 μm)
Spot size	5 (arbitrary units)
Exposure	0.4 s
Gain	-3.2
Hough peaks	Min 3, Max 7

3.5 Heat Treatment

Selected Ti-5553 samples were heat treated both before and after welding in order to examine the effects of these treatments on the material properties. The heat treatment cycles employed are presented in Table 3-7. Heat treatment was performed at Standard Aero, Winnipeg, Canada.

Table 3-7: Heat treatment cycles for Ti-5553

Solution HT Cycle (ST)	**Ageing Cycle (A)**
816°C for 45 min. in vacuum, argon quench	621°C for 8 hr in argon PP, argon quench

3.6 Mechanical Testing

Microhardness was measured using a Struers Duramin A300 machine with a fully automated testing cycle (stage, load, focus, measure). A load of 300 g was applied using a load cell with closed-loop circuit control and hardness profiles were determined across the weld region using an average of three measurements for each point, with an indent interval of 0.2 mm and a dwell period of 15 seconds.

Nanohardness was measured on selected samples using a nanoindentation transducer, a Hysitron Triboscope, mounted above the sample. The diamond indenter, a three-sided pyramid (Berkovich), was used for indentation testing. The nanoindentation system was calibrated by indentation testing performed on a fused quartz standard. The area function of the indenter (projected area as a function of depth) and the system compliance were determined and periodically checked throughout testing. The specific load-versus-time profiles used for each material have consisted of loading and unloading rates between 0.25 mN/s and 2.0 mN/s and maximum loads between 0.7 mN and 9.5 mN. Analysis of load-displacement data was carried out using the Oliver and Pharr method [61]. At the maximum load P_{max}, the hardness, H_{NI}, is obtained from:

$$H_{NI} = P_{max}/A(h_c) \qquad \text{(Eq. 3.1)}$$

where $A(h_c)$ is the contact area. It is important to note that the area of contact determined from nanoindentation testing is a projected area, different from the full-contact area used in a standard Vickers hardness test. [62]

In order to verify that the indentation size effect would not affect the results, a series of indentations at a range of loads from 500 µN to 20 N was performed. The dependence of measured hardness on load flattened out at approximately 5 mN, the load selected for the cross-weld profile series.

For selected weld conditions, three tensile specimens having a standard sub-size geometry of 25 mm in gauge length, 6 mm in width and 4 mm in thickness were machined in accordance with ASTM E8M-01 (see Figure 3-6). All specimens were tested at room temperature using a 250 kN MTS 810 tensile machine equipped with an Aramis

3D deformation measurement system. Before executing tensile testing, each sample was painted with a high-contrast random pattern of black on a white background. The functionality of the Aramis system depends on the quality of this speckle pattern. The quality of the pattern was verified before mechanical property evaluation to ensure strain recording along the entire gauge length. After examination for pattern recognition, tensile property evaluation was conducted using displacement control at a rate of 2 mm/min up to the yield point and then 8 mm/min up to rupture with the Aramis acquisition rate set at 2 frames per second (fps).

E 8/E 8M – 08

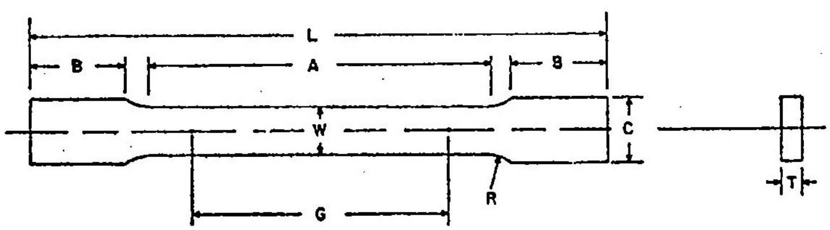

	Dimensions
	Subsize Specimen
	mm [in.]
G—Gage length	25.0 ± 0.1[1.000 ± 0.003]
W—Width	6.0 ± 0.1 [0.250 ± 0.005]
T—Thickness	4 [0.16]
R—Radius of fillet, min	6 [0.250]
L—Overall length	70 [2.75]
A—Length of reduced section, min	32 [1.25]
B—Length of grip section	max. available
C—Width of grip section, approximate	10 [0.375]

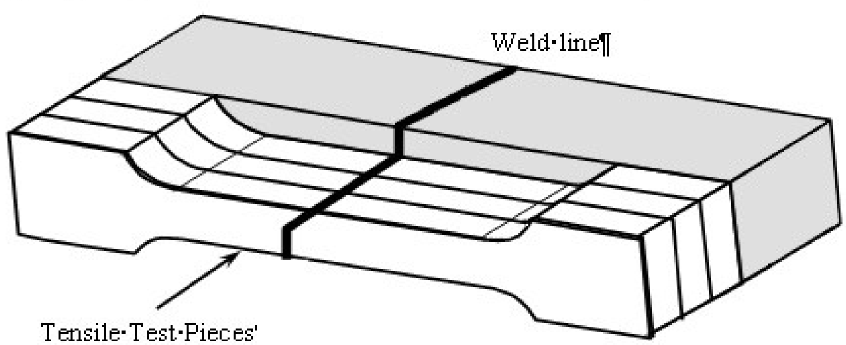

Figure 3-6: ASTM E8 subsize tensile specification and cutting diagram from welded coupon.

Chapter 4

4 Ti-6Al-4V Results

The appearance of a representative welded Ti-6Al-4V sample is presented in Figure 4-1. While all welded samples resembled this one in that flash was extruded on all four sides, the magnitude and appearance of the flash did vary depending on the welding parameters.

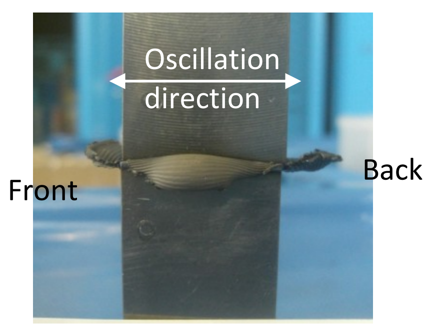

Figure 4-1: LFW Ti-6Al-4V joint showing flash extending towards back and front.

Welding perpendicular or parallel to the rolling direction did not seem to influence the macroscopic appearance of the welded sample, nor did the magnitude of the axial pressure, apart from the aforementioned flash characteristics. No deformation of the bulk material close to the interface was visible to the naked eye.

In Table 4-1 the measured and calculated data associated with the experiments are presented. Axial pressure, frequency, and amplitude are inputs to the welding process; P·a·f is simply a combination of these three main weld parameters; weld time and weld thickness are measured respectively during or after welding; and maximum strain rate and maximum strain are calculated from these values based on the equation elaborated in section 7.1.

Table 4-1: Data associated with the welding of Ti-6Al-4V

Weld ID	Axial Pressure P (MPa)	Freq. f (Hz)	Ampl. a (mm)	P·a·f (kN/m*s)	Measured Weld time t (s)	Estimated Max Strain rate $\dot{\varepsilon}$ (s^{-1})	Calculated Max Strain ε	Measured Weld Thickness d (mm)
1	50	50	2	5000	1.2	3.9	4.7	0.76
3	90	30	2	5400	1.5	2.3	3.4	0.43
9	90	50	2	9000	0.66	3.9	2.5	0.22
11	110	50	2	11000	0.59	7.8	4.6	0.24
15	90	70	2	12600	0.53	11	5.8	0.27
21	110	70	2	15400	0.52	11	5.7	
24, 28	150	50	2	15000	0.57	7.8	4.4	0.29
26, 30	90	110	2	19800	0.38	17.3	6.6	0.24
40	150	110	2	33000	0.36	17.3	6.2	0.13
42	150	90	2	27000	0.35	14.1	4.9	0.3
44	50	110	2	11000	0.44	17.3	7.6	0.34
46	150	30	2	9000	0.97	4.7	4.6	0.23
32	90	50	1.5	6750	0.92	5.9	5.4	0.16
36	50	50	1.5	3750	1.24	5.9	7.3	0.36
34	90	50	3	13500	0.5	11.8	5.9	0.22
38	50	50	3	7500	0.63	11.8	7.4	0.33

4.1 Thermal Analysis.

Several techniques were used in an effort to collect reliable data on the temperature evolution of the material close to the interface during welding. Although no perfect solution was found, some data were collected and are presented here. Problems included thermocouples breaking during welding, thermocouples being pushed out of the weld interface zone by plasticized material, and thermocouples short-circuiting due to contact with the material being welded at indeterminate locations not necessarily in the interface region.

Thermal analysis results for the Ti-6Al-4V are summarized in Table 4-2. Due to the small amount of data acquired, few conclusions can be drawn. Repeatability has not been established, as no two successful thermal measurements were made during welding using identical parameters. It is entirely possible that all peak measurements taken at 1 mm from the interface are approximately equivalent, given the level of uncertainty.

Table 4-2: Thermal analysis results for Ti-6Al-4V welding.

Sample ID	Pressure (MPa)	Frequency (Hz)	TA Result	Peak temp. recorded (°C)	Temp. 10 mm from interface (°C)
#5	50	50	Failed		
#6	90	30	Success	862	214
#7	90	50	Noisy		
#9	90	50	Too low		
#17	110	70	Broke		
#18	90	50	Success	1088	
#19	50	50	Success	802	
#20	90	50	Failed		
#21	110	70	Success	943	
#22	90	50	Failed		

What can be said is that the two curves successfully obtained at different locations during the same weld, shown in Figure 4-2, do represent the delta between the temperature evolution 10 mm from the interface and adjacent to it and as such could be used as inputs for a temperature model. Figure 4-3 represents one of the thermal analysis trials that involved the breaking and spontaneous re-welding of the thermocouple. The data subsequent to the break appear reasonable but again cannot be considered completely reliable as it is uncertain where the re-weld was located and whether it was also welded to the material being welded.

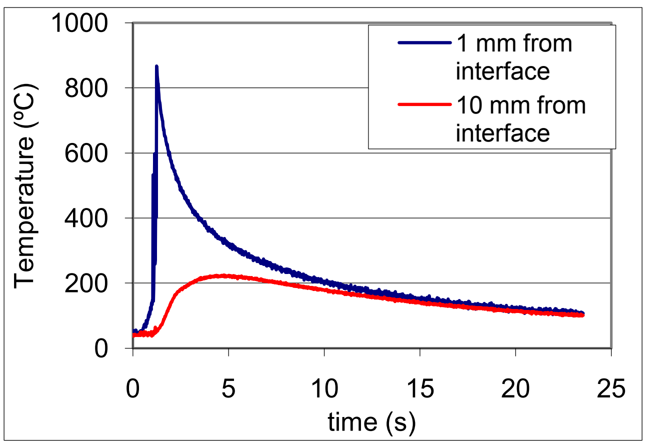

Figure 4-2: Thermal analysis curves for sample Ti-64#6.

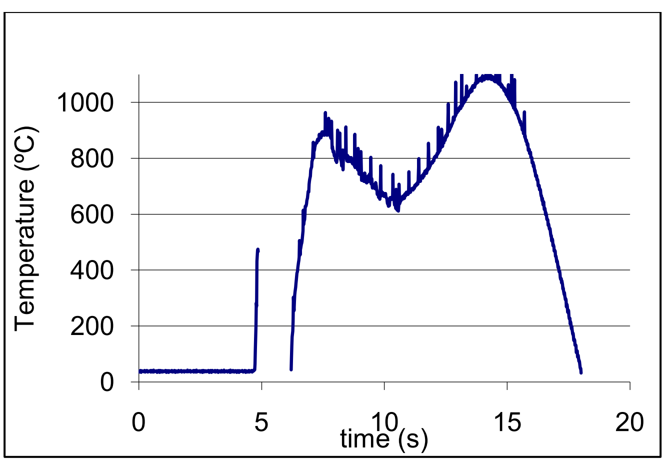

Figure 4-3: Thermal analysis curve for sample Ti-64#18.

4.2 Flash Morphology

It has been demonstrated [6, 32] that the traces of the oscillations undergone by the material during the welding process can be seen in the ridges observed in the flash extruded during welding. In the cross-sectional images of weld flash shown in Figure 4-4 to Figure 4-13, not only can the extrusion cycles be seen in the ridges of the flash but in most images the alternating top and bottom extrusions can be seen as well. With increasing axial pressure, frequency, and/or amplitude, as expanded upon in section 2.2.3, increased specific power input (SPI) results in a more rapid welding process. For a given frequency, a shorter welding time should result in fewer actual oscillations. This is borne out in general by the actual flash images. The differences are most dramatic when comparing the appearance of the three sets of welds done at low amplitude (1.5 mm - samples 32 and 36), medium amplitude (2 mm - samples 28, 30, 40, 42, 44, and 46), and high amplitude (3 mm - 34 and 38).

Figure 4-4: Ti-64#32 (low amplitude series)

Figure 4-5: Ti-64#36 (low amplitude series)

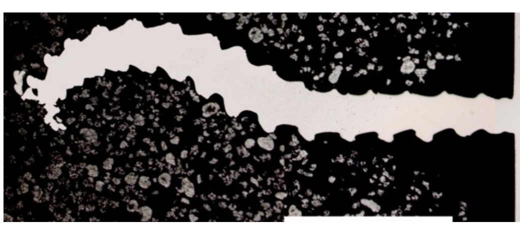

Figure 4-6: Ti-64#28 (medium amplitude series)

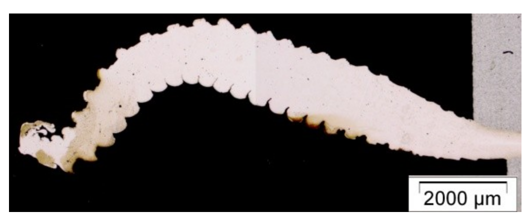

Figure 4-7: Ti-64#30 (medium amplitude series)

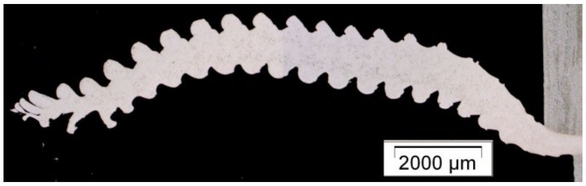

Figure 4-8: Ti-64#40 (medium amplitude series)

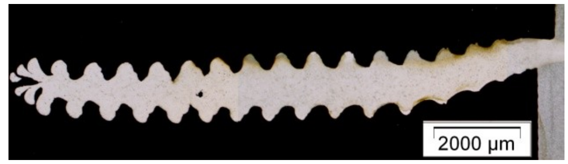

Figure 4-9: Ti-64#42 (medium amplitude series)

Figure 4-10: Ti-64#44 (medium amplitude series)

Figure 4-11: Ti-64#46 (medium amplitude series)

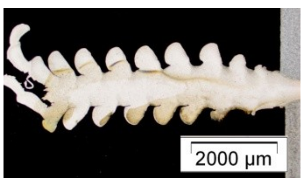

Figure 4-12: Ti-64#34 (high amplitude series)

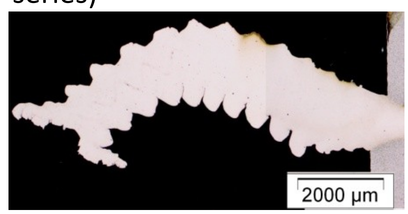

Figure 4-13: Ti-64#38 (high amplitude series)

4.3 Microstructures

Optical micrographs of the as-received parent material are shown in Figure 4-14. The Ti-6Al-4V material is composed of approximately 93-95% α phase and 5-7% β phase and appears banded in both the RD-ND and the TD-ND planes as can be seen in the lower magnification micrograph (Figure 4-14a). The darker bands consist of equiaxed α grains interspersed with equiaxed colonies of α-β lamellae. The equiaxed grains averaged 10 µm in diameter. The lighter bands consist of 5-10 µm acicular α grains surrounded by grain boundary β. The different grain morphologies can be observed in the higher magnification micrograph (Figure 4-14b). Looking at the material in three dimensions (see Figure 3-1), it is clear that not only the RD but also the TD displays these bands, when looking at a cross-section of the material taken perpendicular to the original rolled surface (i.e. parallel to the ND). The rolled surface itself appears more 'pancaked', leading to the understanding that the grains have been compressed vertically and spread in all directions horizontally during rolling. Thus there is little to distinguish the RD from the TD direction visually when looking at a cross-section taken in any plane containing the ND.

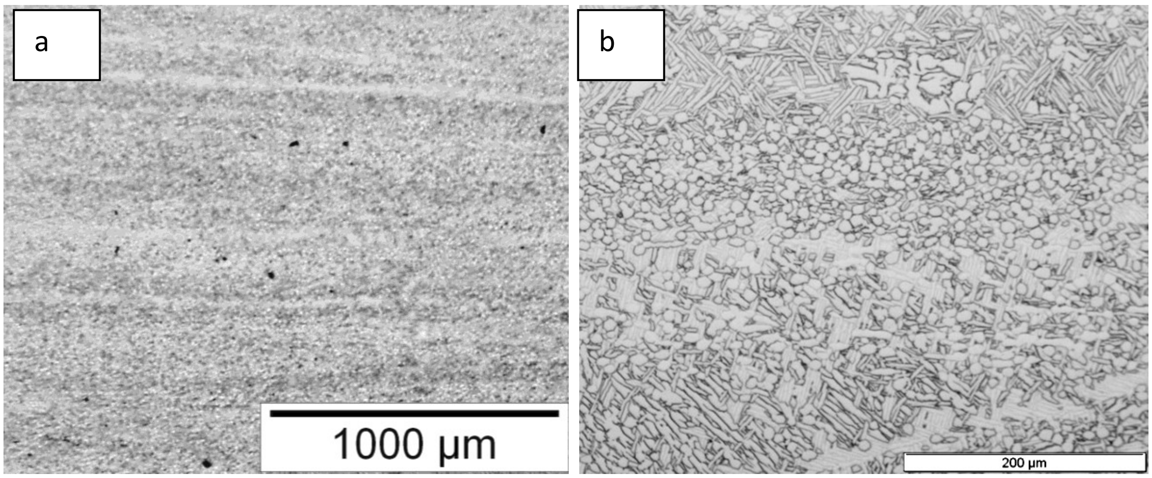

Figure 4-14 : Optical micrographs in the RD-ND plane of as-received Ti-6Al-4V: a) low magnification showing banded structure; b) higher magnification showing individual equiaxed and acicular α grains.

The microstructure of a sample welded with the oscillation direction *parallel* to the rolling direction is illustrated in Figure 4-15. At high optical magnification (see (a)), the grains are not easily seen along the weld centre using optical microscopy, although faint indications of a martensitic structure can be seen. The small dark areas may represent etch pitting (also visible in the other micrographs). This highly deformed region does not etch as readily as the undeformed grains; furthermore, the literature [5, 6] suggests that these grains are very fine, contributing to the poor etching response. In Figure 4-15(b), an SEM back-scattered electron micrograph of the weldline is presented, in which the martensitic structure can be seen more clearly; here the needles are approximately 5 to 7 µm in length and under 500 nm in width. It is difficult to identify the traces of the original β grain boundaries in such a structure. In micrograph (c), representing the structure about 0.375 mm from the weldline, it is apparent that the grains are elongated along the direction of material flow. Finally, in Figure 4-15(d), 0.725 mm from the weld line, the undeformed bimodal α/transformed β microstructure can be seen clearly.

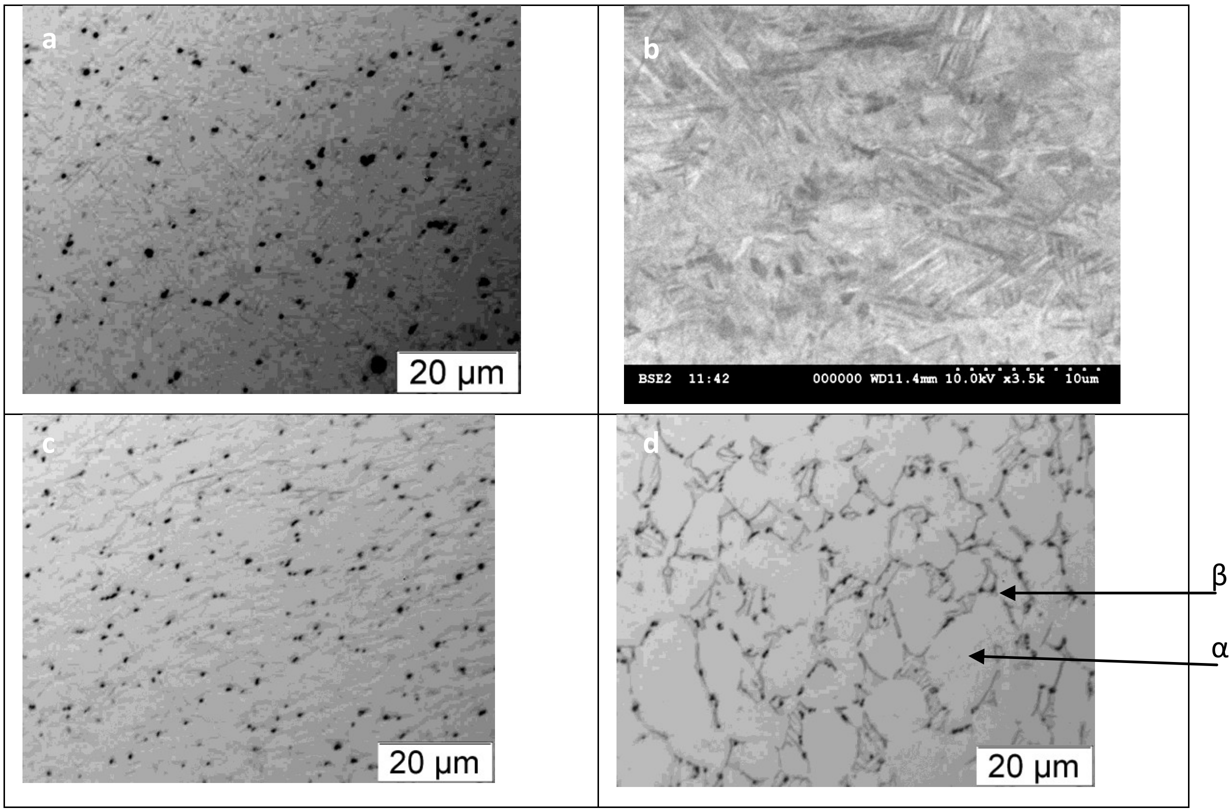

Figure 4-15 : Ti-64#1, welded parallel to the rolling direction; etched with Kroll's reagent. (a) weld centre at high magnification (b) BSE image of weld centre at 3.5 times the magnification in (a); (c) 0.375 mm from weldline; (d) 0.725 mm from weldline.

Optical micrographs of the sample welded with the oscillation direction *perpendicular* to the rolling direction are presented in Figure 4-16. Here the same welding parameters were employed as in the previous example. The weld region appears bright due to its resistance to etching, which is attributed to this region being heavily deformed and very fine grained. This phenomenon occurred in the parallel sample as well. An approximate measurement of the weld (unetched) region indicated that it was 0.75 mm across. The deformed region (TMAZ) from the weld line up into the parent metal is illustrated in Figure 4-16(b). In Figure 4-16(c), similar to Figure 4-15(a), faint grain lines in the weld centre indicate the presence of a martensitic structure. The microstructures (not presented here) for this sample at 0.325 mm and 0.725 mm from the weld, in turn, resemble those of the parallel-welded sample presented in Figure 4-15(c) and (d).

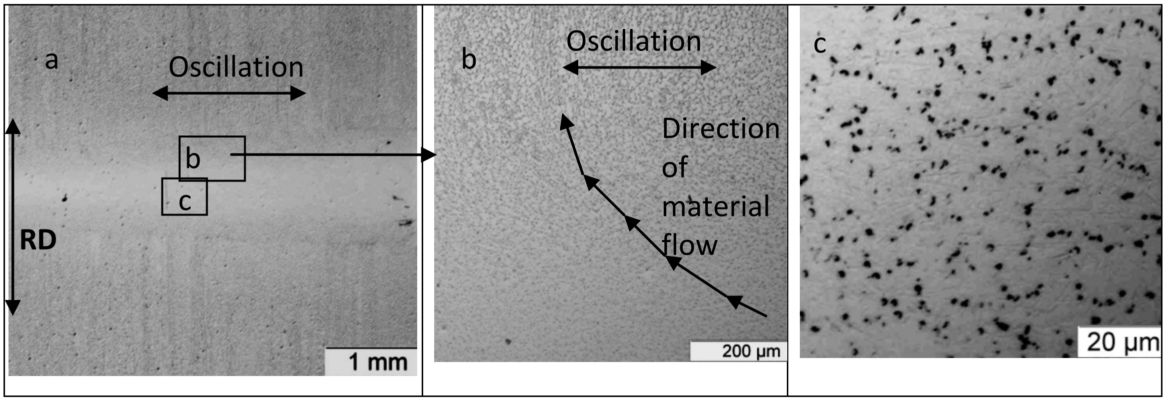

Figure 4-16: Ti-6Al-4V #2, welded perpendicular to the rolling direction; etched with Kroll's reagent. (a) Weld line (low mag) (b) Magnification of weldline area shown as box "b" on micrograph (a); (c) High magnification of weldline area shown as box "c" on micrograph (a).

From this point on, no further distinction will be made between parallel-welded and perpendicular-welded samples unless a difference in properties (such as in tensile testing) warrants it. For the most part, it was found that the two were equivalent.

The effect on the weld thickness of the parameters that were varied is illustrated in Figure 4-18 with the aid of polarized light optical micrographs of the first five samples. Additional welds were performed to improve the understanding of the relationship between weld thickness and the weld parameters. Images of these welds are presented in Figure 4-17 and Figure 4-19 to Figure 4-28.

Figure 4-17: Ti-64#28, from flash to centre, etched (Kroll's reagent)

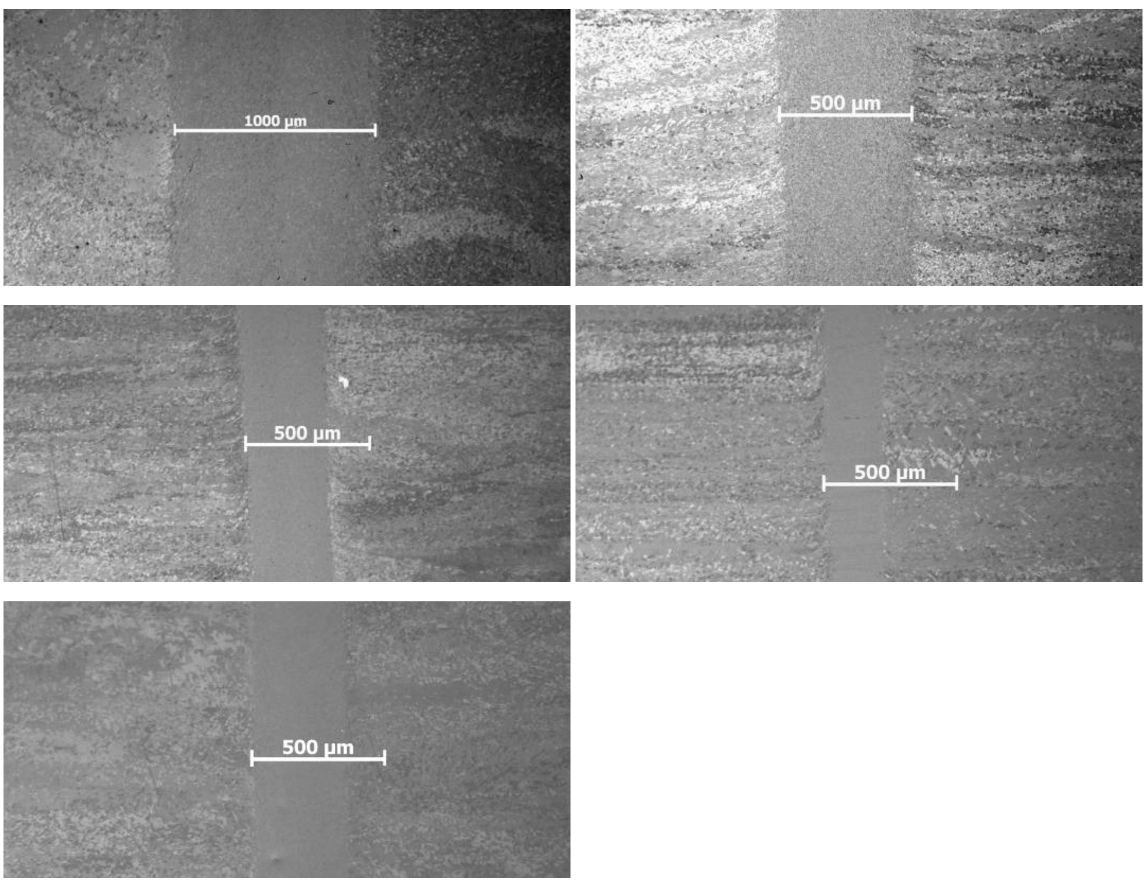

Figure 4-18: Polarized light micrographs of weld thicknesses: (a) sample #1 50 MPa, 50 Hz, 1000 µm weld; (b) sample #3 90 MPa, 30 Hz, 500 µm weld; (c) sample #9 90 MPa, 50 Hz, 345 µm weld; (d) sample #11 110 MPa, 50 Hz, 240 µm weld; (e) sample #15 90 MPa, 70 Hz, 330 µm weld

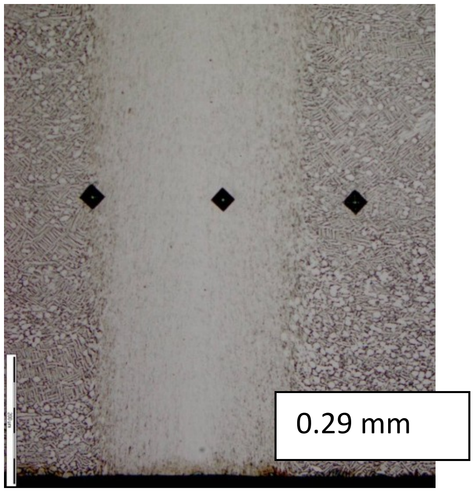

Figure 4-19: #28 etched, centre weld thickness

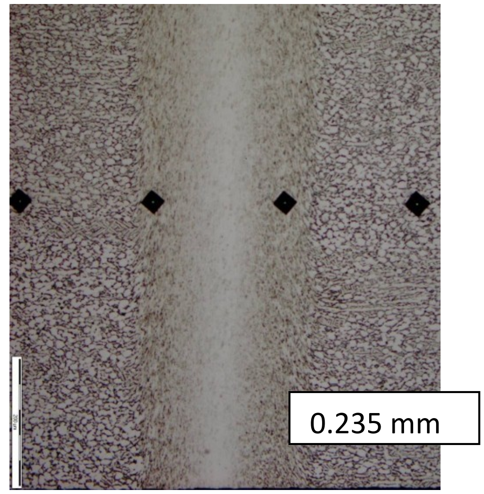

Figure 4-20: #30 weld thickness

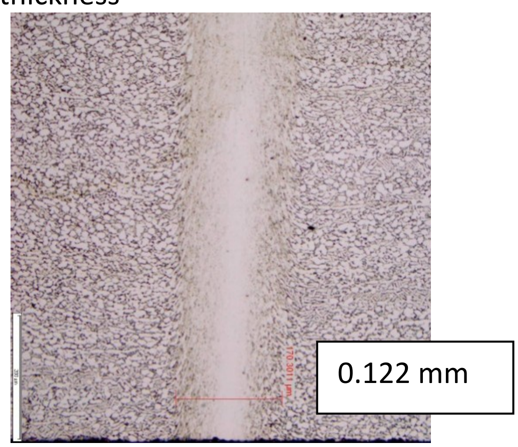

Figure 4-21: #40 weld thickness

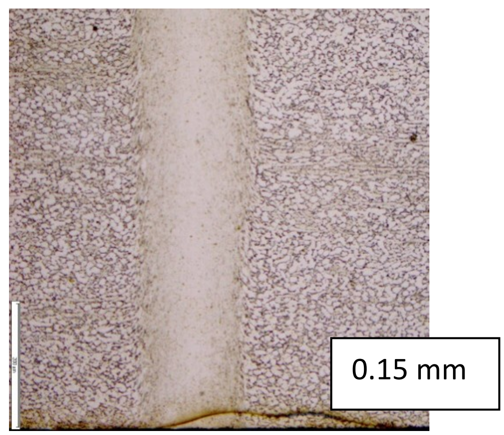

Figure 4-22: #42 weld thickness

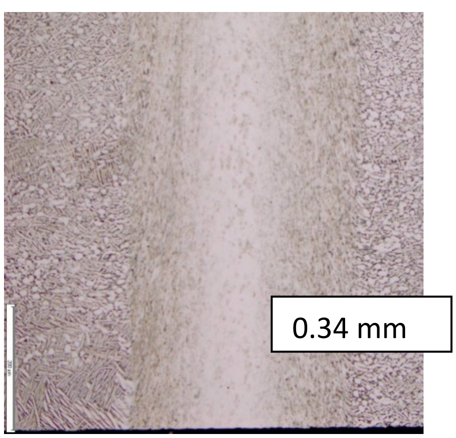

Figure 4-23: #44 weld thickness

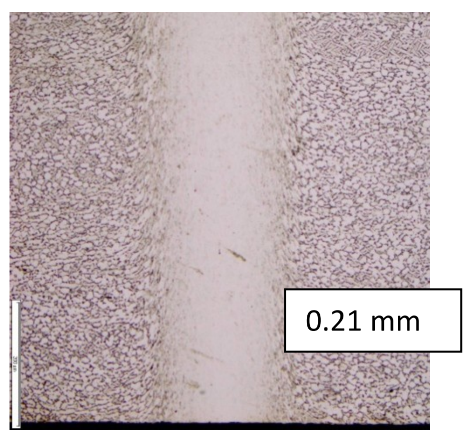

Figure 4-24: #46 weld thickness

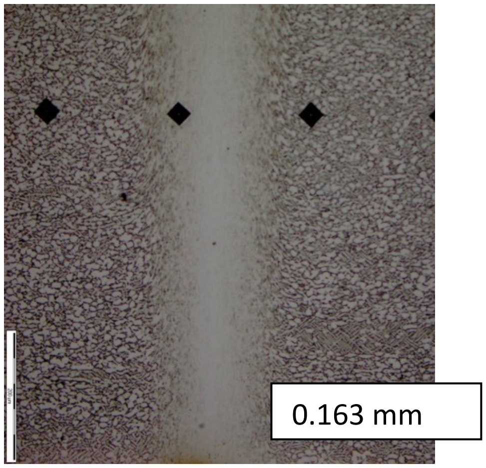

Figure 4-25: #32 weld thickness (low amplitude series)

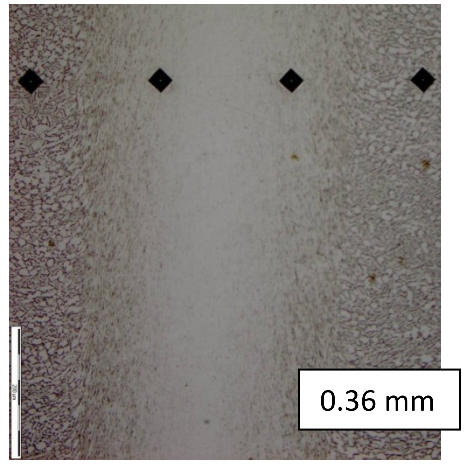

Figure 4-26: #36 weld thickness (low amplitude series)

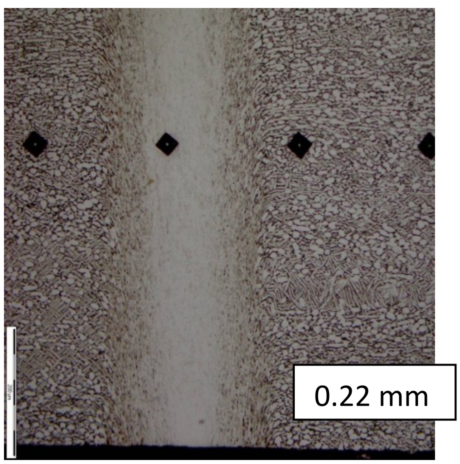

Figure 4-27: #34 weld thickness (high amplitude series)

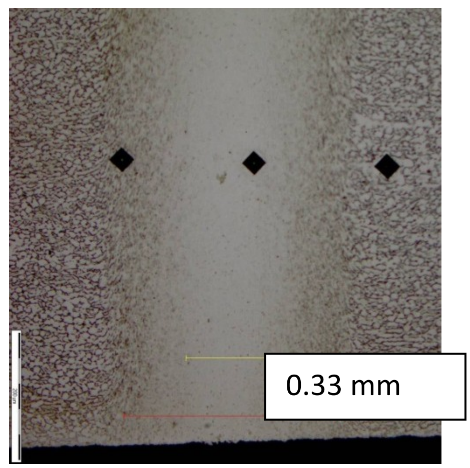

Figure 4-28: #38 weld thickness (high amplitude series)

4.4 Microhardness measurements

It can be seen from Figure 4-29 and Figure 4-30 that the weld region is somewhat harder than the surrounding TMAZ. The TMAZ hardness is comparable to that in the as-received material, which ranged from 300 to 350 HV. Comparing the samples welded from low to high pressure at constant frequency (Figure 4-29), the highest pressure (green diamonds) can be seen to produce the narrowest weld zone with a sharp, well-defined hardness drop at +/- 0.6 mm, in agreement with the microstructural evidence. The intermediate pressure sample has approximately the same peak hardness as the lowest pressure sample but again displays a narrow region, about +/- 0.6 mm, of hardening at the weld line. Finally, the lowest pressure sample presents a hardened zone approximately +/- 1.0 mm from the weld centre.

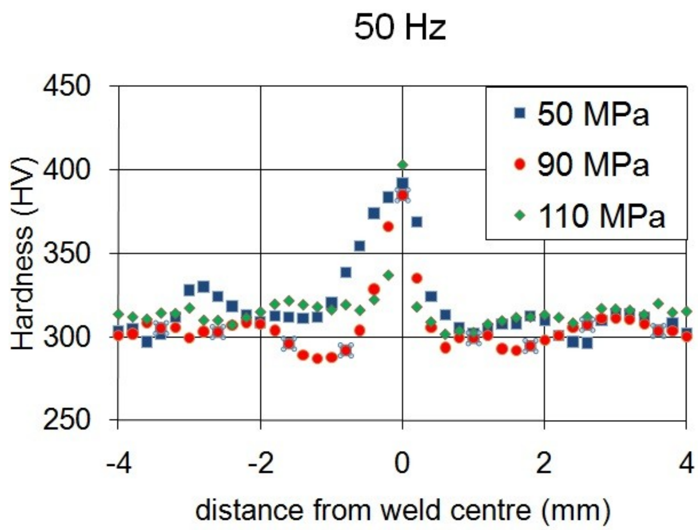

Figure 4-29: Microhardnesses across weld line for samples welded at 50 Hz.

Comparing instead the variation due to frequency, for a constant axial pressure of 90 MPa (Figure 4-30), a similar trend can be observed. In this case, however, the variation in thickness of the affected region is less pronounced.

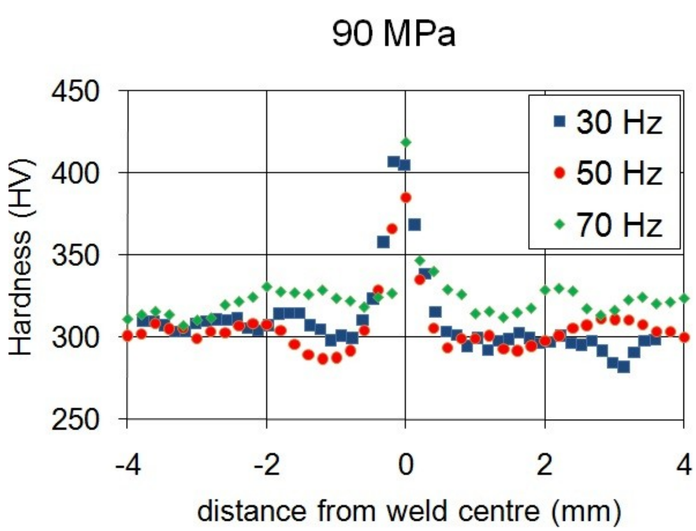

Figure 4-30: Microhardnesses across weld line for samples welded at 90 MPa.

4.5 Tensile measurements

The tensile tests performed using the MTS tensile machine revealed that the weld zone and TMAZ were stronger than the surrounding parent material. This was concluded in that all the fractures occurred outside the weld zone. Micrographs of the fractured ends of two welded specimens (Figure 4-31) are etched to show that the weld (which would appear white) is not within 2 mm of the break. In fact, fracture locations ranged from 5 to 10 mm away from the weld, in a gauge length of 25 mm with the weld in the middle.

Since this alloy may be used at temperatures up to approximately 350°C, the applicability of room temperature tensile results must be considered. In fact, the only microstructural change anticipated at this temperature would be a very slow grain growth in the recrystallized region. This probably would have no perceptible effect on the tensile properties in the time frame of an ordinary tensile test. However, effects might be observed in a long term test such as a creep or fatigue test. Creep and fatigue resistance were not explored in this work but might be of interest to future researchers.

As-received material, tested along both the RD and the TD orientations, closely matched the behaviour of the welded samples, as shown in Table 4-3 and Figure 4-32. Samples pulled along the RD, shown in shades of blue for the welded and green for the as-received, displayed lower UTS's and conventional engineering stress-strain curves exhibiting gradual strain hardening followed by an apparent softening phase presumably related to necking. Samples pulled along the TD, indicated by red for the welded and shades of brown for the as-received material, had higher UTS's and an oddly flattened initial stress-strain curve shape immediately following the elastic region.

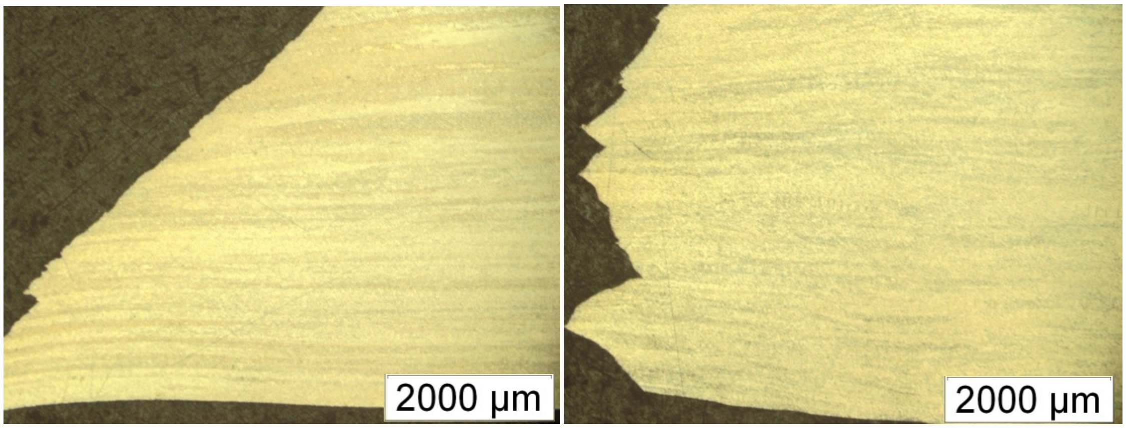

Figure 4-31: Fractured tensile samples of Ti-6Al4V: a) #5; b) #6.

Table 4-3: Tensile measurements for Ti-6Al-4V as-received and welded specimens.

Sample ID	E (GPa)	YS (MPa)	UTS (MPa)	Total elong. (%)	Colour on plot
Ti-64#RD-1	110	841	916	14.5	green
Ti-64#5-2	112	860	933	13.8	blue
Ti-64#5-3	110	864	943	15.8	lt. blue
Ti-64#TD-1	126	948	983	15.2	rust
Ti-64#TD-2	127	968	1004	15.0	brown
Ti-64#6-2	124	957	1000	13.7	red

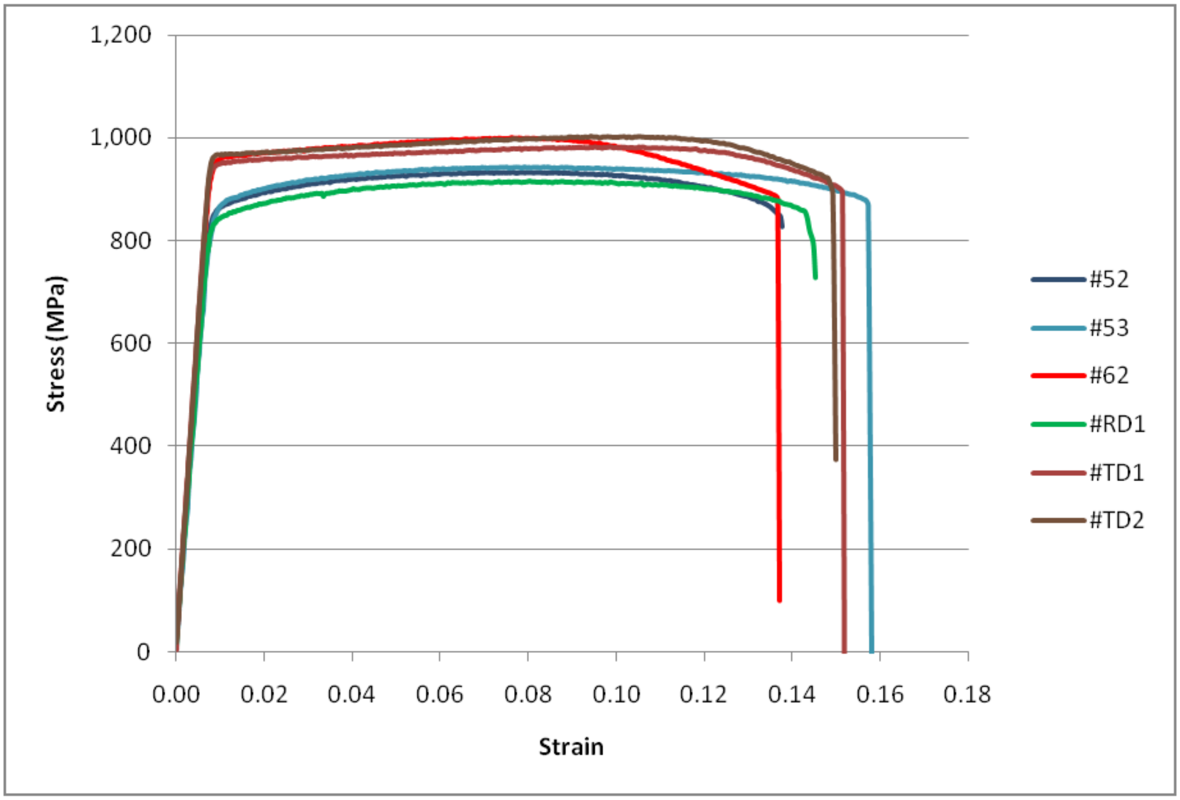

Figure 4-32: Engineering stress-strain curves for as-received (RD, TD) and welded (numbered) Ti-6Al-4V specimens.

4.6 Microtexture measurements

Orientation data were obtained from the as-received and welded samples. The material required an extensive and sensitive polishing procedure, as electropolishing is not recommended in order to preserve any β that may be found in the structure. In fact, very few β grains were detected and indexed in any case. The pole figures and inverse pole figure maps below refer solely to the orientations of the α (HCP) grains.

The as-received texture, as shown in both the pole figures (Figure 4-33) and the inverse pole figure map (Figure 4-34) has a strong basal component in the direction approximately normal to the rolling direction, as predicted in the literature and as in the typical rolled texture presented in Figure 2-15. Metals or alloys with c/a ratios less than the ideal 1.633, such as titanium, tend to form rolling textures with the basal poles tilted plus or minus 20 to 40 degrees from the normal toward the transverse direction and [10-10] poles aligned with the rolling direction [41].

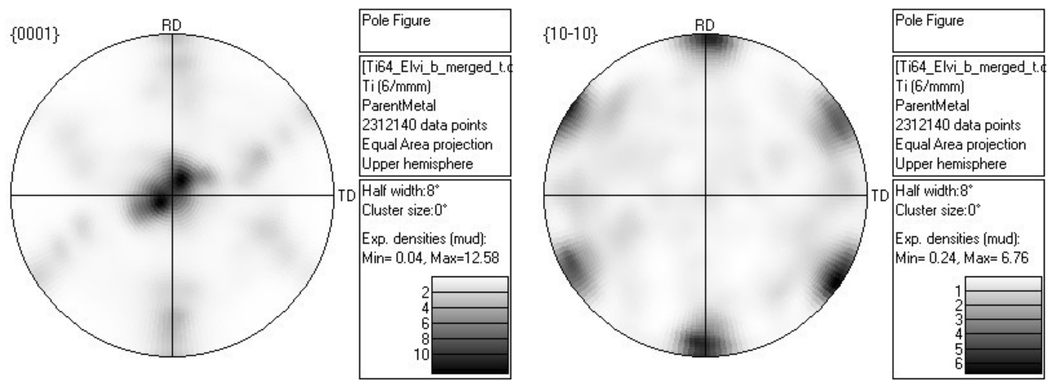

Figure 4-33: Pole figures of the as-received Ti-6Al-4V.

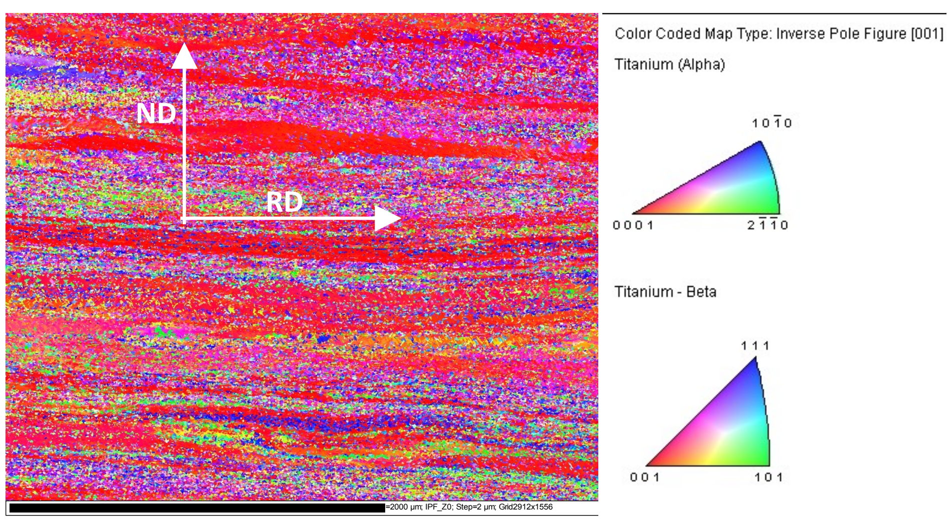

Figure 4-34: As-received Ti-6Al-4V microstructure determined by EBSD showing the banded structure. The TD is perpendicular to the plane shown in this view.

The inverse pole figure map (Figure 4-34) displays the banded microstructure already described in the microstructure section (section 4.4 in this chapter) with the addition of information about the orientations of the bands. It can be seen that several bands are almost entirely red, indicating the presence of the basal texture, while the majority of the bands contain high concentrations of red or pink, indicating that the surface normal is approximately parallel to the basal pole with a slight trend towards the pyramidal direction (as shown in the legend of Figure 4-34).

The orientations of the samples sectioned for welding can be determined with reference to the original plate axes, as shown in Figure 4-35, Figure 4-36 and Figure 4-37. This was required for definition of the sample axes after the samples were placed in the microscope for the EBSD measurements.

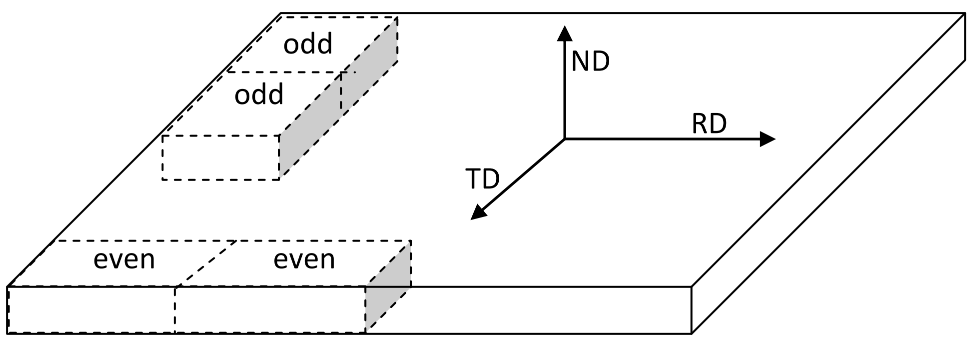

Figure 4-35: Samples sectioned from rolled plate: odd-odd: welding oscillation direction *parallel* to rolling direction; even-even: welding oscillation direction *perpendicular* to rolling direction (parallel to transverse).

Once the blocks had been sectioned from the original plate and welded, the samples themselves were numbered with odd or even sample numbers depending upon their orientation. Metallography samples were then sectioned from the welded blocks and designated “1” or “2” depending on whether the section was taken parallel or transverse to the oscillation direction, as shown in Figure 4-36 and Figure 4-37.

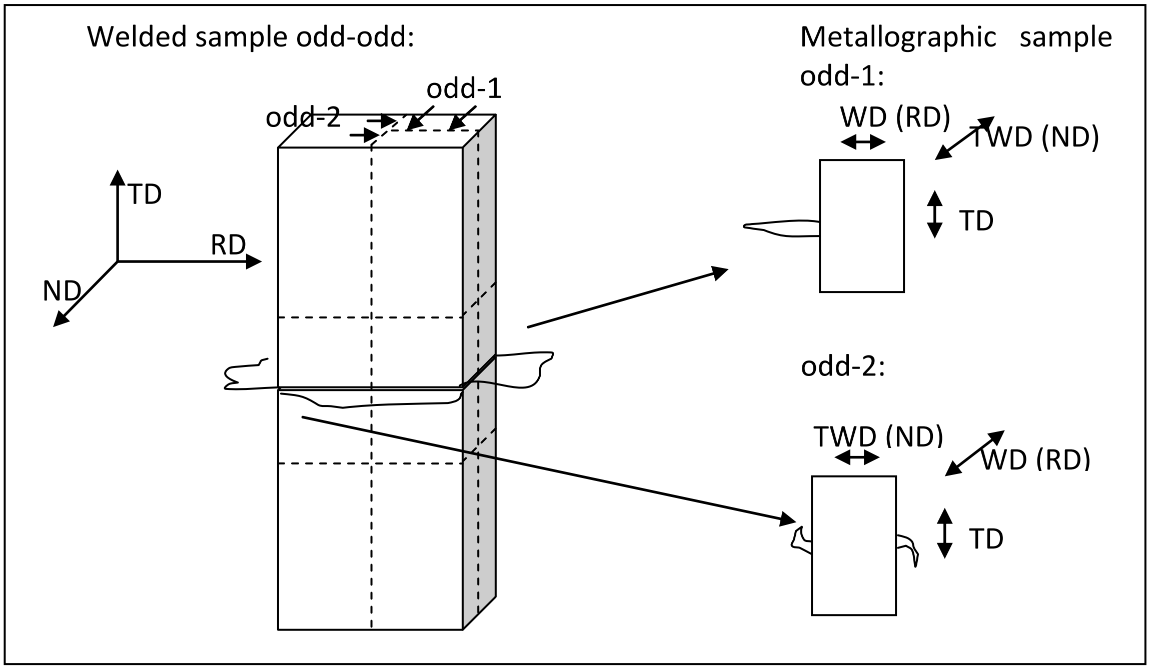

Figure 4-36: Odd-odd welded samples (weld oscillation direction parallel to RD)

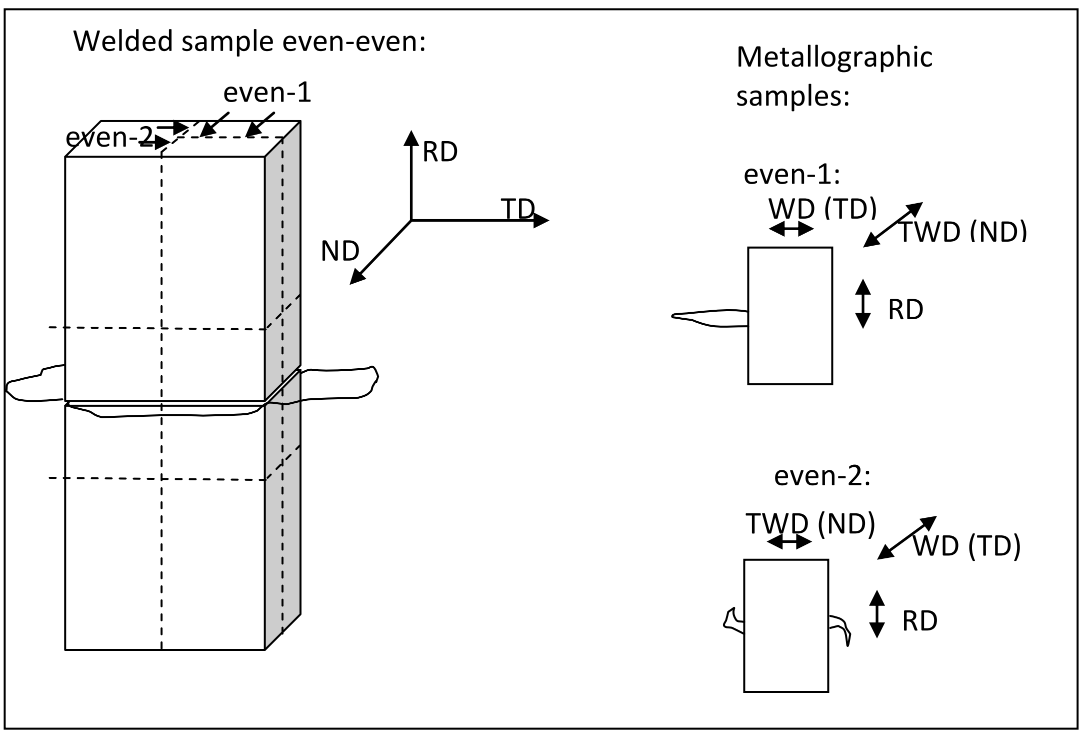

Figure 4-37: Even-even welding direction (weld oscillation direction perpendicular to RD)

A typical microstructure after LFW'ing of Ti-6Al-4V can be seen in Figure 4-38, with i) the large equiaxed grains of the parent material on the left giving way to ii) first deformed grains, then iii) finer deformed grains (which probably underwent recrystallization), and finally iv) a fully recrystallized zone in the centre close to the weld interface.

By comparing the pole figure representing the texture of the welded material, Figure 4-39, to that representing the as-received material, Figure 4-33, it can be seen that the texture of the material adjacent to the weld zone has been only slightly altered by LFW-ing parallel to the rolling direction. Here the data are taken from zone ii, the thermomechanically affected zone. Both Figure 4-39 and Figure 4-40, which represents the texture of material LFWed *perpendicular* to the rolling direction, closely resemble the as-received material save for small misalignments due to sectioning imprecision.

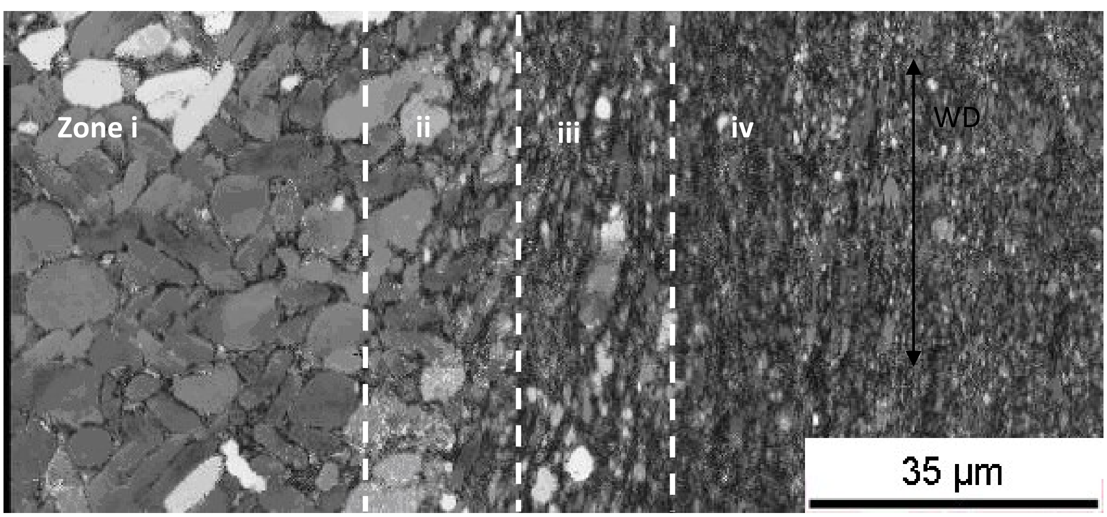

Figure 4-38: EBSD image quality map showing typical LFW microstructural zones

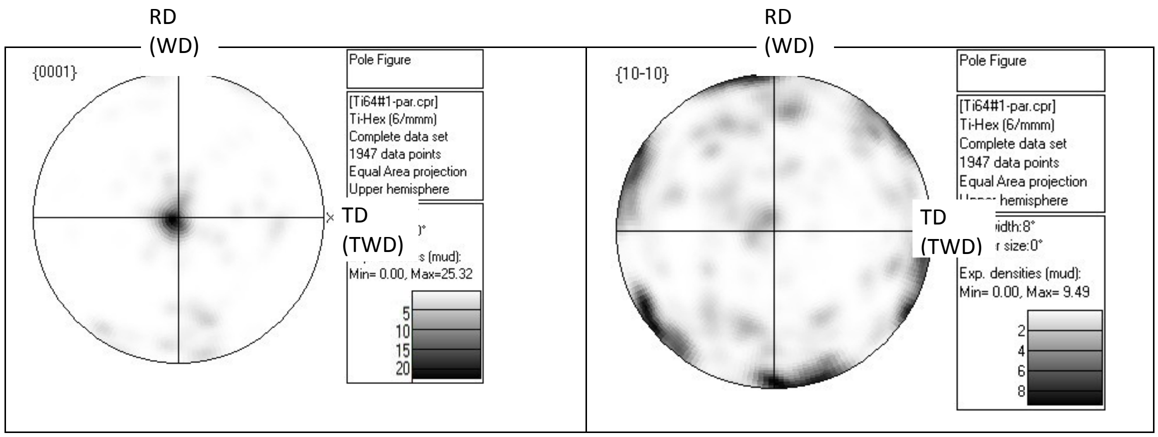

Figure 4-39: Pole figures of Ti-6Al-4V#1 welded parallel to RD, adjacent to the weld. Note that the original RD is now WD, and the original TD is now TWD.

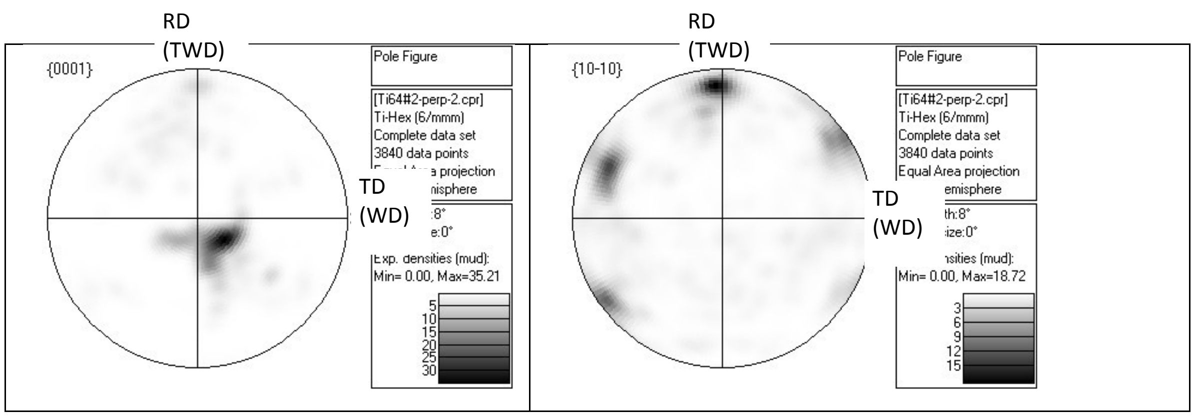

Figure 4-40: Pole figures of Ti-6Al-4V#2 welded perpendicular to RD, adjacent to the weld. Note that the original TD is now WD, and the original RD is now TWD.

A comparison of the orientation data collected for four sets of welding parameters is presented in Figure 4-41 in the form of both basal (0001) and prismatic (10-10) α pole figures, taken from three regions of each sample: i) undeformed and apparently unaffected grains; ii) large deformed grains; and iv) finer grains from the weld centre, presumed to be recrystallized. Due to the similarities between the textures of the fine deformed grains (zone iii as previously defined) and the weld line textures, the former are not presented here for all samples.

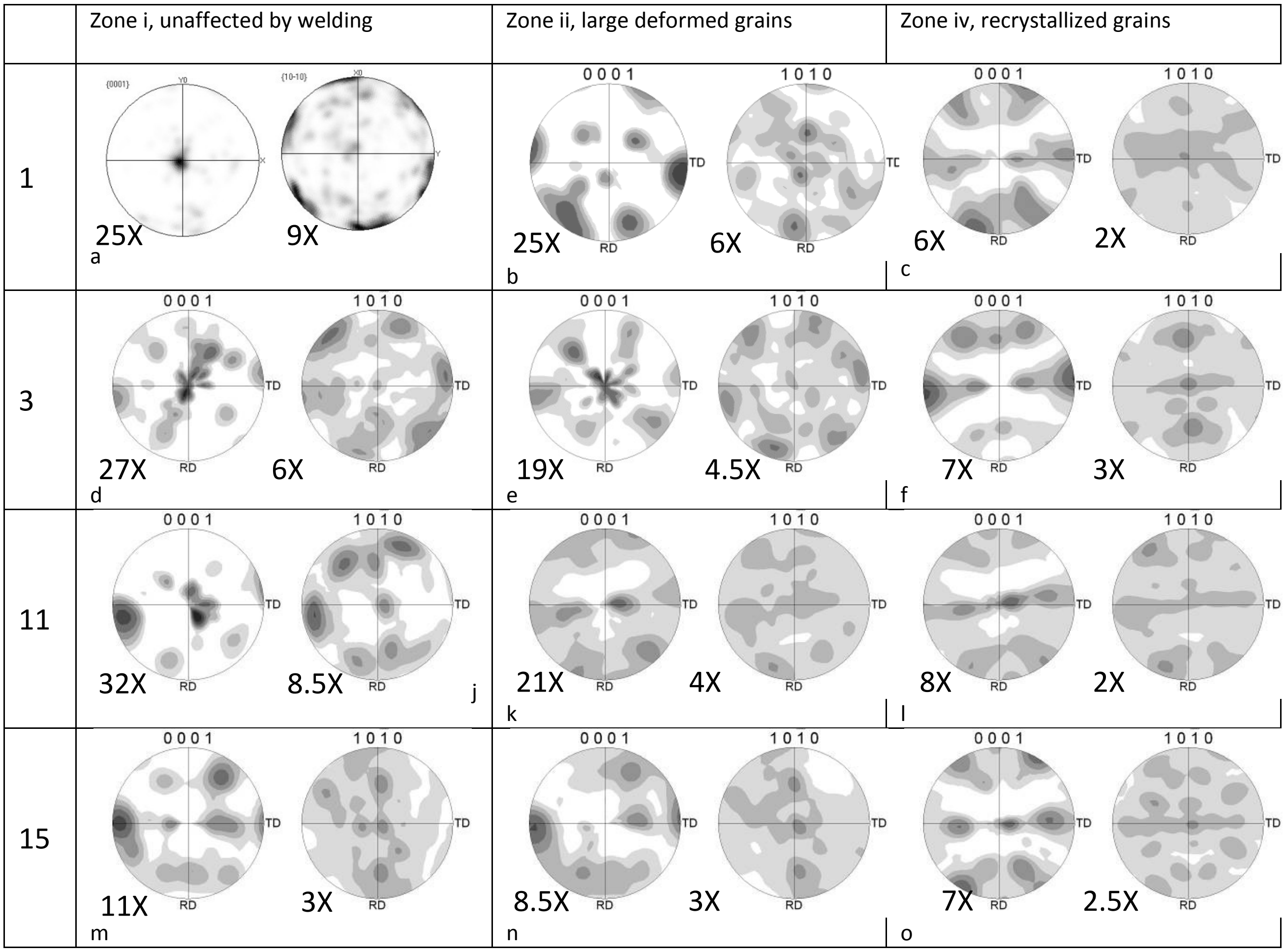

Figure 4-41: Basal and prismatic α pole figures for four weld conditions, showing from left to right figures for the unaffected, deformed, and recrystallized regions: (a,b,c) sample #1, 50 MPa/50Hz; (d, e, f) sample #3, 90 MPa/30Hz; (j, k, l) sample #11, 110MPa/50Hz; (m, n, o) sample #15, 90MPa/70Hz.

The β textures are not presented here at all due to the very small area fraction of β present. Numbers next to the pole figures (e.g. 8X) represent the intensities of the highest peaks in times random units. RD is equivalent to WD, and TD is equivalent to TWD.

The Kikuchi patterns shown in Figure 4-42 are intended to indicate the high quality of pattern obtained in general from the polished samples. This is a result of the careful development of a polishing process through research and optimization in order to obtain the most reliable and accurate EBSD data.

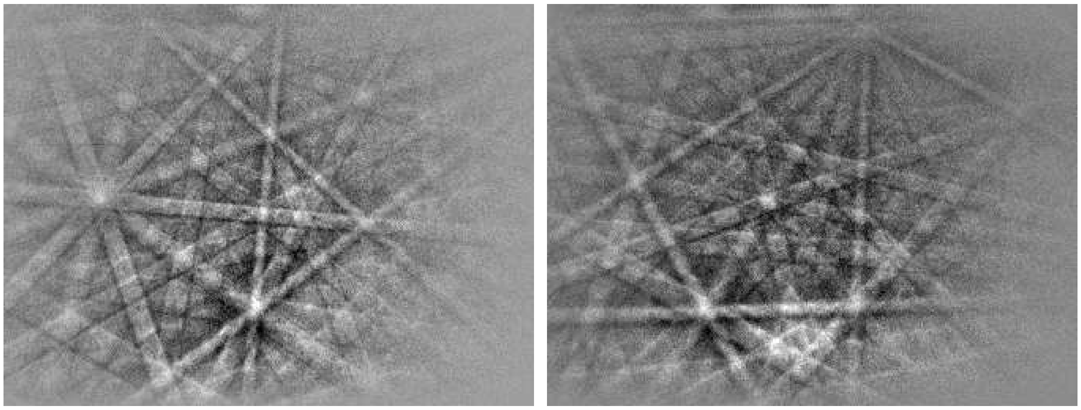

Figure 4-42: Sample Kikuchi patterns gathered from the Ti-6Al-4V samples

In addition to pole figures, inverse pole figure maps were generated for some specimens. Two representative maps are presented in Figure 4-43 and Figure 4-44.

In Figure 4-43 it can be seen that the two bands from the original banded structure (see Figure 4-34 for optical microstructure) visible in the as-received material have been scanned. While the texture of the acicular band is quite homogeneously pink (i.e. the surface normal is basal, with a slight shift towards the pyramidal), the texture in the more equiaxed band is much less uniform and shows a mixture of grains with basal as well as with pyramidal poles normal to the surface. It can also be noted that the largest and most distinct grains visible in the recrystallized zone are those that are red and that still appear elongated, as though they were deformed (and oriented) during welding and did not recrystallize.

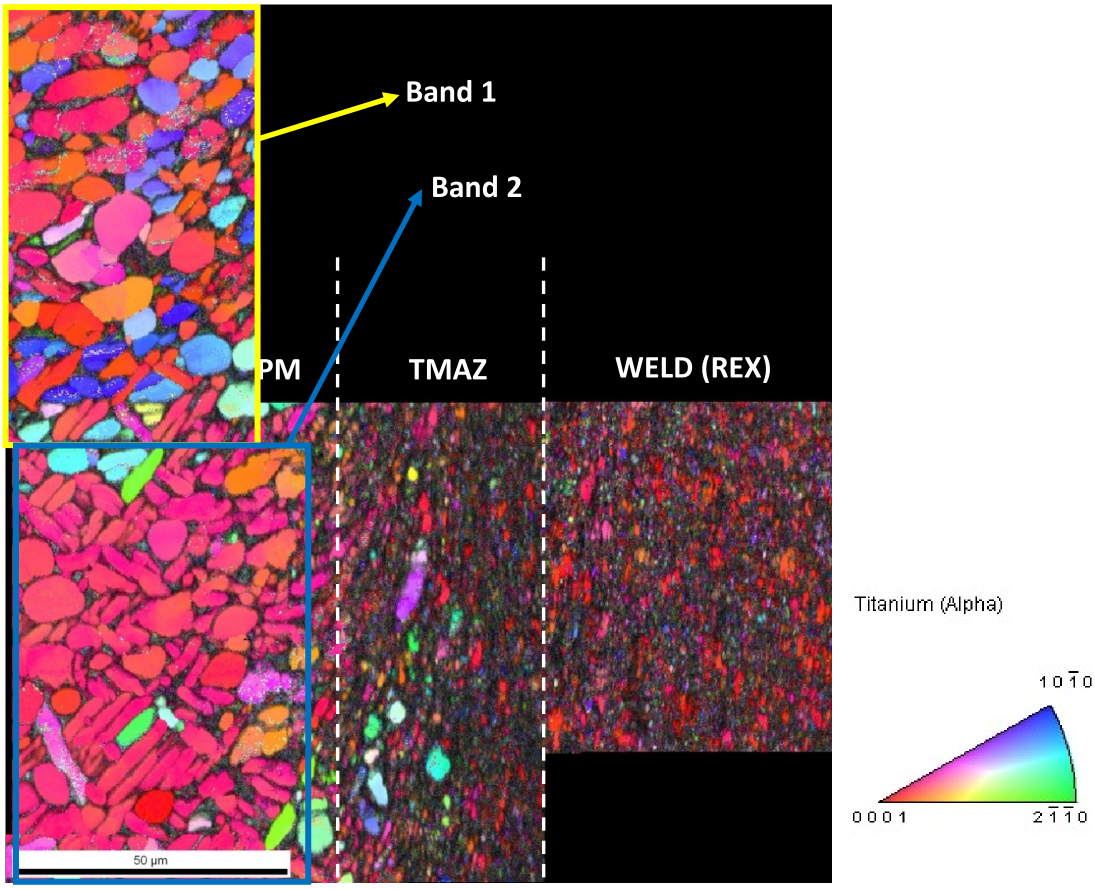

Figure 4-43: Ti-6Al-4V#11, EBSD inverse pole figure maps of α phase in recrystallized, deformed, and large grained areas have been juxtaposed to show transition as well as banding in parent material.

In Figure 4-44, depicting sample Ti-6Al-4V#15, a full overview of the parent material transitioning into the deformed zone, and finally into the recrystallized zone, can be seen. The flow of grains due to the oscillating motion of the welding can be clearly seen, as can the dramatic reduction in grain size going from the undeformed to the deformed and finally to the recrystallized zones. Also of interest is the fact that during deformation, the grains appear to maintain their original orientation, as can be determined from the fact that grains do not change colour as they flow. Specifically, at the beginning of the deformed zone, the band with a predominance of red grains (circled in white on the figure) continues with the same grain colours even when the grains are elongated and rotated.

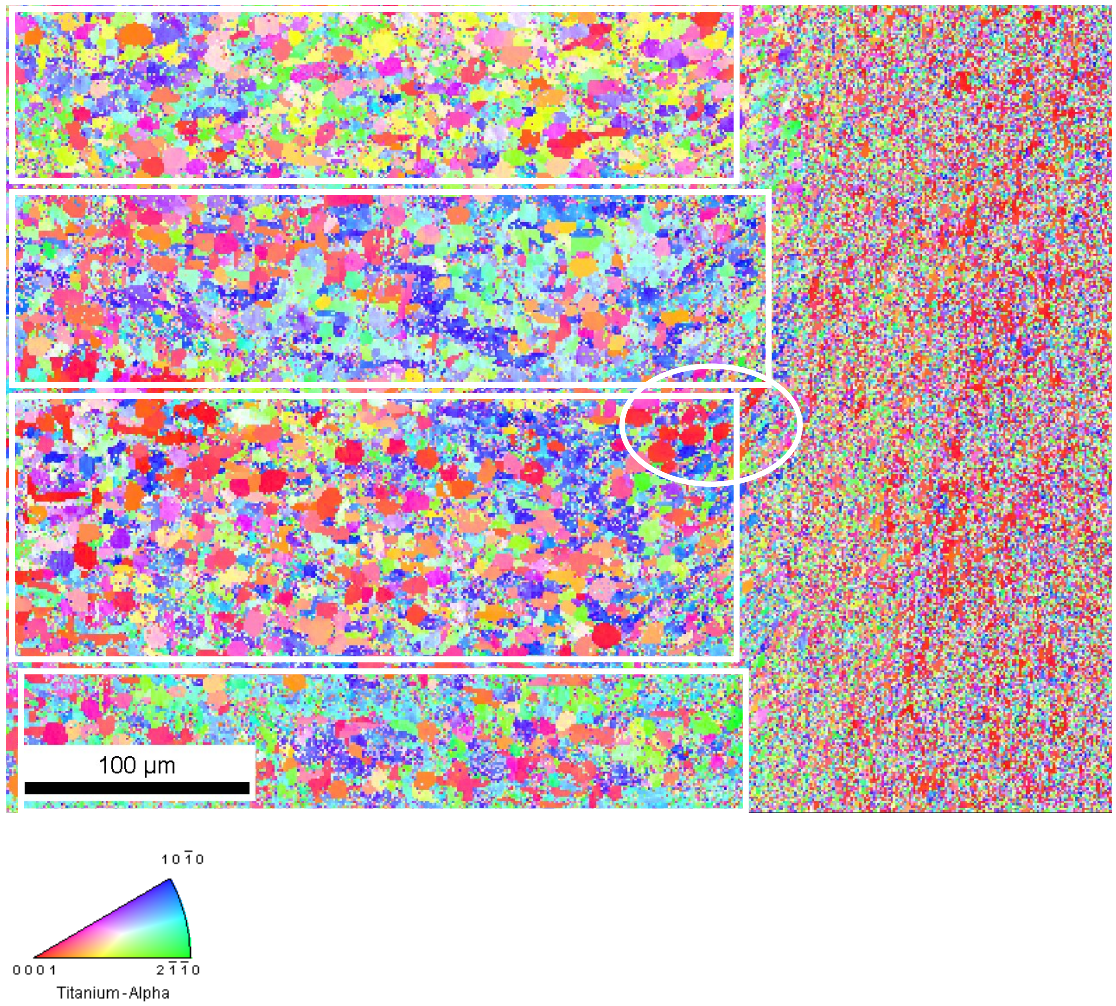

Figure 4-44: EBSD inverse pole figure map of α phase in Ti-64#15; an image quality map has been overlaid to make grain boundaries more visible. Original microstructurally distinct bands are broadly outlined in white rectangles.

Chapter 5

5 Ti-5553

Due to the literature indications that Ti-5553 would need heat treatment to attain its optimum strength and due as well to mechanical test results indicating that the untreated weld represents a weaker zone, heat treatments were applied to some Ti-5553 specimens both before and after welding. Specifics of the solution treated (ST) and solution treated and aged (STA) processes were given in Chapter 3, Experimental Procedure. One set of welding parameters was selected for all the heat-treated samples in order to simplify comparison.

Samples produced under each set of welding conditions, as well as most heat treatment conditions, were examined using EBSD. This was done mainly to acquire information about texture and phase partition but also to reveal the grain structure, given the difficulties of using ordinary optical and even SEM techniques. Only the samples from two welding conditions (but all heat treatment combinations) were mechanically tested.

Table 5-1: Summary of Ti-5553 samples (excluding repeats and failed tests).

Sample ID	Weld Parameters (Pressure-Frequency-Amplitude)	Pre-weld heat treatment	Post-weld heat treatment
Ti-5553#3	50 MPa-50 Hz-2 mm;	Ø	Ø
Ti5553#6	70 MPa-30 Hz-2 mm	Ø	Ø
Ti5553#9	50 MPa-110 Hz-2 mm	Ø	Ø
Ti5553#14	50 MPa-50 Hz-2 mm;	ST	ST
Ti5553#15	50 MPa-50 Hz-2 mm;	ST	STA
Ti5553#16	50 MPa-50 Hz-2 mm;	ST	Ø
Ti5553#17	50 MPa-50 Hz-2 mm;	Ø	ST
Ti5553#18	50 MPa-50 Hz-2 mm;	Ø	STA

Note: shaded rows indicate the baseline weld parameters; the heat treatment series all use these same weld parameters.

The microstructures of the as-received Ti-5553 material revealed by optical microscopy and scanning electron microscopy (SEM) are shown in Figure 5-1. At low magnification, Figure 5-1a, extremely large β grains averaging 100 to 500 µm in diameter are visible. The high magnification optical and SEM images, Figure 5-1b and c, reveal an acicular microstructure within the β grains. Some of the large β grain boundaries can be seen in both high magnification images.

This as-received microstructure is consistent with that expected for an ingot structure [9] that has not been subjected to any secondary operations, such as thermomechanical processing or solutionizing and/or aging heat treatments.

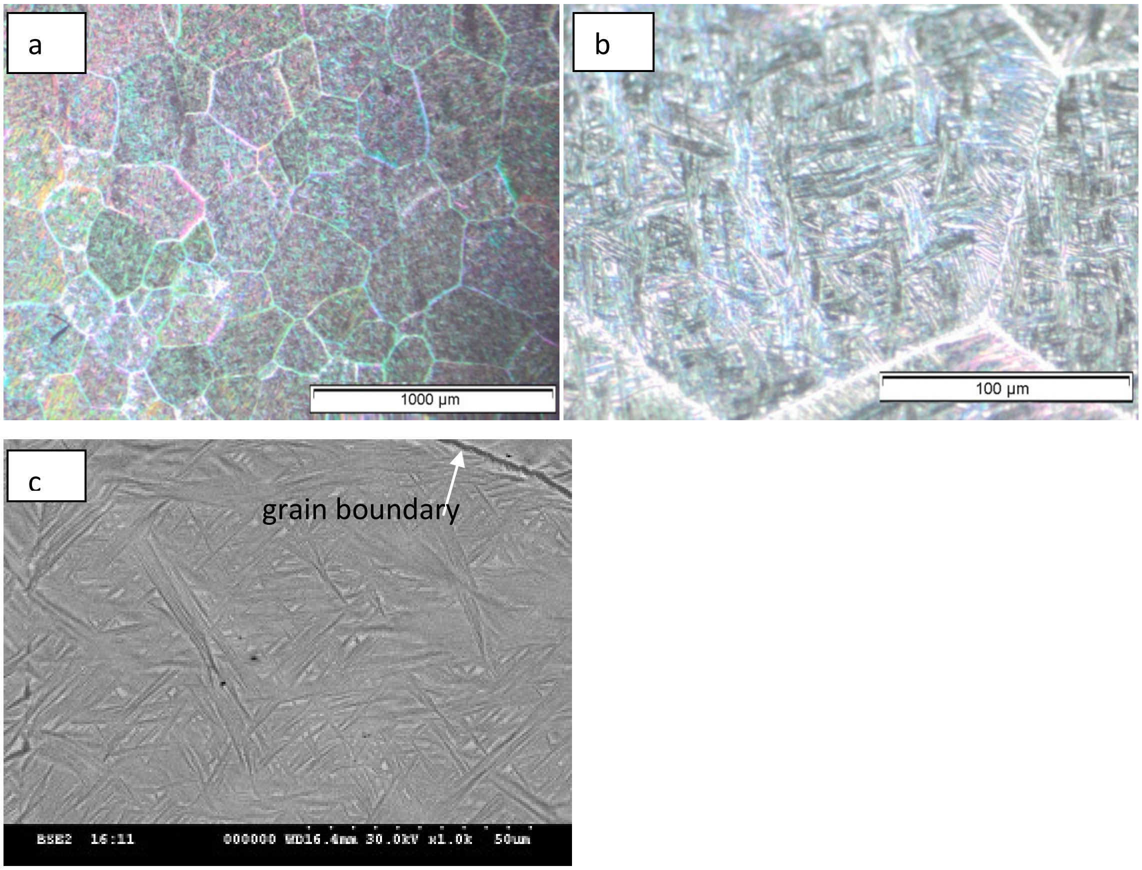

Figure 5-1: Parent material showing (a) a dark field optical image of the large equiaxed grains (Kroll's reagent), (c) high magnification dark-field optical image (Kroll's reagent) and (b) high magnification BSE image of acicular substructure using compositional contrast (mirror polished).

5.1 Microstructural Evolution

Visual inspection of the interface region in the LFWed Ti-5553 shows an appreciable flash from all four sides of the joint (Figure 5-2) for all conditions tested, suggesting that the weld is integral [6, 33]. As in the case of the Ti-6Al-4V behaviour, the flash length was found to be larger in the direction of the oscillatory movement, i.e., parallel to the specimen long axis as compared to along the specimen width. However, unlike LFWed Ti-6Al-4V, which exhibited a series of ridges on the flash extruded in the direction of the reciprocating motion, the LFWed Ti-5553 flash, though rough on the outer surface, displayed no regular ripples under the process conditions examined. As the flash layer consists of plastically deformed material extruded during the welding process, the difference in the flow behaviours of the two alloys (α+β versus near-β) is almost certainly responsible for the difference in flash morphology. The differences in the flow characteristics of the two materials is further discussed in Chapter 7, section 7.2.

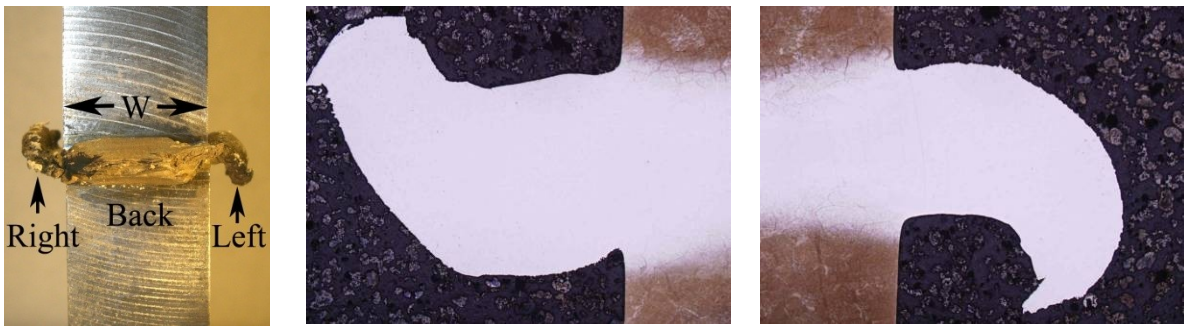

(a) (b) (c)

Figure 5-2: (a) As-welded Ti-5553#3 showing (b) right and (c) left side flash cross-sections.

Some microstructures of the welded sample Ti-5553#3 are illustrated in Figure 5-3. At high magnification using optical microscopy, faint indications of grain boundaries can be seen but, overall, the grains along the weld centre (Figure 5-3a) are not effectively revealed through chemical etching.

The low etching response is attributed to the highly deformed and dynamically recrystallized microstructure in the weld zone. The region adjacent to the weld centre is presented in Figure 5-3(b); here a few more equiaxed grains are visible, as well as some indication of an acicular structure in certain regions between the recrystallized grains. In the micrograph of Figure 5-3(c), representing the structure about 0.4 mm from the weld line, this acicular structure is clearly revealed. Finally, in Figure 5-3(d) 1 mm from the weld line, the undeformed acicular microstructure that is characteristic of the as-received material (Figure 5-1b) can be seen clearly. These micrographs are quite representative of all the welded Ti-5553 samples; thus micrographs for the other conditions will not be presented.

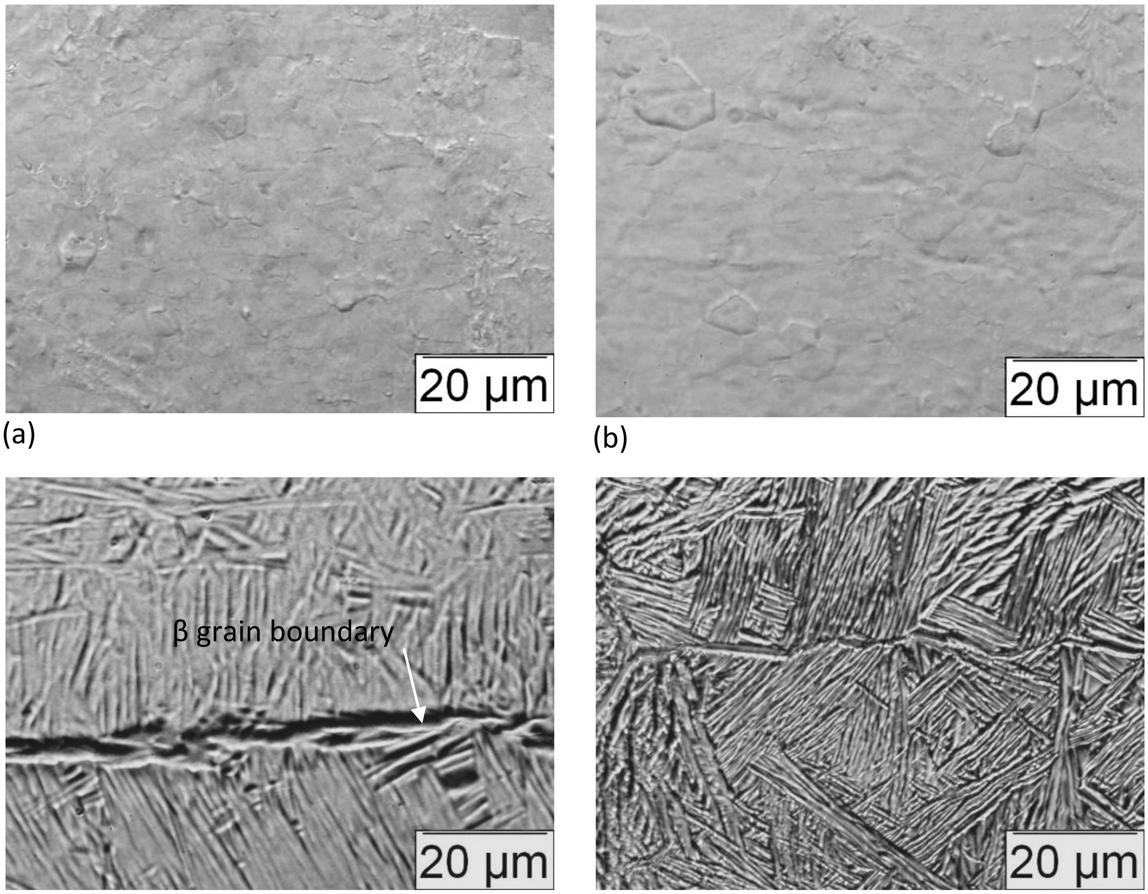

(a) (b) (c) (d)

Figure 5-3: Ti-5553#3 (Kroll's reagent): (a) weld centre at high magnification, (b) 100 µm from weld centre, (c) 400 µm from weld centre and (d) 1 mm from weld centre.

5.2 Mechanical testing

The microhardness profiles shown in Figure 5-4 and Figure 5-5 reveal that the weld region is somewhat softer than the surrounding TMAZ, which in turn is softer than the surrounding parent material; this is consistent with the microstructural observations of α depletion in the weldment [63]. Sample Ti-5553#3, welded at a lower pressure and higher frequency, can be seen to display a pronounced hardness drop in the weld with a sharp drop over the range +/- 1.6 mm. Meanwhile Ti-5553#6, the higher pressure/lower frequency sample, displays less softening in the weld centre and a slightly less abrupt drop that, however, spans a wider region, as indicated by comparison with the parent metal (PM) hardness range (shaded in pink on Figure 5-4 and Figure 5-5). It is worth noting that, as the size of the indentation is comparable to that of the weld thickness, the hardness results may not accurately capture the exact onset and peak of softening in the weld zone. Nevertheless, the thicknesses of the softened regions in the two samples are consistent with the weld zone thicknesses observed in the EBSD scans.

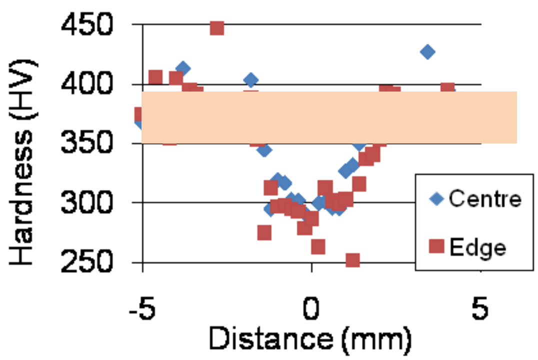

Figure 5-4: Microhardness profile across weld line for sample Ti-5553#3 (baseline pressure and frequency).

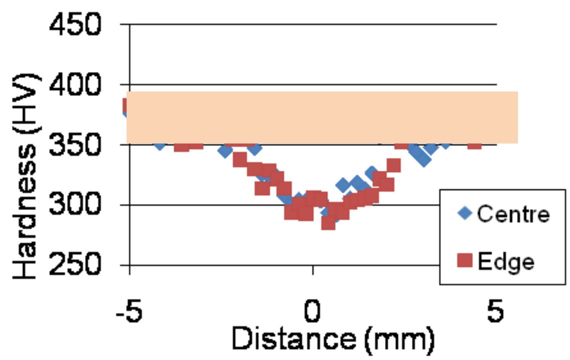

Figure 5-5: Microhardness profile across weld line for sample Ti-5553#6 welded at low frequency and high pressure.

In an effort to improve the resolution of the size of the softened zone defined by the microhardness profiles, nanoindentation testing was performed on samples Ti-5553#3 and Ti-5553#6. First, a calibration series was run in order to be sure of using a load that would not be subject to any indentation size effect. It can be seen from the two series indented in the weld region and the two in the parent material (Figure 5-6) that, at a load of 5000 µN (which is to say 5 mN), the value of H has reached a plateau, indicating that this is the correct hardness reading and not a result of residual stresses at the surface, or more complex effects related to dislocation pile-up [64].

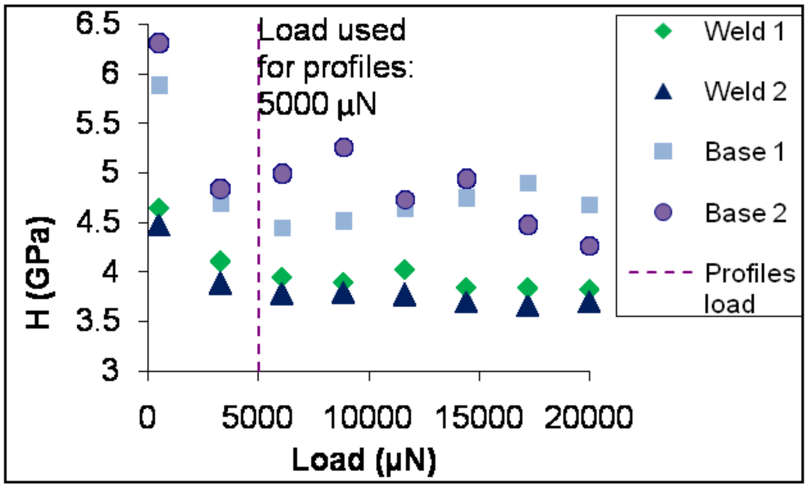

Figure 5-6: Nano-indentation varying load series performed within the weld and in the parent material to rule out indentation size effect.

Following the calibration, three series of indentations were made across the weld region from the unaffected zone on one side to that on the other. The averaged results are presented in Figure 5-7 and Figure 5-8. With the finer resolution of the nanoindentation process as compared with microhardness, it can be seen that there is in fact very little difference between the two weld regions in either hardness or thickness.

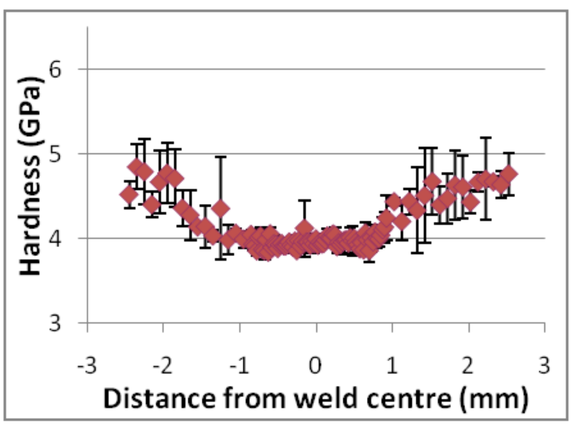

Figure 5-7: Ti-5553#3-2 Nanoindentation cross-weld profile

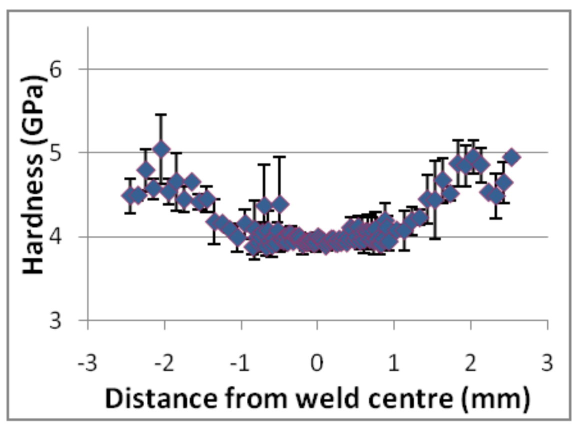

Figure 5-8: Ti-5553#6-2 Nanoindentation cross-weld profile

Tensile testing was performed on both the as-received and the welded specimens. Since this alloy is used mainly in structural applications such as landing gears and not under higher temperature conditions such as in engines, the use of room temperature tensile tests is appropriate. The first as-received values in Table 5-2 are for the material that was not heat treated and are thus lower than literature values quoted for solutionized and aged Ti-5553. The large variation in the % El. observed is consistent with previous findings for a billet structure without STA. By contrast, Fanning has reported [58] less variation in the elongation when the microstructure of Ti-5553 is homogenized using STA. Following the *untreated* as-received values are the values for as-received material that was subjected to the ST and STA heat treatments. In the unwelded condition the properties of the STA samples approach the literature values much more closely than do those of either the untreated or the ST samples (see the first three rows of Table 5-2). In the un-heat-treated samples, the YS, UTS and % El. values are lower for the LFWed samples as compared to the as-received tensile properties.

Table 5-2: Ti-5553 tensile testing results

Sample ID-PreWHT/PostWHT	YS (MPa)	UTS (MPa)	Uniform El. (%)	Total El. (%)
As-received	1046±13	1108±25	7.4±3.0	11.2±6.5
As-received ST	889±4	917±0.5	2±0.2	7.4±0.7
As-received STA	1266±18	1283±30	2±0.4	2.2±0.4
Ti-5553#3-Ø/Ø	1019±19	1058±23	3.0±0.5	4.0±1.0
Ti-5553#6-Ø/Ø	988±16	1013±10	2.0±0.1	2.9±0.9
Ti-5553#14-ST/ST	883±24	910±13	1.7±0.1	4.8±4.2
Ti-5553#15-ST/STA	1242±20	1214±63	1.3±0.4	1.3±0.4

Engineering stress-strain curves for the untreated, ST, and STA sets of specimens, both as-received and welded, are presented in Figure 5-9, Figure 5-10, and Figure 5-11 respectively. In these graphs, the “A” and “B” designations refer to two directions, normal to each other, along which the as-received specimens were sectioned. As this material was not rolled but cut from an ingot, the orientation variation was introduced merely to confirm that the as-received material was not highly anisotropic.

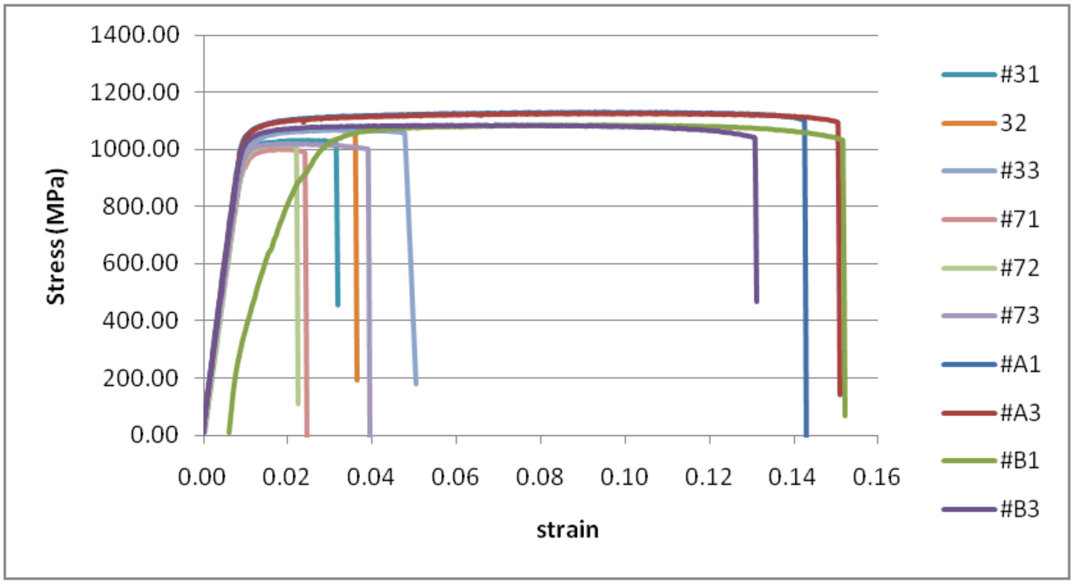

Figure 5-9: Engineering stress-strain curves for the non-heat-treated Ti-5553 specimens.

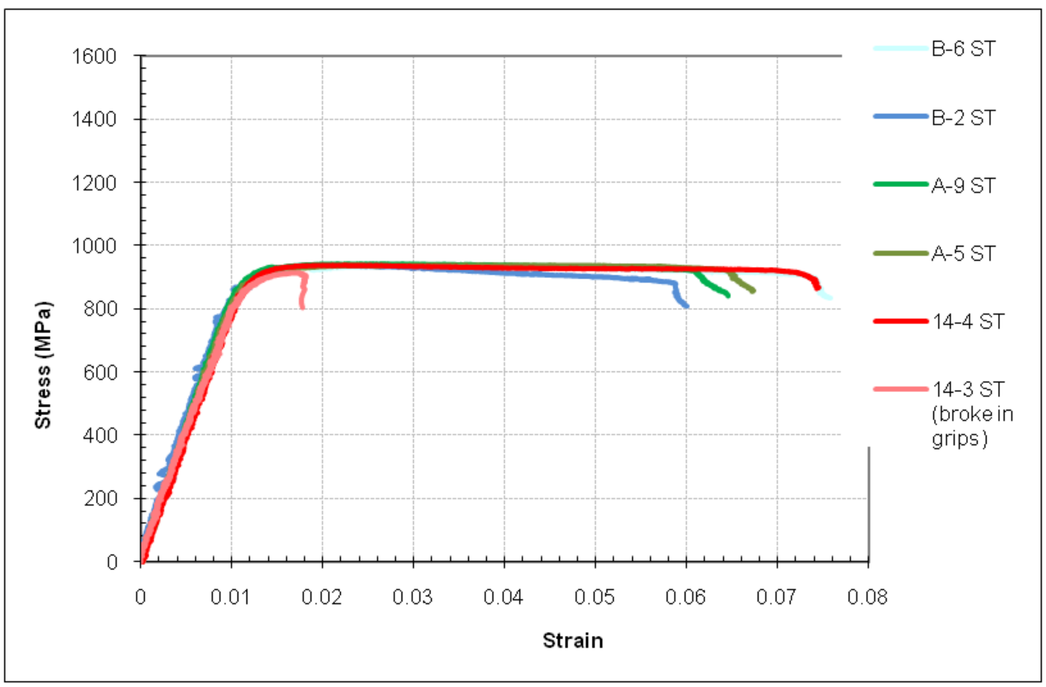

Figure 5-10: Engineering stress-strain curves for the solution treated Ti-5553 specimens.

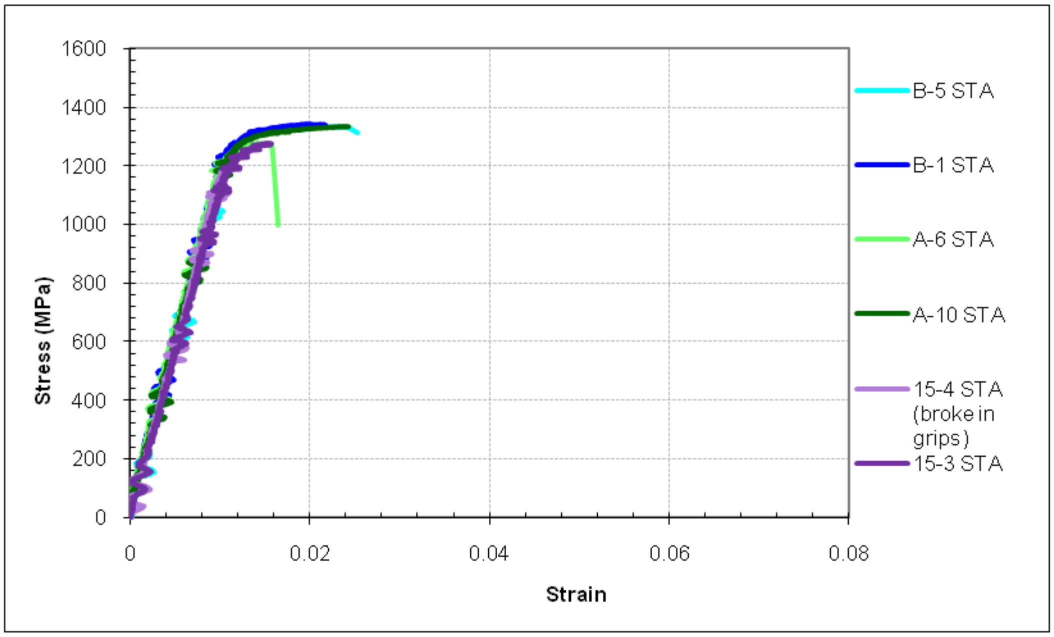

Figure 5-11: Engineering stress-strain curves for the solution treated and aged Ti-5553 specimens.

The fracture surfaces of the welded tensile coupons revealed the presence of very large grains (see Figure 5-12); these are consistent with fracture occurring in the TMAZ adjacent to the recrystallized weld zone. Both unwelded and welded samples displayed ductile fracture characteristics with some areas of shear. In fact, all the welded specimens fractured in the TMAZ within 1 mm of the weld zone, as shown in Figure 5-13. Conversely, the as-received (unwelded) tensile specimens fractured at random locations along their gauge lengths.

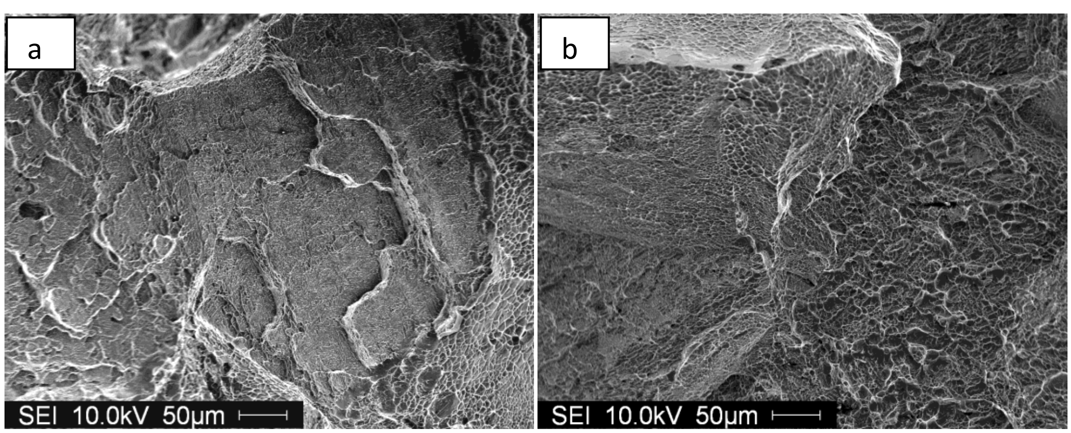

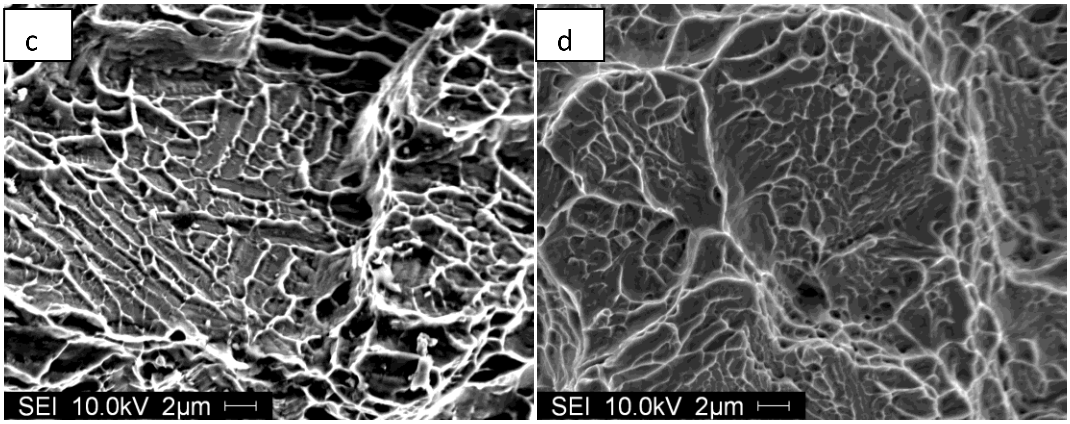

Figure 5-12: SEM images of fracture surfaces: a) as-received, low-mag; b) welded, low-mag; c) as-received, high-mag; d) welded, high-mag.

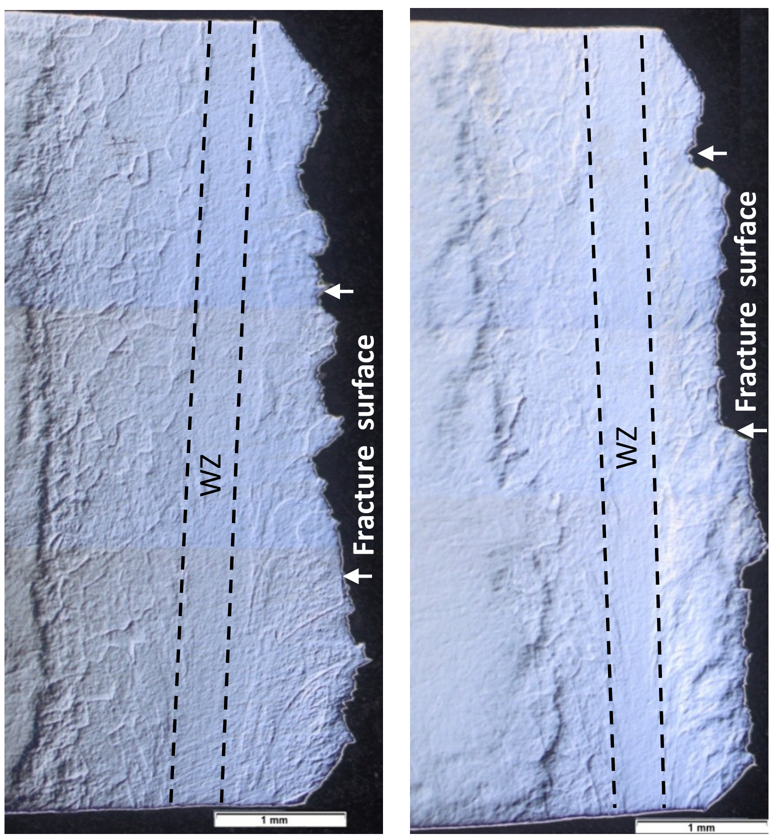

(a) (b)

Figure 5-13: Polarized light micrographs of fractured tensile bars (a) Ti-5553#3 and (b) Ti-5553#6.

An example of the strain distribution in the unwelded condition is presented in Figure 5-14. This should be compared with that of the welded Ti-5553#3 in Figure 5-15. The region of strain concentration indicated (in red) as the area of highest intensity in the welded specimen corresponds to the location of the fracture that occurred immediately afterward.

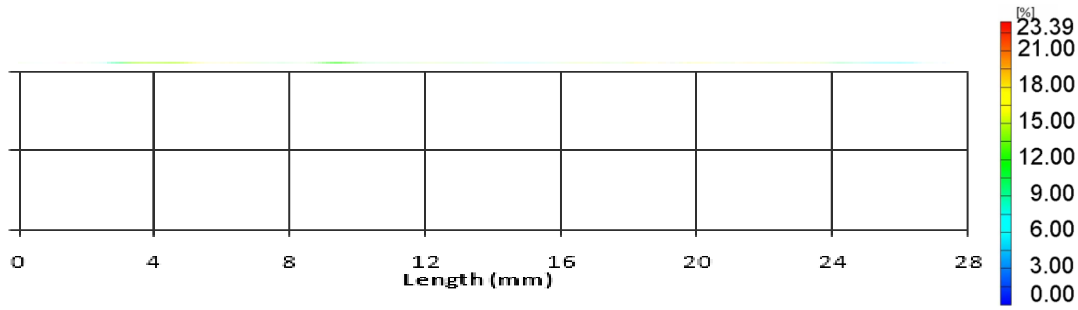

Figure 5-14: Strain distribution in deformed as-received Ti-5553 just before fracture.

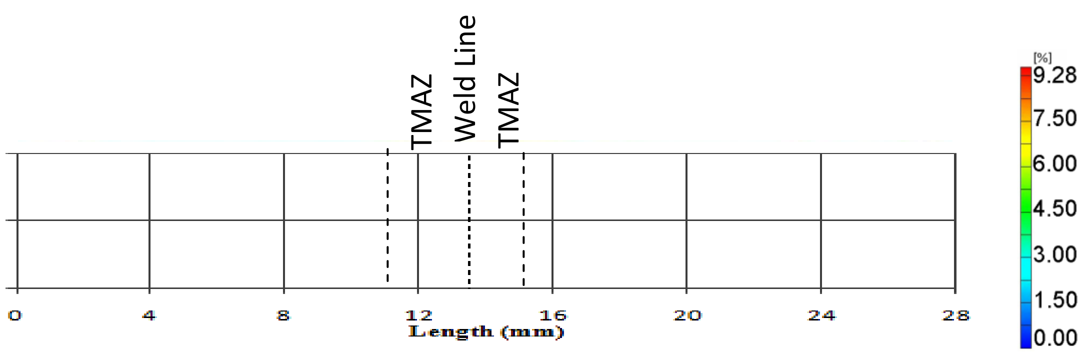

Figure 5-15: Strain distribution in deformed *welded* Ti-5553#3 just before fracture.

5.3 Microtexture measurements

To reveal the details of the weld microstructure, including delineation of the grain boundaries and phase divisions, orientation data were obtained from the as-received material and the LFWed samples. Scans of the as-received material are presented in Figure 5-16 and Figure 5-17. The α phase area fraction in this sample is approximately 3.4%, which is equivalent to 3.4% volume fraction. The α phase can be seen to be mainly clustered about the β grain boundaries. These α phase clusters do not appear to display any strong texture as a group, though they may have an orientation relationship with the adjacent β grains.

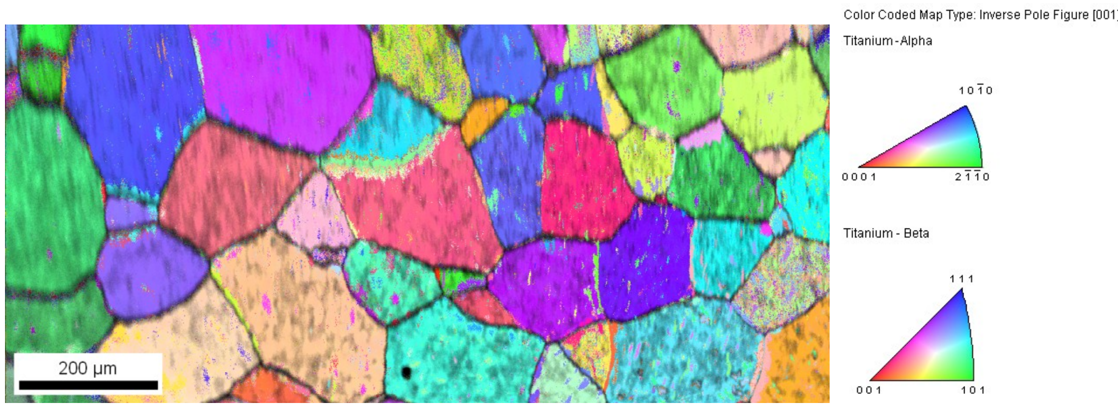

Figure 5-16: EBSD inverse pole figure map of as-received Ti-5553.

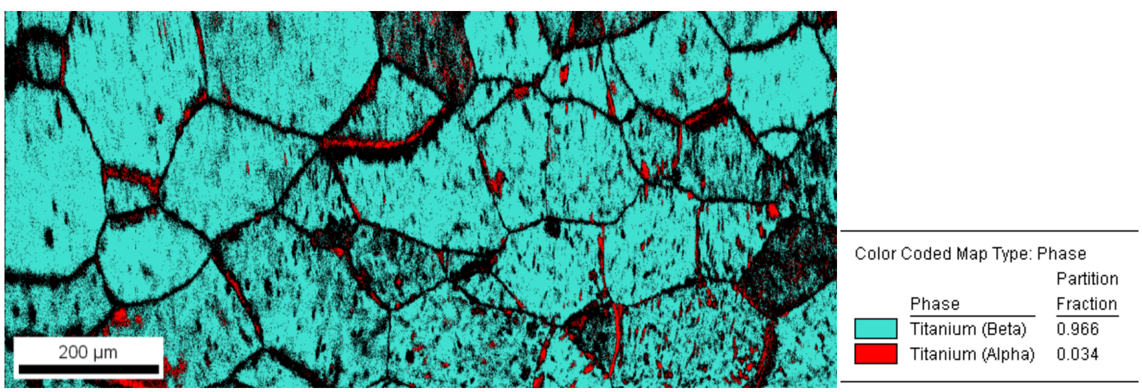

Figure 5-17: EBSD phase map of as-received Ti-5553.

The welded samples presented for this alloy were sectioned transverse to the weld oscillation direction and perpendicular to the weld plane, as shown in Figure 5-18. Note that as there was no initial deformation texture in the material, the usual “RD, TD, ND” designations have been replaced by weld oscillation direction (WD), transverse to weld oscillation (TWD), and normal to weld plane (ND). In Figure 5-19, an inverse pole figure map of welded sample Ti-5553#3 can be seen. An image quality map is overlaid in order to define the grain boundary locations.

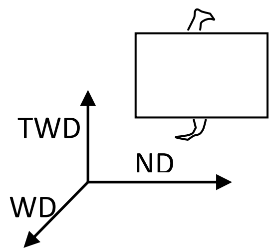

Figure 5-18: Sectioning schematic for metallographic samples.

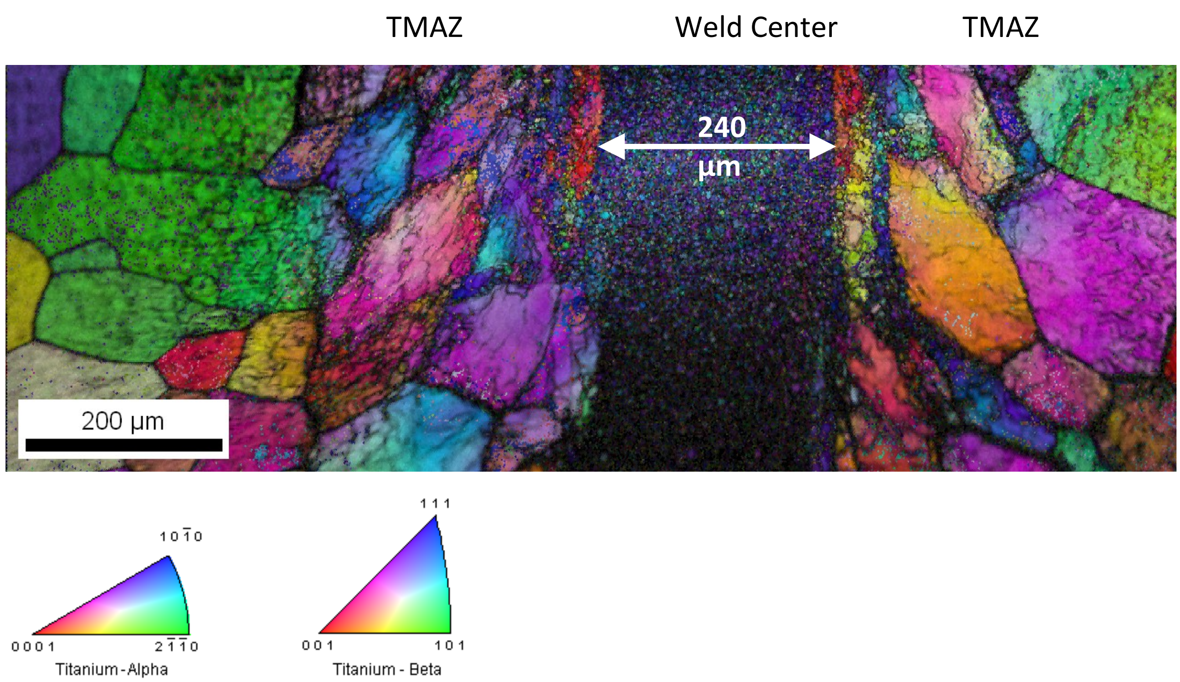

Figure 5-19: Ti-5553#3 image quality + inverse pole figure map (transverse cross-section)

From Figure 5-20, it can be seen that there is an overall α phase area fraction of 0.4% in sample Ti-5553#3. The α fraction decreases to nearly none (estimated at 0.05%) in the recrystallized weld zone. The thickness of the recrystallized zone in sample Ti-5553#6 (see Figure 5-21 and Figure 5-22) averages 380 µm at the narrowest point (weld centre). Once again, the recrystallized zone consists almost entirely of fine grains oriented with their <111> directions normal to the surface. A close-up scan of this recrystallized region can be seen in Figure 5-23. The phase fraction map confirms the earlier finding in the lower resolution scan that there is little or no α present in these grains, as compared with the TMAZ, which contained 0.5 to 1% volume fraction of α.

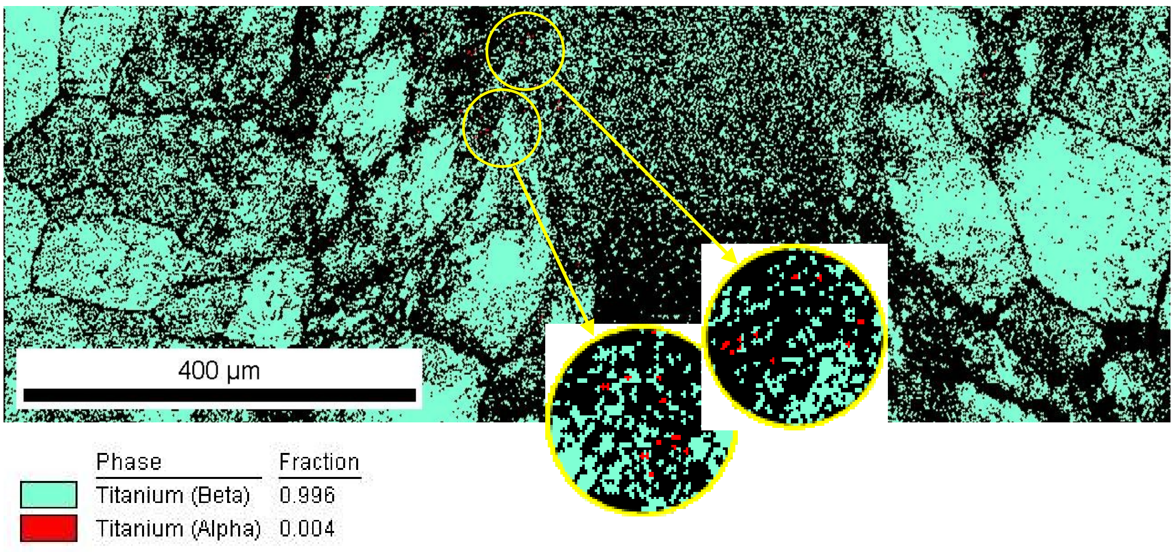

Figure 5-20: Phase fraction map of Ti-5553#3; points with confidence index below 0.2 removed.

TMAZ Weld Center

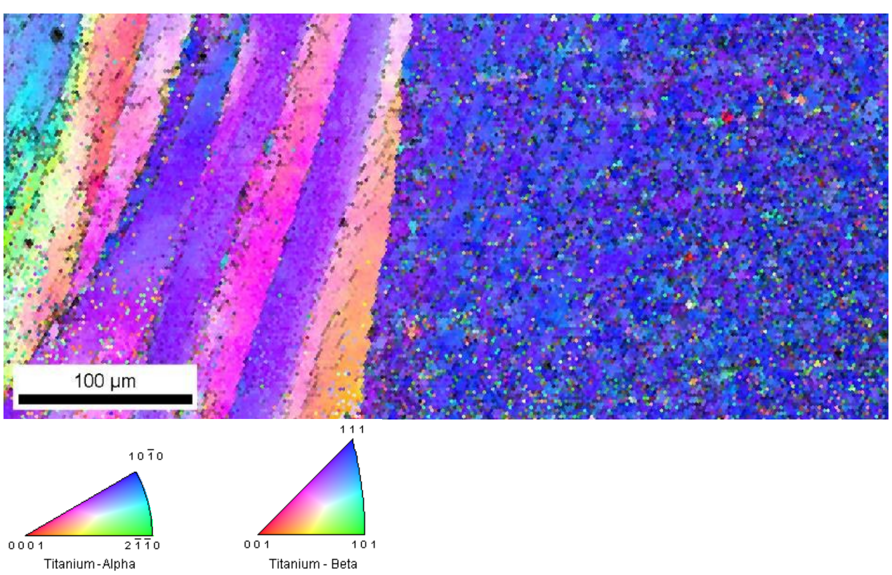

Figure 5-21: Inverse pole figure map of Ti-5553#6 showing one side of weld zone with adjacent deformed grains.

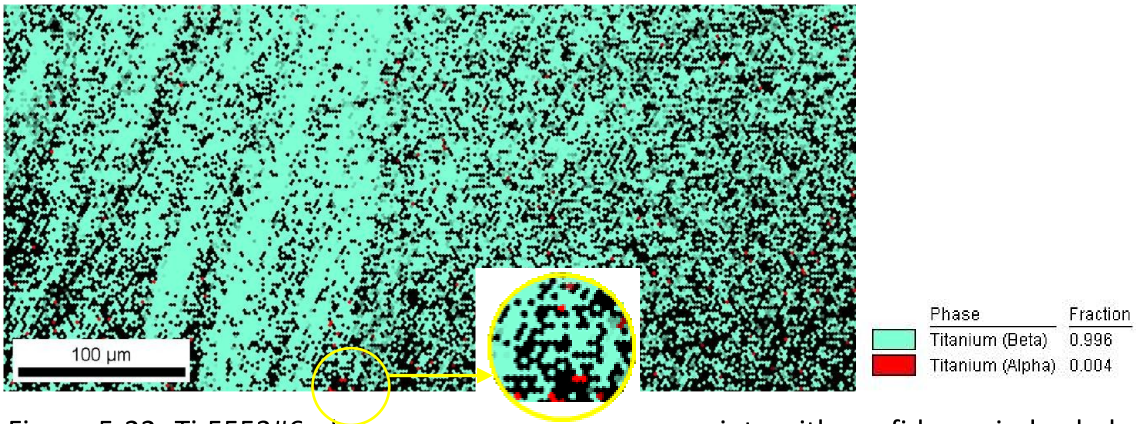

Figure 5-22: Ti-5553#6 phase map; step size 2 µm; points with confidence index below 0.2 removed.

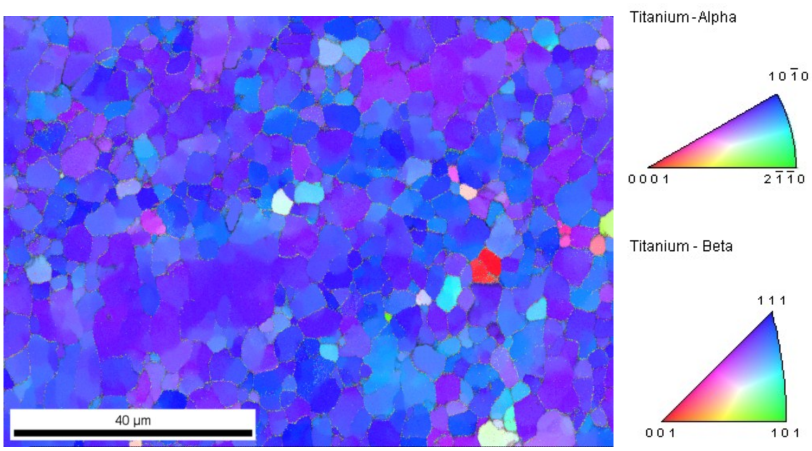

(a)

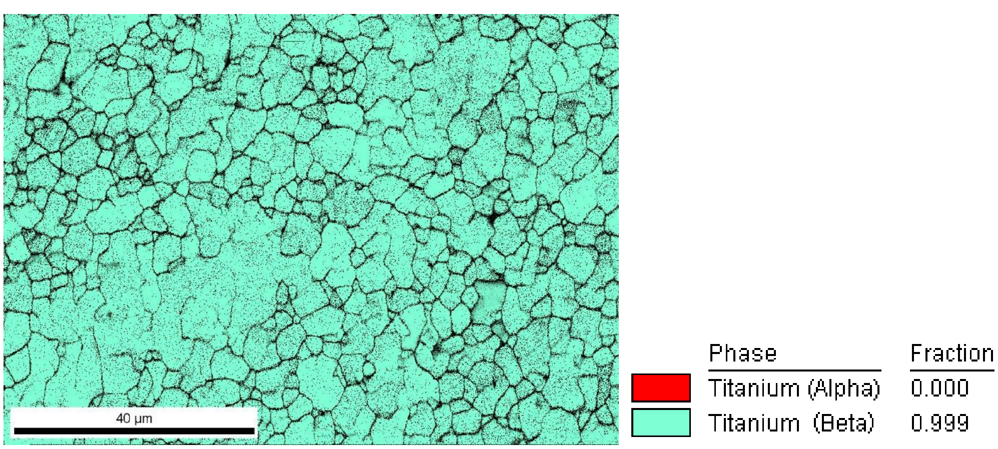

(b)

Figure 5-23: High resolution scan of equiaxed grain zone of Ti-5553#6 at step size 0.10 µm: (a) Inverse pole figure map + image quality map; (b) phase map.

Inverse pole figure (IPF) maps and phase maps for samples #9, #14, and #15 are presented in Figure 5-24 through Figure 5-33. Sample Ti-5553#9, as summarized in Table 5-1, represents the specimen prepared with the most aggressive weld parameters. The effect of this can be observed in the fact that the weld zone is narrower than in samples prepared at lower specific power inputs, as seen previously with Ti-6Al-4V (see Chapter 4).

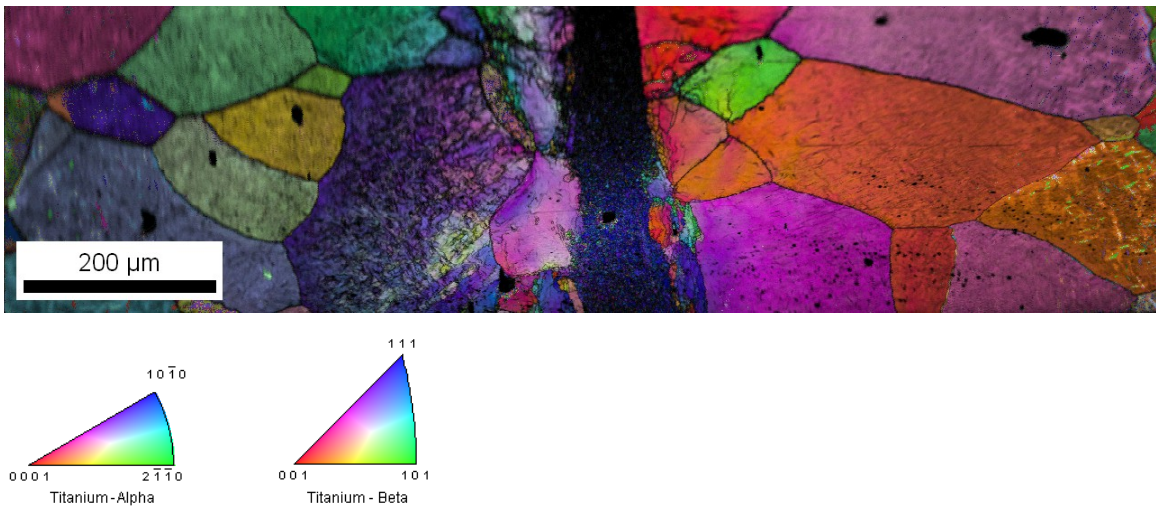

Figure 5-24: EBSD IPF scan of Ti-5553#9 (transverse section).

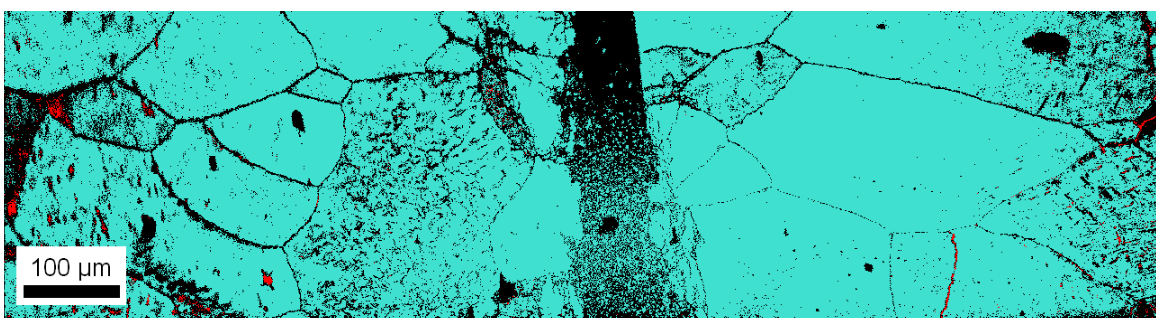

Color Coded Map Type: Phase

Phase	Total Fraction	Partition Fraction
Titanium (Beta)	0.823	0.994
Titanium (Alpha)	0.005	0.006

Figure 5-25: EBSD Phase map of Ti-5553#9

Samples #14 and #15 are respectively the solution treated and the solution treated and aged specimens. The phase maps show clearly the evolution of the α phase through these heat treatment processes, with special emphasis placed on the extensive presence of grain-boundary α in sample #15.

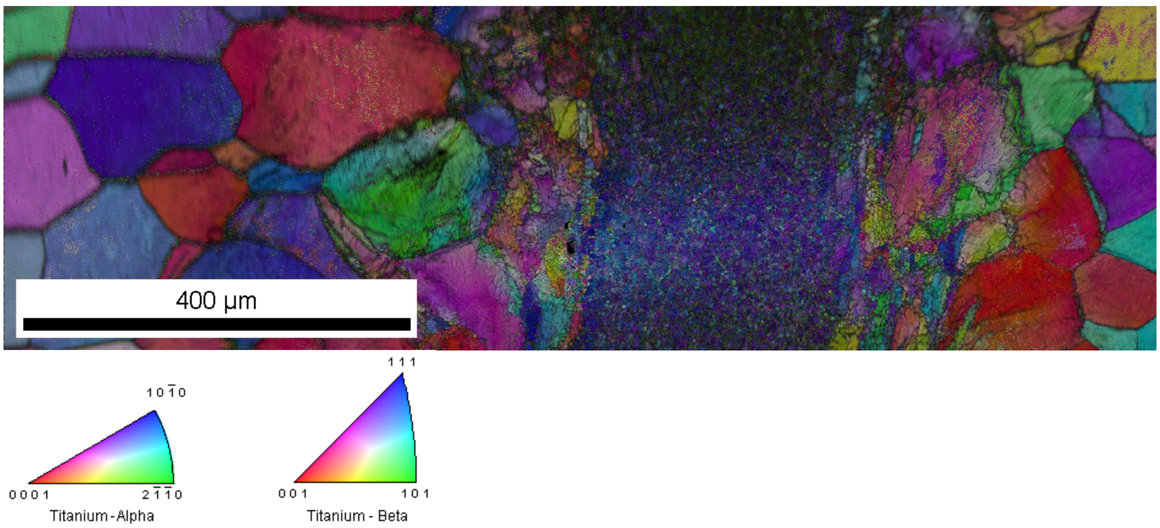

Figure 5-26: EBSD IPF scan of Ti-5553#14, solution heat treated (ST) after welding.

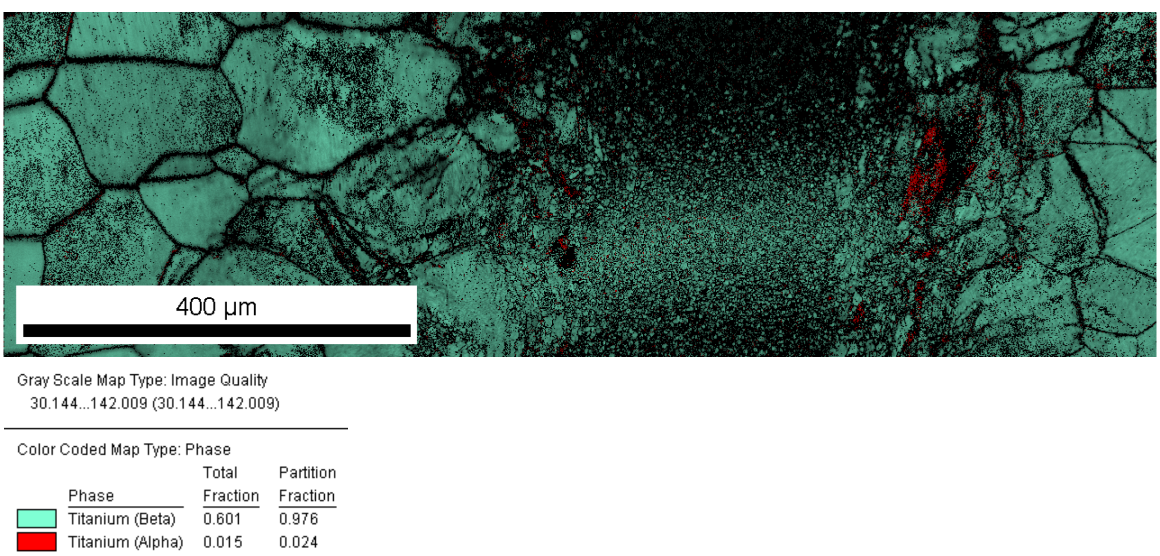

Figure 5-27: EBSD phase map of Ti-5553#14 ST after welding.

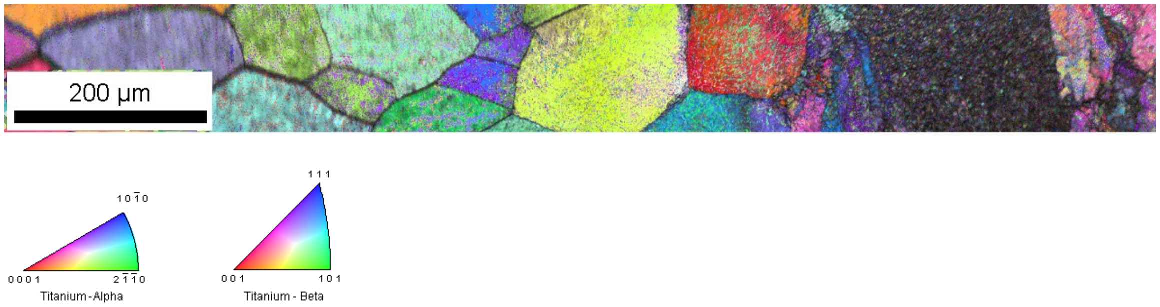

Figure 5-28: Ti-5553#15 solution treated and *aged* (STA) after welding.

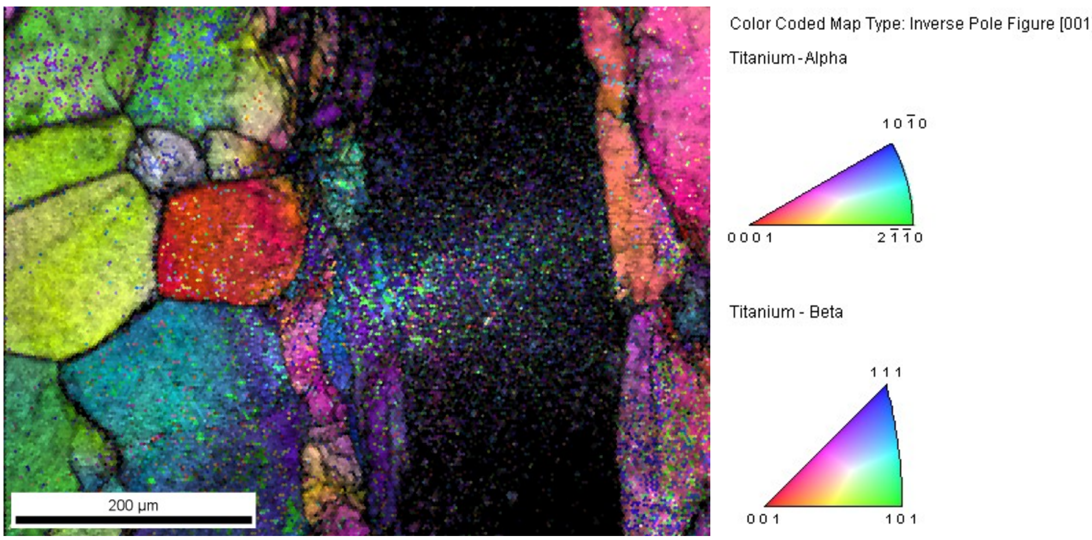

Figure 5-29: Ti-5553#15 STA after welding. Close-up of weld and surroundings.

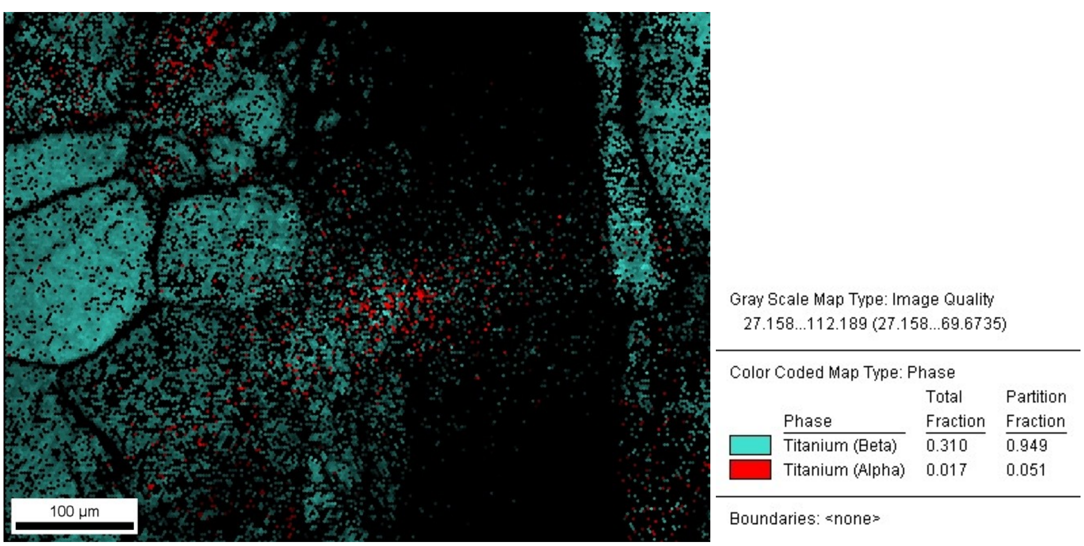

Figure 5-30: Phase map of Ti-5553#15 STA.

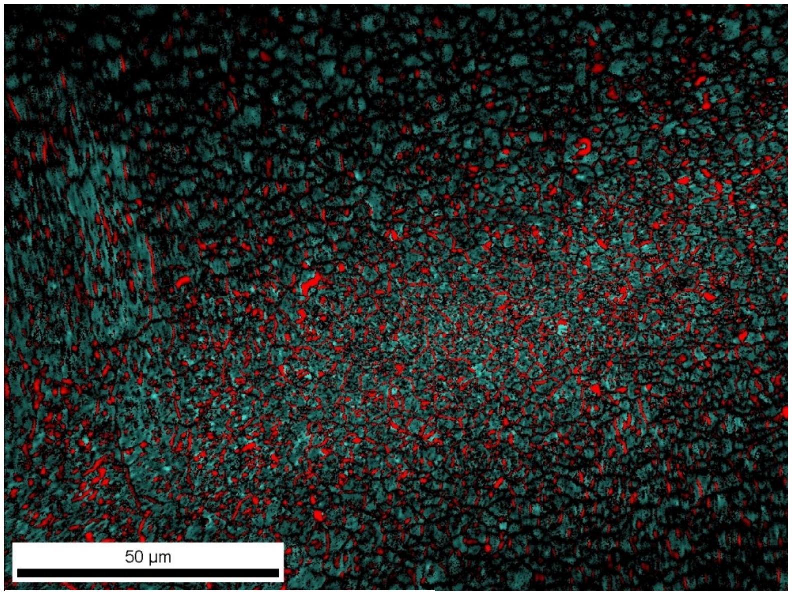

Color Coded Map Type: Phase

	Phase	Total Fraction	Partition Fraction
	Titanium (Beta)	0.410	0.775
	Titanium (Alpha)	0.119	0.225

Figure 5-31: Phase map of Ti-5553#15 (STA). Recrystallized weld zone.

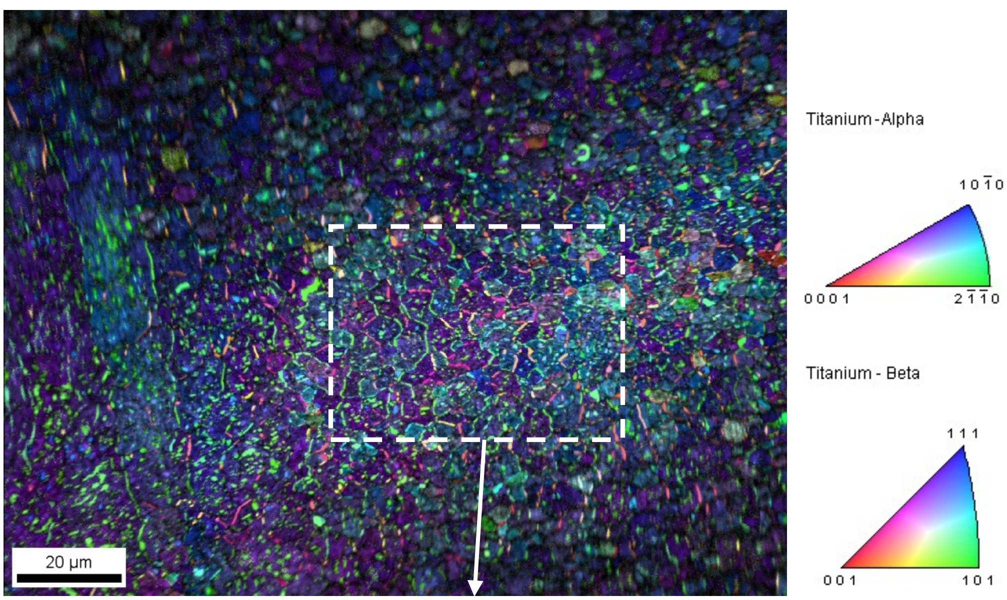

Figure 5-32: Inverse pole figure map of Ti-5553#15 (solution treated and aged after welding). Detail of recrystallized weld zone. Dashed rectangle shows area zoomed in following figure.

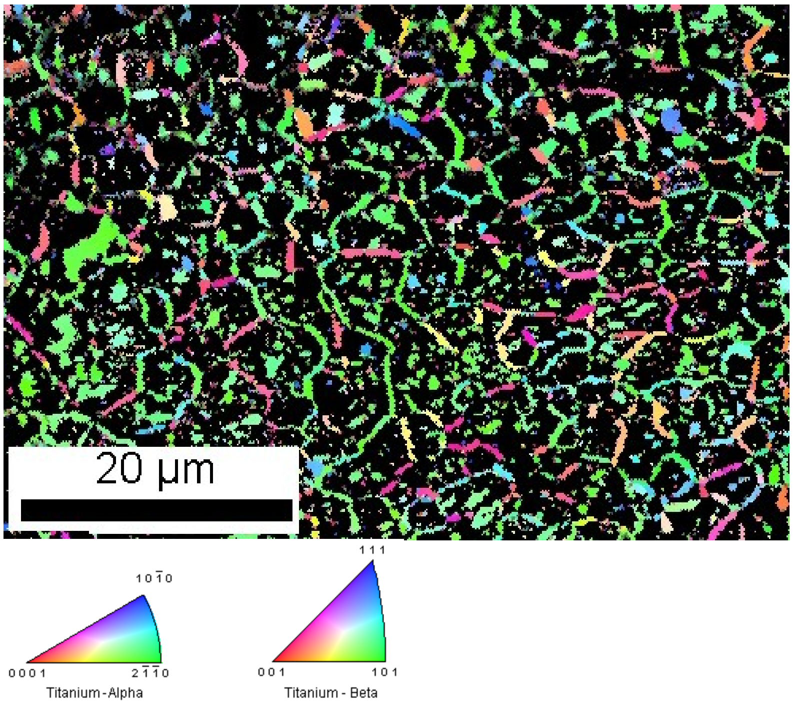

Figure 5-33: α phase only IPF of Ti-5553#15 recrystallized zone.

In Figure 5-34, β pole figures are presented for the recrystallized regions of Ti-5553#3 and Ti-5553#6. No α pole figures are presented due to the negligible amount of α phase observed in the material. The texture intensity of these recrystallized zones can be seen to be very high, approximately 10 to 15 times random. This strong texture is based on a large number of small grains and is quite reliable. As expected from the inverse pole figure maps, most of these recrystallized grains have {110}<111> orientations, where {110} is parallel to the welding plane and <111> to the oscillation direction.

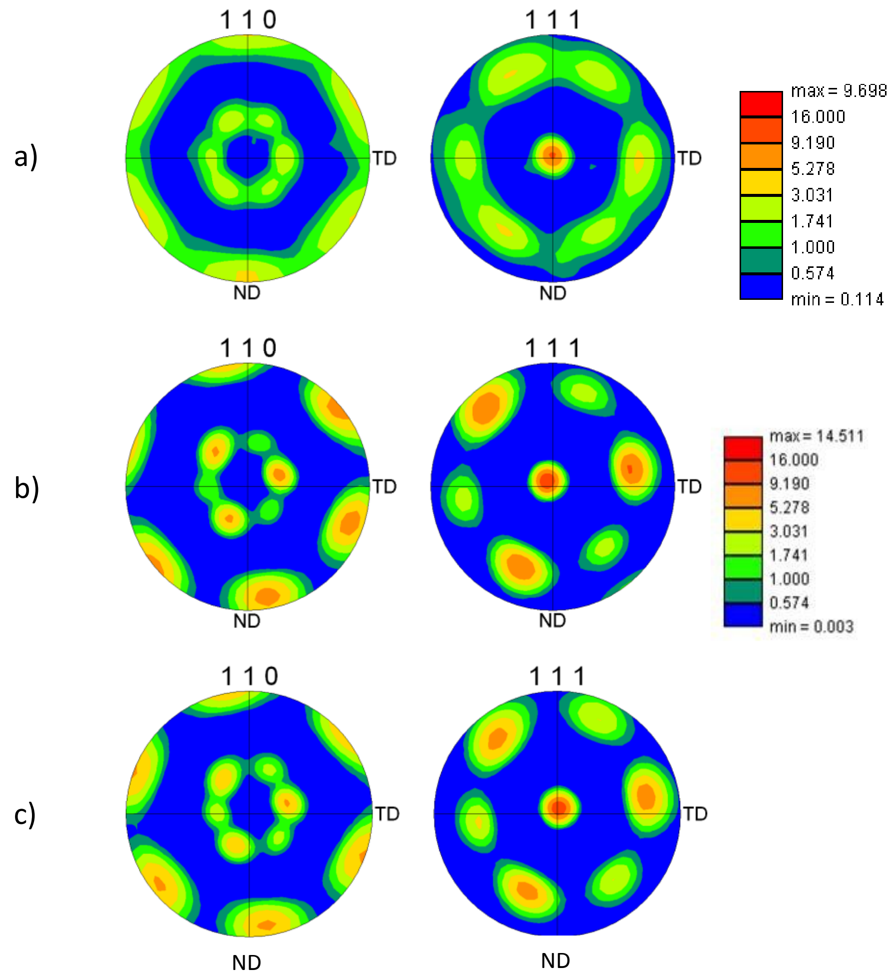

Figure 5-34: β pole figures of the recrystallized zones in (a) Ti-5553#3; (b) Ti-5553#6; (c) Ti-5553#9. Welding direction (WD) is normal to the figure (not shown), Transverse to welding direction is TD, and the direction normal to the welding plane is ND.

Chapter 6

6 Other Materials

In addition to the titanium alloy tests described in detail in the previous chapters, several other materials were linear friction welded as part of the process of understanding the mechanics of the instrument. These welding projects are described only briefly here. For further information the reader is directed to references to published or unpublished reports on these studies, where applicable.

6.1 IMI-834

A third titanium alloy, IMI-834 (Ti-5.8Al-4Sn-3.5Zr-0.7Nb-0.5Mo-0.3Si), was welded under several sets of welding conditions. This alloy falls between Ti-6Al-4V and Ti-5553 in terms of α/β ratio and was received in the forged condition (as opposed to the respectively rolled and ingot starting conditions of the first two titanium alloys). This alloy was not investigated in as much detail as the Ti-6Al-4V and Ti-5553 but some preliminary results are presented below. The parameters and measured and calculated quantities associated with the five conditions tested are tabulated in Table 6-1, while the physical appearance of the welded coupons is shown in Figure 6-1.

Table 6-1: Welding parameters, measured values and calculated values for LFW of IMI-834

	Pressure (MPa)	Freq. f (Hz)	Ampl. a (mm)	Paf (kN/m*s)	Weld time t (s)	Est. Strain Rate (s^{-1})	Est. Strain
IMI-834#1	50	50	2	796	1.1	7.8	8.5
IMI-834#2	70	30	2	668	1.5	4.7	7.1
IMI-834#3	90	50	2	1432	0.8	7.8	6
IMI-834#4	90	30	2	859	1.3	4.7	5.9
IMI-834#5	110	50	2	1751	0.7	7.8	5.6

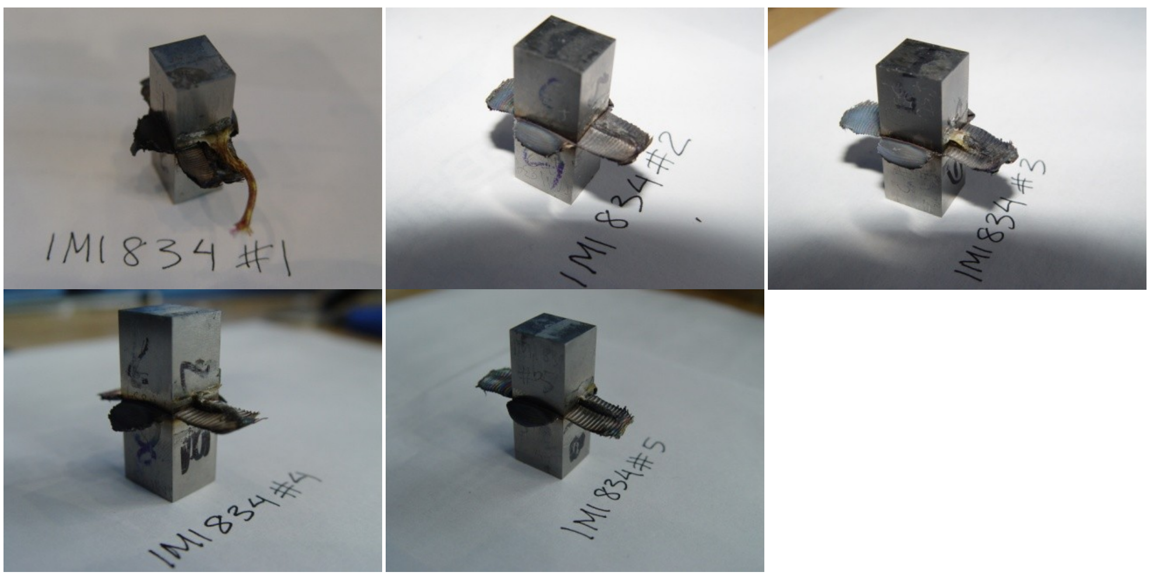

Figure 6-1: LFW'ed IMI-834 coupons.

Due to the large amount of scatter in the microhardness results, the hardening at the weld centres is difficult to observe (see Figure 6-2). However, by comparing sample IMI-834#1, using one of the lowest specific power inputs, with IMI-834#5, using the highest, it can be seen that there is some hardening and that it increases when the axial pressure (and hence SPI) is doubled.

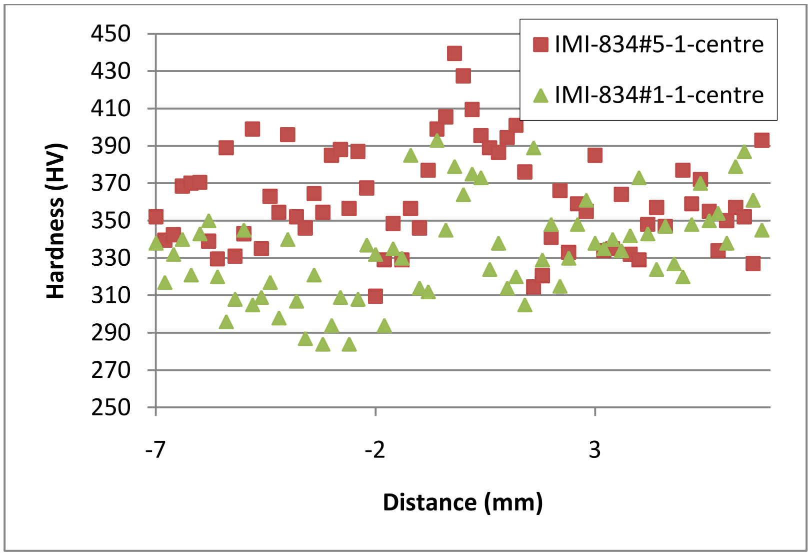

Figure 6-2: Hardness profiles across IMI-834 welds #1 and #5

In the thermal analysis curves shown in Figure 6-3, the start time has been staggered simply in order to make the individual curves easier to see. The thermocouples in both sample #3 and sample #5 broke during oscillation but re-welded themselves almost immediately and continued to gather data. For this reason, the highest value of each of these curves is not reliable. In general, it appears that the highest temperature seen by the thermocouples (at approximately 1 mm from the weld centre, as described in the experimental procedure) is between 750°C and 800°C in each test.

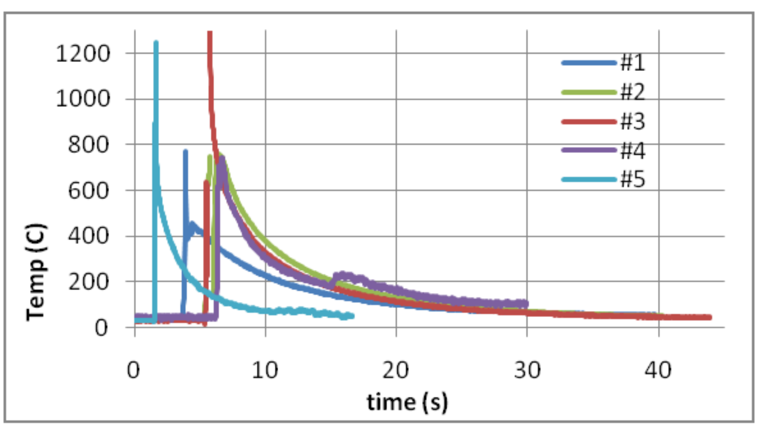

Figure 6-3: Thermal analysis curves collected during LFW of IMI-834.

Figure 6-4 to Figure 6-8 illustrate the microtextures of three selected IMI-834 welds. The three welds were produced at the same frequency (50 Hz) but respectively increasing pressures (50 MPa, 90 MPa, and 110 MPa). In the first sample, IMI-834#1, many twins can be seen, especially in the detail view shown in Figure 6-6. In each of the three samples, a strong texture can be seen in the weld centre. It appears that in the third sample, which was welded using the highest axial pressure, this textured zone occupies a smaller region of the fine-grained zone than in the samples welded at lower pressures. This is consistent with the finding in the Ti-6Al-4V study that the thickness of the affected zone is inversely proportional to axial pressure, frequency of oscillation and amplitude of oscillation (see Figure 7-4, Figure 7-5, and Figure 7-6). The texture is shown as a pole figure in Figure 6-5.

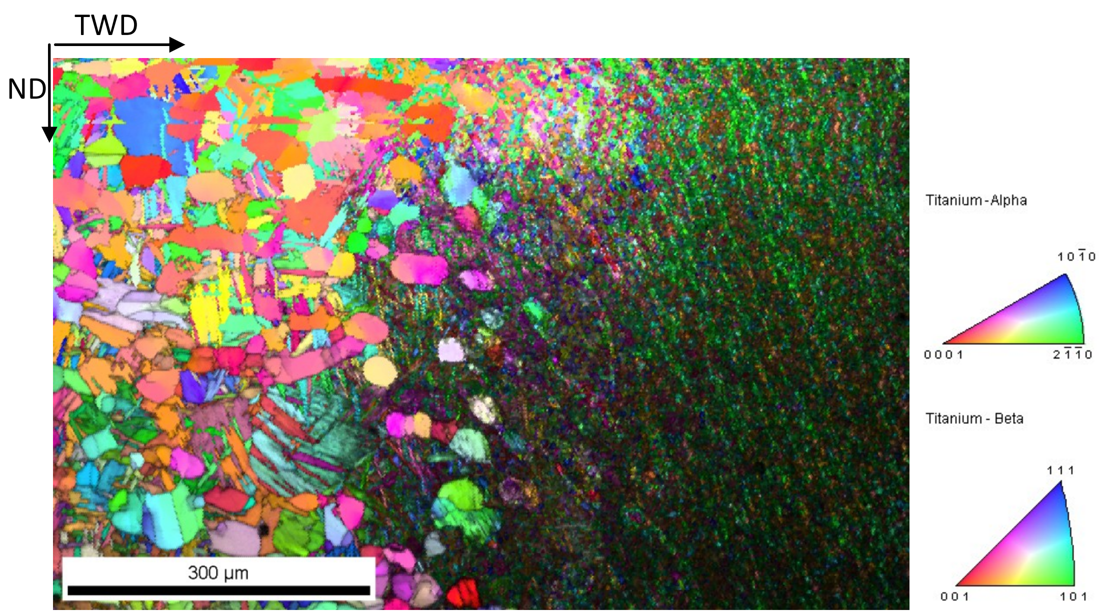

Figure 6-4: EBSD inverse pole figure map of IMI-834#1.

As in the two titanium alloys presented above, this alloy shows a strong basal texture in the direction normal to the weld plane, while the prismatic pole figure also displays a strong texture with peaks in the transverse direction and approximately 30° from the oscillation direction.

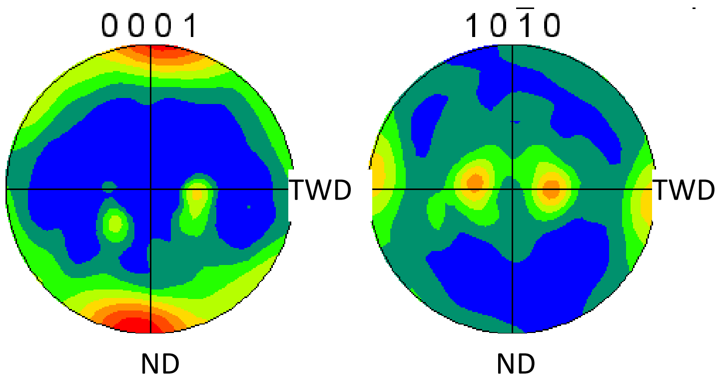

Figure 6-5: Pole figures representing the fine-grained weld zone of IMI-834#5.

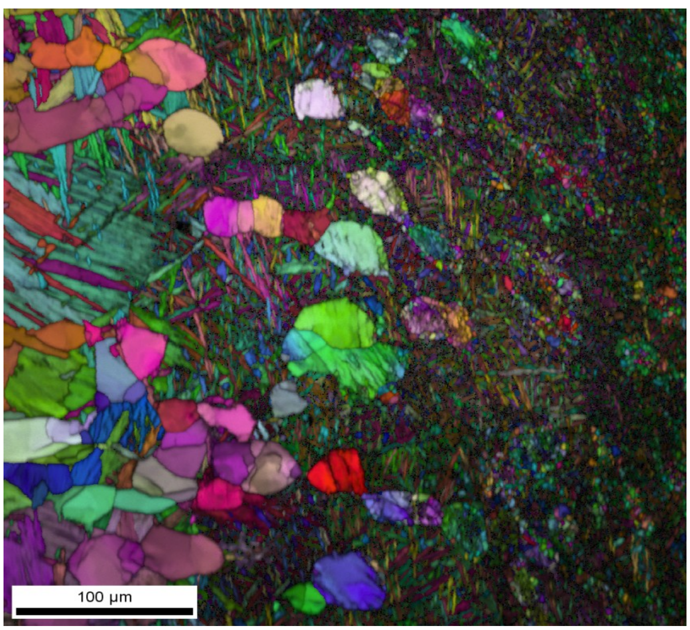

Figure 6-6: EBSD inverse pole figure map with image quality map overlaid; IMI-834#1, at higher magnification and with a smaller step size of 0.5 µm.

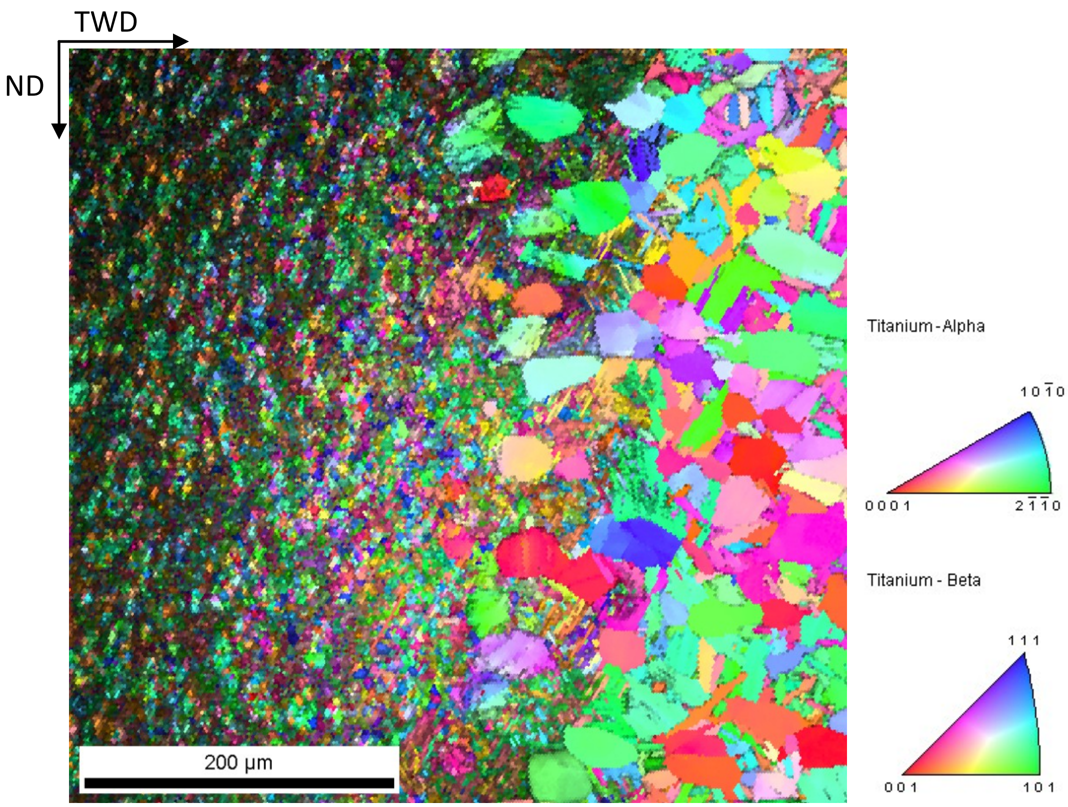

Figure 6-7: EBSD inverse pole figure map of IMI-834#3.

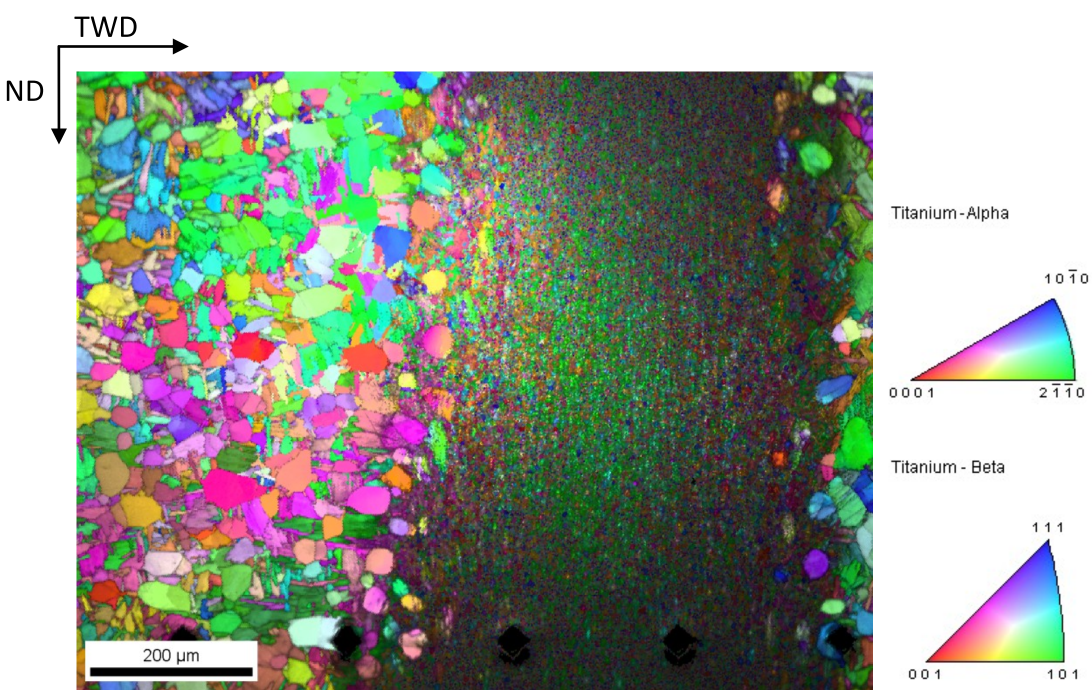

Figure 6-8: EBSD inverse pole figure map of IMI#5 across the weld.

6.2 Single crystal Ni-based superalloy

The LFW of single crystal Ni-based superalloys involved careful control of the orientation of the samples as they were placed in the holder. To ensure consistent welding results, the majority of the rods were ground as shown in Figure 6-9 such that the [011] direction of each crystal, which was determined from the literature to be the ideal oscillation direction for LFW [16], was correctly oriented. Some rods were ground such that the [011] direction was inclined at a 22.5° angle to the oscillation direction. These rod pairs were then positioned for welding such that the delta between their [011] directions was a total of 45°. These rod pairs were not welded successfully. No amount of oscillation caused a bond to form, although some flash was extruded.

The physical appearance of the successfully welded rods is presented in Figure 6-10. It can be seen that the flash emerges split, unlike the combined flash seen in titanium alloys. Through the manipulation of the weld parameters, the centre zone, which initially contained a relatively large region of recrystallized grains, was reduced to a very few grains. However, the dendrites that formed during the growth of the single crystal, can be seen in Figure 6-11 to have flowed in two opposite directions, i.e. in *both* oscillation directions. Nonetheless, as shown in Figure 6-12 , tensile testing confirmed that the weld was not a weak point in the structure.

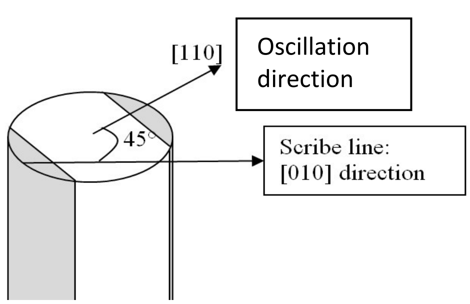

Figure 6-9: Schematic of the direction of oscillation (and hence clamping flats to be machined) with respect to the crystal orientation.

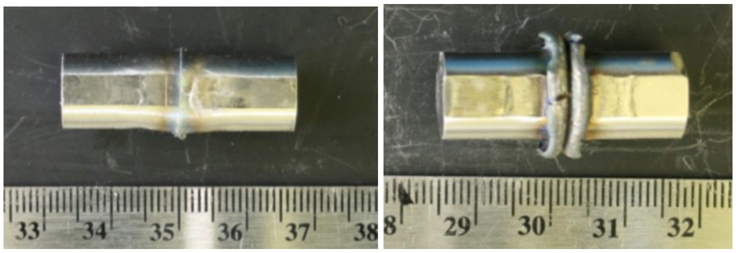

Figure 6-10: CMSX-4 linear friction welded (a) unsuccessfully and (b) successfully (note substantial flash).

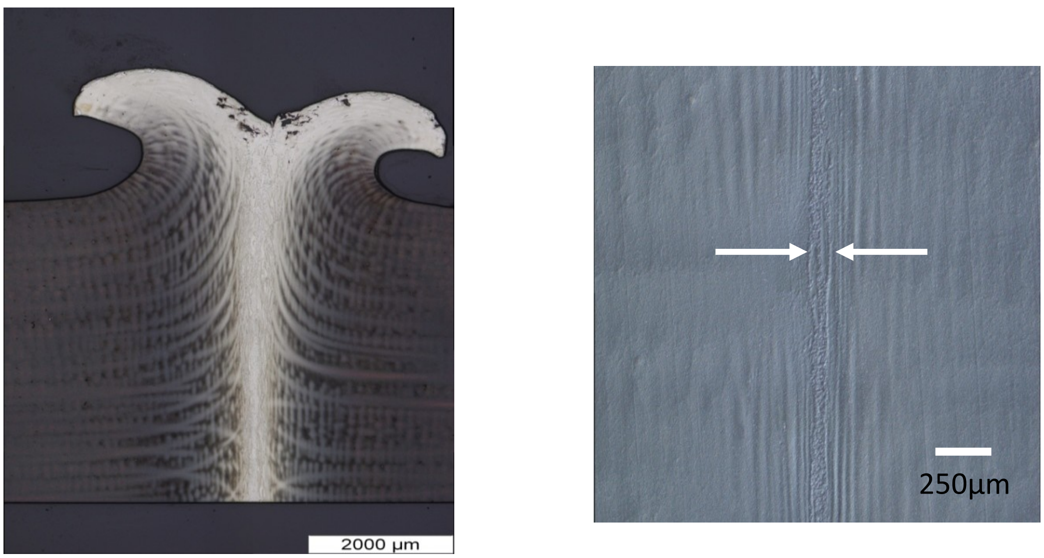

Figure 6-11: Optical etched micrographs of LFW CMSX-4 samples showing dendrites curving in both oscillation directions and small recrystallized zone.

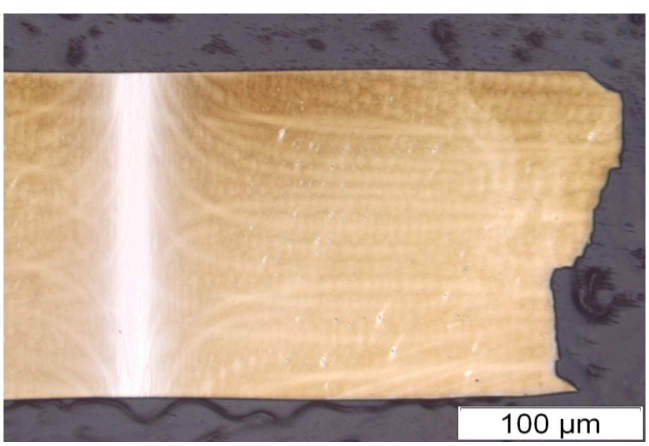

Figure 6-12: Fractured tensile sample from LFW CMSX-4 specimen.

6.3 Aluminum-copper dissimilar welding

An extensive project was undertaken aimed at evaluating the suitability of LFW for producing bi-metal electrical connectors [23, 24]. The AA6063–Cu connectors produced in this way were found to be in general of comparable quality to the industry-standard explosively welded connectors. In some respects (such as the volume of intermetallic compounds produced at the interface), the LFW connectors were vastly improved (Figure 6-13).

In these joints formed from two dissimilar materials, it was found that the deformation and material plasticization was concentrated in the material with the lower melting point, i.e. the aluminum alloy. The flash formed was almost exclusively AA6063, with only scattered particles of Cu included. Despite the one-sidedness of the material softening, the bonds formed were very strong and appeared to have minimal defects mainly consisting of intermetallic compounds. These compounds, however, did not form a continuous layer at the interface and in some cases did not appear at all, so were considered to have a relatively low impact on the conductivity of the connectors.

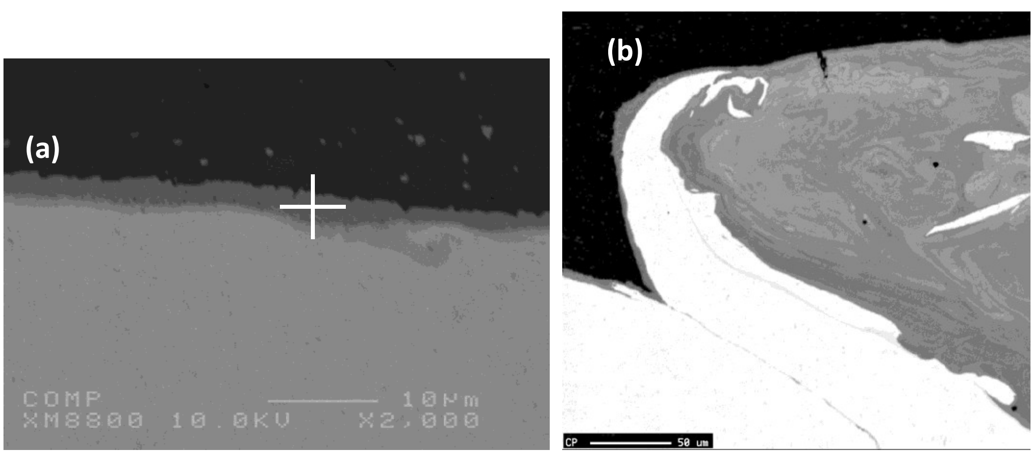

Figure 6-13: BSE images of (a) LFW AA6063-Cu connector and (b) explosively welded Al alloy-Cu connector; note that the magnification in (b) is five times that in (a).

Chapter 7

7 Discussion

Ti-6Al-4V has been the subject of more linear friction welding studies than any other single material due to the material's prevalence in compressor blades and the development of LFW as an alternative manufacturing technique for these parts. Despite this, there are still many areas that have not been fully explored. Models are being developed to attempt to explain the thermal and deformation effects imposed on the material during welding [33, 65-67] but as yet there are no definitive answers as to exactly what temperatures and strains are experienced by each region within and surrounding the weld interface. It is to be hoped that the techniques employed in this study will add significantly to the understanding of this process, both with respect to Ti-6Al-4V and more generally.

Ti-5Al-5V-5Mo-3Cr, a much more recently developed alloy, has not been studied at all in conjunction with the linear friction welding method. As a near-β alloy, it behaves quite differently from Ti-6Al-4V in some respects; however, both alloys are composed primarily of titanium and both contain α and β phases. At the temperatures attained during linear friction welding, both would appear to exceed the β transus and undergo deformation in the β phase. Clearly, some of the knowledge that applies to Ti-6Al-4V can assist in understanding the linear friction welding of Ti-5553. This alloy was welded using the same MTS LFW process development system employed in the Ti-6Al-4V work described above. As in the first part of the work, the process conditions were varied in order to examine the relationship between the process parameters and the microstructural, textural and mechanical properties.

7.1 Strain and Strain Rate

In LFW, the maximum deformation that the material is exposed to will depend on the distance traveled from the opposite ends of oscillation. This deformation occurs in half a cycle, so the strain rate can be estimated using an average velocity (amplitude x frequency) over the total length travelled, as shown in Eq. 7.1 [27].

$$\dot{\varepsilon} = \frac{\partial \varepsilon}{\partial t} = \frac{2a/L}{2/f} \qquad \text{(Eq. 7.1)}$$

where a is the amplitude of oscillation, L is the length of the specimen and f the frequency of oscillation. This strain is distributed in the sample according to the schematic shown in Figure 7-1. Naturally, a simple equation such as Eq. 2.2 cannot fully describe the complexity of the system or the components of the strain along different axes. As this work did not focus on modelling this process, however, this estimate is used with the understanding that it is, indeed, only an estimate, and a rough one at that. In reality, in the plastic section at the interface, the strain rate is affected by the rate at which material is ejected from the interface into the flash as well as the oscillation velocity. The former in turn is dependent on the rate at which axial shortening occurs, which is specified only indirectly in terms of the axial pressure. The actual shortening rate depends on the resistance of the plastic material to being compressed and ejected towards the flash. Thus an equation or model incorporating the axial pressure as well would more accurately reflect the actual strain rate. This type of problem is frequently analyzed using finite element (FEM) methods.

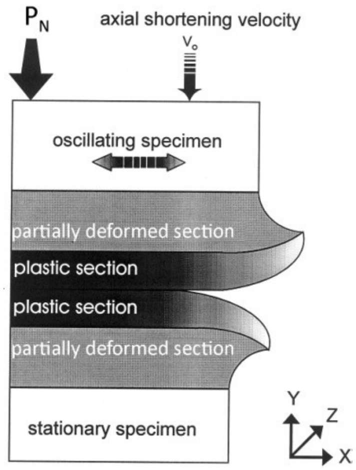

Figure 7-1: Material flow model [32]

The overall strain can nevertheless be estimated using the measured welding time in conjunction with the estimated average strain rate. The strains and strain rates calculated for the Ti-6Al-4V specimens welded in this study were presented above in Table 4-1.

In the case of the Ti-6Al-4V, the calculated maximum strains and strain rates greatly exceeded the literature values of 0.7 and 0.5 s^{-1} required to initiate dynamic recrystallization in Ti-6Al-4V at temperatures exceeding the β transus [68]. Previous studies [6, 30] have found that the temperature at the weld interface during LFW rises above the β transus temperature (approximately 996°C) for the experimental range considered in this work. It is therefore reasonable to assume that the strain and strain rate required to provoke dynamic recrystallization during the LFW of this alloy are similar to the literature case and that dynamic recrystallization took place as a result. It is clear upon examination of the microstructures in Figure 4-18, as well as the EBSD images in Figure 4-43 and Figure 4-44 that the predicted recrystallization had indeed occurred in the centre zone of the weld interface. These images display a fine-grained weld centre bordered by a region of deformed grains, which in turn is bordered by a region of apparently unaffected grains.

Another study [69] found that at strain rates higher than 10^{-1} s^{-1} in the α + β range, Ti-6Al-4V exhibited flow instabilities manifested as adiabatic shear bands, which caused cracking. The lack of any apparent shear bands or cracks in the LFWed specimens leads to the conclusion that the deformed region reached the β temperature range. The same source found that the dynamic recrystallization of Ti-6Al-4V in the β phase occurs at about 1100 °C and in the strain rate range 10^{-3}–10^{-1} s^{-1}, which again has been almost certainly attained or even exceeded in this case.

In a similar manner, the Ti-5553 alloy exhibited recrystallization in the weld zone for all successful linear friction welds [70]. Literature data on the deformation behaviour of this alloy is somewhat sparse but it has been reported [9] that, at strains > 0.35, dynamic recovery of the β phase is the dominant deformation mechanism. With a starting structure matching the material used in this study (see Figure 7-2), forging Ti-5553 at 835°C (below the transus) leads to little to no flow softening, with steady-state flow being achieved almost directly after yielding. The grain refinement seen in the weld centre in the LFWed Ti-5553 alloys may be a result of dynamic recrystallization rather than dynamic recovery, despite the findings of Jones et. al [9]. Dynamic recrystallization is quite effective in grain refinement when deformation takes place at a high strain rate and a relatively low temperature (i.e. at a relatively high Zener-Hollomon parameter, see Eq. 7.2) [71]. It has been found in past studies [71] that dynamic recrystallization does not occur in titanium alloys during α + β deformation; this once again supports the hypothesis that the weld centre experienced super-transus temperatures, while the adjoining TMAZ did not, since the former had undergone recrystallization and the latter had not.

$$Z = \dot{\varepsilon} \exp (Q/RT) \qquad \text{(Eq. 7.2)}$$

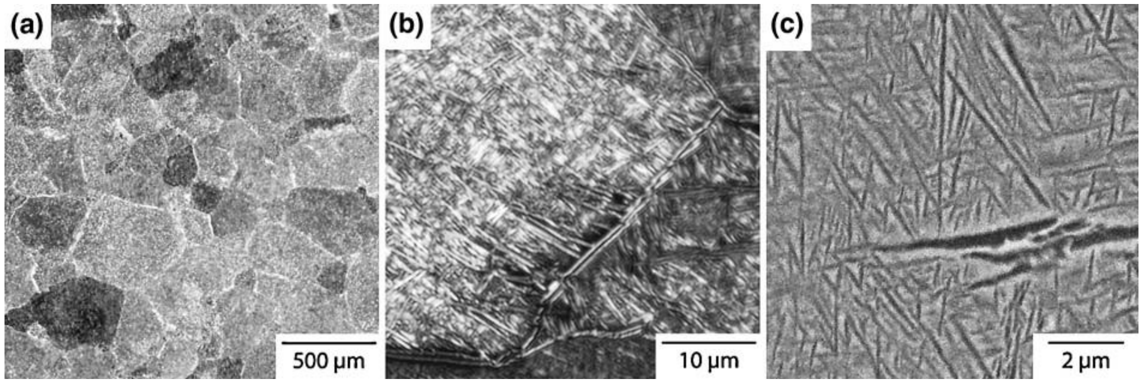

Figure 7-2: Micrographs of the Ti-5553 following β forging and slow cooling, showing (a) parent β grain structure, (b) grain boundary α phase, and (c) BSE micrograph of the fine Widmanstätten microstructure within the prior β grains [9].

7.2 Influence of Flow Characteristics on Welding Behaviour and Flash Character

Thermomechanical processing can be used to control microstructural, textural and mechanical properties. Dislocation density and stored energy are dependent on deformation and annealing, while the grain size and texture are controlled by recrystallization [72]. In ductile crystalline materials, the flow stress is dependent on the average dislocation density and the evolution of dislocation structure during deformation.

The greatest hardening effect provided by deformation is observed in single-phase Ti alloys, both α and β phase. With increasing volume fraction of the β phase in α + β alloys, the hardening effect of cold work diminishes and can only be observed at the onset of deformation. In addition, when no phase transformation occurs during deformation, the hardening effect is at its lowest [73]. Given the much larger fraction of the β phase in Ti-5553 versus Ti-6Al-4V, it is clear that work hardening should be a much less important mechanism in the former. In terms of flash shape, this would lead to a softer material being extruded, which helps to explain the vertical spread of the flash as compared with the thin, elongated layer in the Ti-6Al-4V.

A large body of work has been carried out to relate constitutive equations to the hot deformation behaviour in order to model this behaviour [74, 75]. It is common in such work to try to fit the flow characteristics of a material to an expression such as Eq. 7.3 [76].

$$\dot{\varepsilon} = k\sigma^n \exp\left(-\frac{Q}{RT}\right) \qquad \text{(Eq. 7.3)}$$

It is convenient to rearrange the equation into the form:

$$\ln\sigma = \left[\frac{\ln(\dot{\varepsilon}/k)}{\mathrm{n}}\right] + \left[\frac{\mathrm{Q}}{\mathrm{R{\cdot}n}}\right]\frac{1}{\mathrm{T}} \qquad \text{(Eq. 7.4)}$$

so that for a given strain rate, ln σ can be plotted as a straight line vs. 1/T.

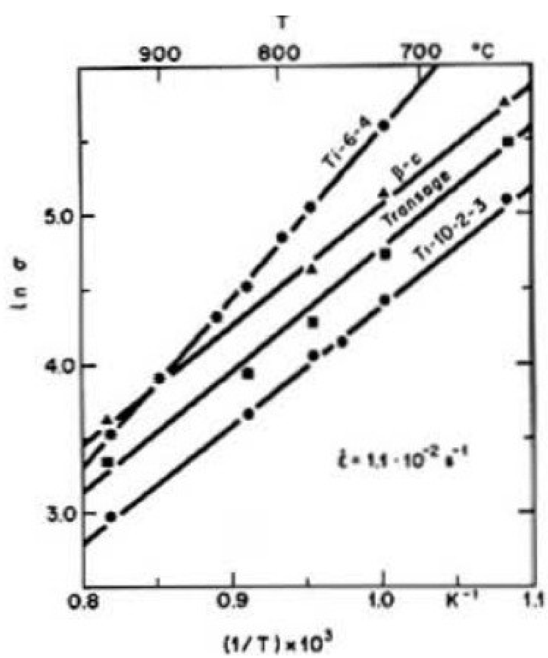

Figure 7-3: Flow stresses of four Ti alloys at $\dot{\varepsilon}$ =1.1x10^{-2} and ε=0.5 [76].

For an investigation into multiple strain rates at a constant temperature, on the other hand, ln σ at a given ε and T can be plotted vs ln $\dot{\varepsilon}$. If the relationship expressed by Eq. 7.3 applies, straight lines will result, with slopes m = 1/n [76].

Although Ti-5553 does not appear in Figure 7-3, a similar alloy, Ti-10-2-3, can be seen to have a significantly lower flow stress at any given temperature than Ti-6Al-4V. Once again, this is in agreement with the observation that the near-β alloy produces flash that is thicker than that produced by Ti-6Al-4V, the α+β alloy.

It has been stated in the literature that, in strain rate sensitive materials such as Ti-6Al-4V, there are two effects that control the extrusion rate: i) the temperature at the interface; and ii) the viscoplastic strain rate [32]. It can be added that, in addition to the extrusion rate, the extrusion time plays an important role in determining the size of the final flash. Although several authors have studied (and modeled) flash development in inertial, or rotational, friction welding [77, 78], very little has been written about the LFW flash morphology.

7.3 Specific Power Input Expression and Beyond

While the rate at which the temperature rises is closely related to the process parameters, the ultimate temperature reached is controlled by the fundamental characteristics of the material. This is because the work of friction that provides the increase in temperature decreases as the material becomes more and more plastic. Thus the process is self-regulating.

The heat generated by the welding process can be described in terms of the fundamental properties of the material. Specifically, the shear stress τ in MPa developed at the oscillating interface will be:

$$\tau = \mu P_N \qquad \text{(Eq. 7.5)}$$

where μ is the friction coefficient and P_N is the normal pressure in MPa. Then the heat generated per unit time and per unit of cross-section (q) can be expressed as:

$$q = \tau v \qquad \text{(Eq. 7.6)}$$

where v is the mean velocity in m/s and q is expressed in $J/s/m^2$ [32].

Combining Eq. 7.6 with the expression for (average) velocity as amplitude x frequency and substituting the value of τ from Eq. 7.5, we obtain

$$q = \mu P_N f a \qquad \text{(Eq. 7.7)}$$

where f is frequency in s^{-1}, a is amplitude in m, and q is expressed in $J/s/m^2$.

Eq. 7.7 has a clear resemblance to the Specific Power Input relationship described in section 2.2.3 and specifically in Eq. 2.2.

$$w\ (kW/m^2) = a*f*F/2\pi*A \qquad \text{(Eq. 2.2)}$$

Using the calculated value of q in conjunction with the measured weld thickness, a relationship was observed in this work. The dependence of weld thickness on specific heat input *rate*, or q, is shown graphically in Figure 7-4.

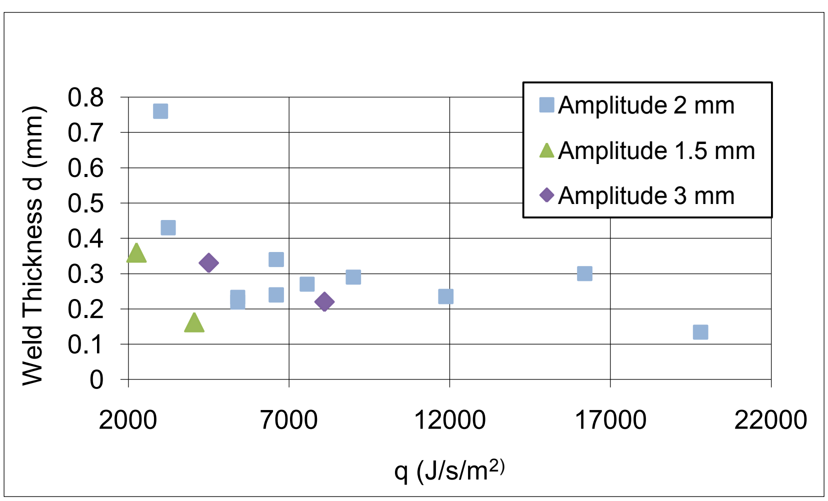

Figure 7-4: Weld thickness *d* as a function of specific heat input rate *q* for three amplitudes.

The dependence of the weld thickness on the individual weld parameters frequency and axial pressure is shown in Figure 7-5 and Figure 7-6. The axially applied pressure is seen to have a greater influence on the weld thickness than does the frequency, as was also seen in the last column of Table 4-1 above. While there is a general narrowing trend as the specific power input (proportional to the product of pressure and frequency) is increased, the sample with the highest pressure, but not the highest specific power input, has the narrowest weld. The thickness of the weld is closely related to the energy-density as well: a higher energy-density allows more rapid heating of the weld interface; the latter in turn leads to a shorter time over which the weld region is at high temperature.

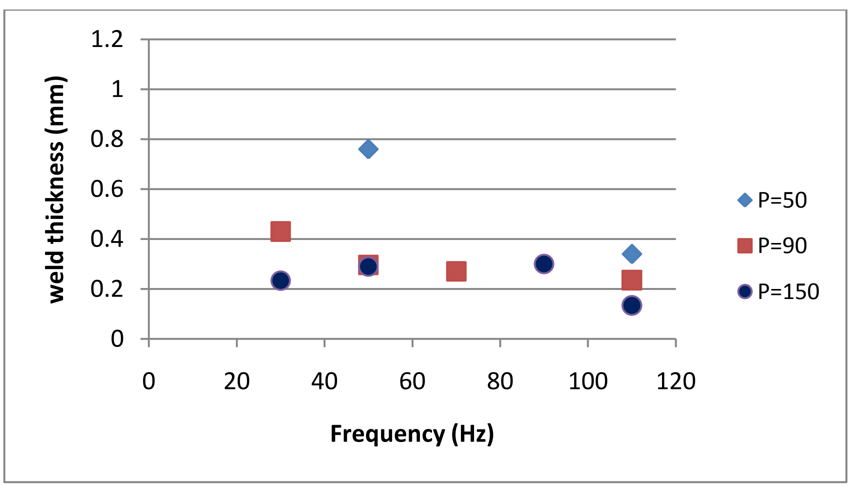

Figure 7-5: Weld thickness as a function of frequency, for three axial pressures.

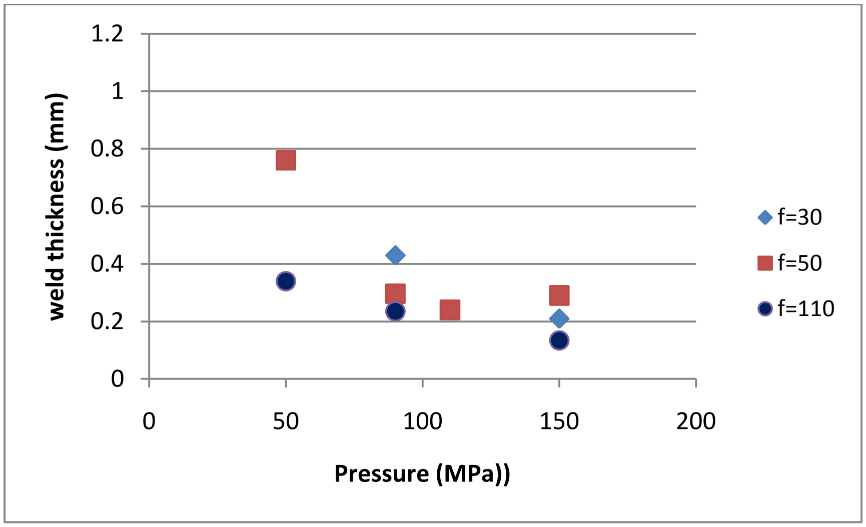

Figure 7-6: Weld thickness as a function of pressure, for three frequencies.

Intuitively, if the time of welding is left as a dependent variable and weld completion is defined by an upset distance, the welding time must depend on both the upset distance chosen and the rate of heat input. The t vs. q plot in Figure 7-7 indicates that t decreases as some exponent of q, which is illustrated in log-log form in Figure 7-8. In this plot, the time dependence on specific heat input rate seems to be consistent for all sets of welding conditions tested.

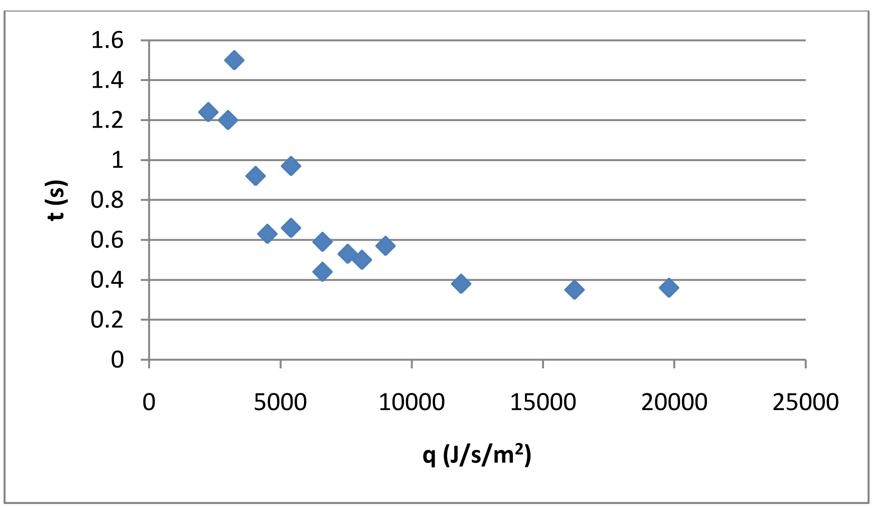

Figure 7-7: Weld time as a function of specific heat input rate.

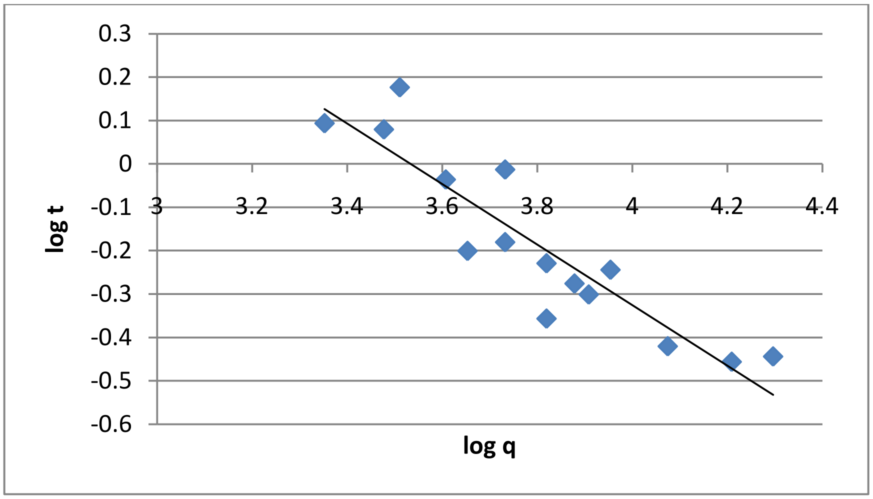

Figure 7-8: The dependence of weld time t on specific heat input rate q.

The weld thickness can also be related to weld time, since naturally the amount of heat input into the weld interface is a function of how long oscillation occurs. A plot of measured weld thickness vs. measured oscillation time is presented in Figure 7-9. The trend line has been forced to pass through the origin due to the logical conclusion that if there is no oscillation, there can be no weld thickness. This plot is not as convincing as those depicting the dependence of time and weld thickness on specific heat input rate, thus there is probably a factor missing from this relationship.

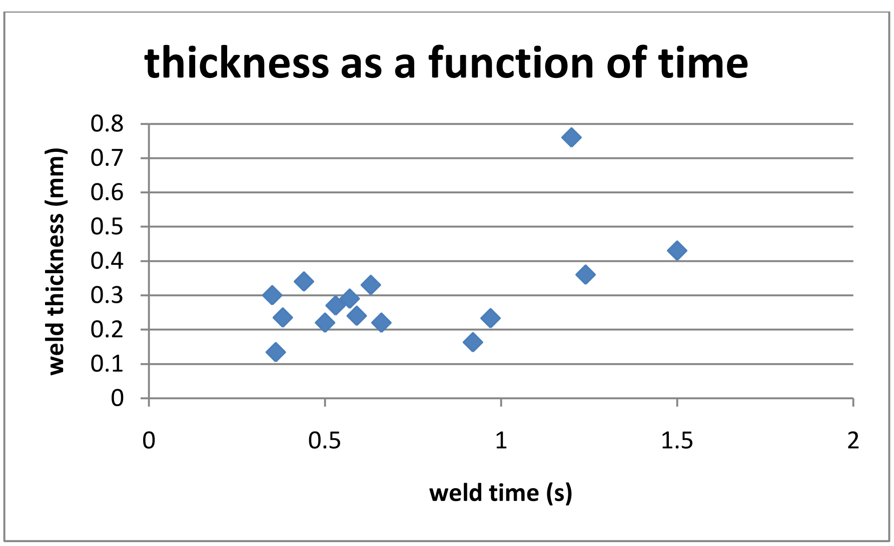

Figure 7-9: Weld thickness as a function of duration of oscillation for Ti-6Al-4V.

To extend the idea of the specific power input equation, it is possible to calculate the *total* heat generated Q during the full time of oscillation from the axial pressure, amplitude, frequency, and measured quantities of time and weld thickness. In other words:

$$Q\,(J) = \mu P_N \cdot af/\ell \cdot t \cdot (\text{relevant volume}). \qquad \text{(Eq. 7.8)}$$

Here Q is expressed in Joules and should not be confused with lower case q, the specific heat input rate. For simplicity, the volume involved is defined here as A x d, where d is the thickness of the weld zone. The deformation in as well as the heat absorbing capacity of the HAZ are ignored in this simplified estimate. ℓ is the 'gauge length' for the shear deformation that produces the heat. It refers to the asperity height and is assumed to remain fixed [79].

On simplifying, this gives:

$$Q/A = \mu P_N \times af/\ell \times dt. \qquad \text{(Eq.7.9)}$$

It can be assumed to a first approximation that $\mu = 0.6$ and that ℓ is constant (although unknown). Since d and t have been measured, the total heat input for the welded area during the time of oscillation, Q, can be evaluated in units of $1/\ell$. The calculated values are tabulated in Table 7-1.

Table 7-1: Total heat input Q calculated for different weld conditions.

Weld ID	Axial Pressure P (MPa)	Frequency f (s^{-1})	Amplitude A (mm)	Q * ℓ (J·m)	Weld thickness d (mm)
1	50	50	2	0.80	0.76
3	90	30	2	0.57	0.43
9	90	50	2	0.11	0.22
11	110	50	2	0.12	0.24
15	90	70	2	0.15	0.27
24, 28	150	50	2	0.21	0.29
26, 30	90	110	2	0.15	0.235
40	150	110	2	0.13	0.134
42	150	90	2	0.24	0.3
44	50	110	2	0.14	0.34
46	150	30	2	0.17	0.233
32	90	50	1.5	0.09	0.163
36	50	50	1.5	0.14	0.36
34	90	50	3	0.12	0.22
38	50	50	3	0.13	0.33

7.4 Heat Conduction

A preliminary attempt to calculate the actual temperature at the interface for the Ti-6Al-4V welds can be made using a one-dimensional heat conduction model [80], as shown in Eq. 7.10. It is important to keep in mind that there is almost certainly a cap on heat input rate *q*, which is based on frictionally generated heat and can only continue for as long as there *is* friction, i.e. until the plasticized material begins to melt. This limit is in a sense automatically accounted for in the following equation by the *time* element, which is experimentally determined and the magnitude of which is dependent on the welding process.

$$T(x,t) - T_0 = \frac{2q_0\sqrt{\frac{\alpha t}{\pi}}}{\lambda}\exp\left(-\frac{x^2}{4at}\right) - \frac{q_0 x}{\lambda}\left(1 - erf\left(\frac{x}{2\sqrt{\alpha t}}\right)\right) \text{ [80]} \qquad \text{(Eq. 7.10)}$$

Here T_0 is the initial temperature, taken as 25°C (298 K); q_0 is taken as 5000 kJ/s/m^2, (this is calculated using Eq. 7.7 with 50 MPa pressure, 50 Hz frequency, and 2 mm amplitude); α is the thermal diffusivity 2.87X10^{-6} m^{2}s^{-1}; λ is the thermal conductivity of the material, 6.70 W/m·K; t is taken as 1 second, since equilibrium is assumed to have been reached by that time; and x is the distance from the interface in m.

Note that the thermal diffusivity is calculated in this case using Eq. 7.11 below. A simplifying assumption that the diffusivity does not change with temperature is used for this first approximation.

$$\alpha = \frac{\lambda}{\rho C_p} \qquad \text{(Eq. 7.11)}$$

Here the thermal diffusivity α is in m^2/s; the thermal conductivity λ (at room temperature) is in W/(m·°K); the density ρ in kg/m^3; and the specific heat capacity C_p in J/(kg·°K).

The temperature calculated using this method for a distance 1 mm from the weld interface at 1 second from the start of oscillation is 828 °C vs. the measured value of 862°C for the Ti-6Al-4V weld in question (from Table 4-2). However, the temperature calculated for 10 mm from the interface is back to room temperature, 25°C, in contrast to the 214°C measured using a thermocouple. Despite this discrepancy in the 10 mm calculation, the heat transfer equation appears to be useful as a first approximation of the temperature close to the interface, and thus was used to generate an estimate of the temperature right next to the interface. The results are plotted in Figure 7-10, and indicate that the interface temperature may be as high as 1200° during equilibrium welding. Since thermocouple measurements were not attempted for the Ti-5553 material, the validity of this approach for this material could not be verified, and thus was not performed.

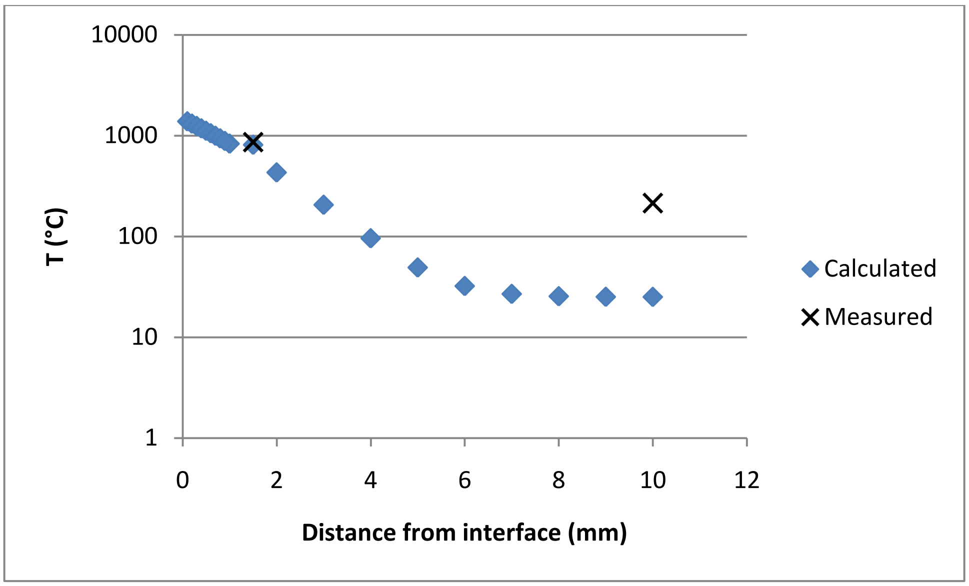

Figure 7-10: Calculated and measured temperatures in Ti-6Al-4V during LFW.

7.5 Microstructures

As described in Chapter 4, the as-received Ti-6Al-4V contained a banded structure of macrozones approximately 50 to 150 µm in width (see Figure 4-14). One band consisted of equiaxed α with transformed β grains containing lamellae of α and β. The other contained α grains with grain boundary β.

The as-received Ti-5553 (Figure 5-1) displayed a large equiaxed β grain structure of about 100 to 500 µm diameter grains. These grains contained an acicular substructure. In comparing the two materials (Figure 7-11), it can be seen that both have two component microstructures, consisting of large features (rolling bands in the former, β grains in the latter) as well as smaller features (grains in the Ti-6Al-4V, an acicular substructure in the Ti-5553).

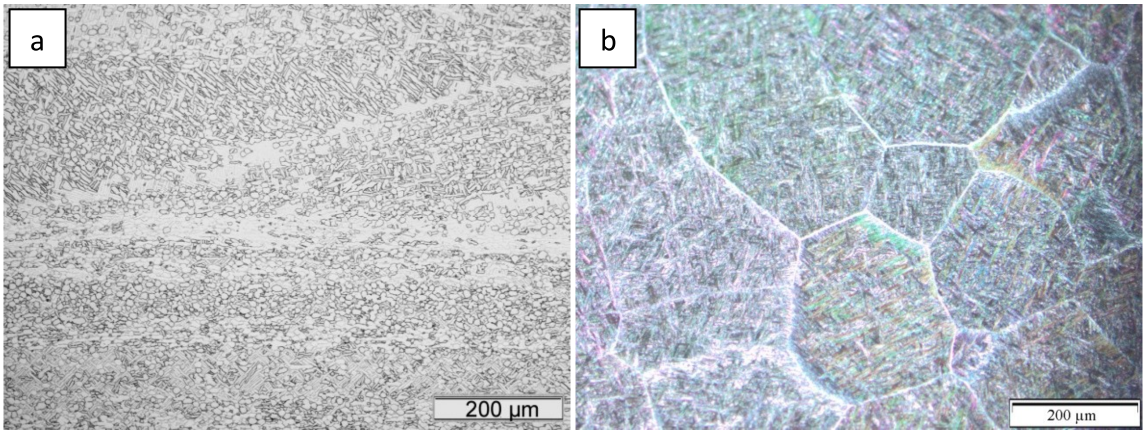

Figure 7-11: Optically revealed (etched) microstructures of (a) Ti-6Al-4V and (b) Ti-5553, both in the as-received condition.

After welding, the microstructures in and near the weld interfaces were severely affected, creating several new zones in the specimens. A martensitic structure was present in the centre of the Ti-6Al-4V welds, as revealed with Kroll's etch under the optical microscope and as shown in Figure 4-15b. This was confirmed with the aid of backscattered electron images from the SEM. The needles were approximately 5 to 7 µm in length and under 0.5 µm in width.

Adjacent to this martensitic region in the Ti-6Al-4V specimens, deformed grains are visible at some distance from the weld centre line (Figure 4-17). The total thickness of the fine-grained weld zone varies from 0.75 mm for the samples welded at 50 MPa and 50 Hz to less than 0.2 mm for those welded at 150 MPa and 110 Hz. Continuing away from the weld centre past the deformed grains, equiaxed grains are visible, indicating a total thickness of the TMAZ of 1.5 mm for the samples welded at 50 MPa, 50 Hz. Samples welded at higher pressure and lower frequency, but overall higher specific power input, had narrower weld regions, as seen in Figure 4-18 to Figure 4-28.

In the case of the Ti-5553, very little can be seen in the weld centre using optical microscopy despite etching attempts (Figure 5-3a, b). Some faint indications of fine equiaxed grains are visible but only intermittently. For this reason, discussion of the Ti-5553 weld centre and TMAZ microstructure in this study is based on the EBSD scans rather than the optical micrographs.

7.6 Microtexture

The pole figures obtained from the Ti-6Al-4V (Figure 4-33) show that the as-received material has a typical rolled titanium alloy texture, with strong basal texture components in the directions normal and transverse to the rolling direction. This texture matched that predicted in the literature [41] fairly closely for a hexagonal material with a c/a ratio less than the theoretical ideal of 1.663. The α phase of titanium has a c/a ratio of 1.587.

The α volume fraction estimated in the as-received Ti-5553 using EBSD was 3.4%. This α phase was distributed at grain boundaries and was not strongly textured. The β phase did not display a strong texture either, which is normal in a material that has not been subjected to any thermomechanical processing. It is important to note that this alloy would not normally be used in the un-heat-treated condition. Like most β titanium alloys, its strength is optimized using careful thermal treatments to achieve the α volume fraction and α particle morphology desired.

7.6.1 Textures in the welded Ti-6Al-4V

The textures obtained from the Ti-6Al-4V samples welded at 50 MPa and 50 Hz (see the pole figures in Figure 4-39 and Figure 4-40) reveal that, from the TMAZ towards the parent material, the texture is essentially that of the as-received material. No textural difference was observed between the parallel-welded and perpendicular-welded specimens. From the TMAZ towards the weld centre, however, there are some textural changes. The Ti-6Al-4V textures in the three zones depicted in Figure 4-41 are distinct, although they are rather weak. The first column of Figure 4-41, representing the apparently unaffected grains in zone (i) adjacent to the TMAZ, looks much as would be expected, in that the pole figures resemble those for the parent material, Figure 4-33. This finding confirms that these grains not only *appear* unaffected in the micrographs but are *crystallographically* unchanged as well. These pole figures display strong textures in some cases (e.g. #3 and #11) but not all. The strong textures closely resemble the as-received pole figures, as expected. Those that have less pronounced textures (e.g. #15) appear to represent a mixture of a) unaffected grains and b) others that have been thermomechanically affected.

Examining the second column of Figure 4-41, which contains the pole figures generated from zone (ii) (the deformed grains between the unaffected zone and the recrystallized zone), it can be seen that there is some resemblance to the original rolled texture but that the peaks are less intense, indicating that a significant percentage of the grain orientations has been altered. These large deformed grains span a region that is only of the order of 10 µm wide; it was therefore difficult to measure their textures separately from those of the adjacent zones.

The basal textures shown in the third column of Figure 4-41, representing zone (iv) (the weld line area), resemble each other quite closely. This supports the idea that this region recrystallized during the welding process, and that the new grains, while inheriting their orientations from the original grains, are also influenced by the shearing forces imposed by the oscillation and friction and the compression imposed by the axially applied force. The prismatic pole figures for the weld line region do vary somewhat but these figures represent very weak textures, with intensity maxima of 2 to 3 times random. Based on the appearance of the weld centre microstructure (see Figure 4-15b), this region is highly martensitic and may have a less pronounced deformation texture than the areas immediately adjacent to the weld.

Comparing the first two rows, representing samples #1 and #3, it would appear that welding at higher pressure (and lower frequency), with an overall higher power/heat input rate, seems to result in the reflection peaks being sharper, indicating a more pronounced texture. This is particularly noticeable in the zone (iv) texture. This agrees with the findings of Lütjering [38], who observed that, while the texture type depends on the deformation temperature, the texture intensity depends on the degree of deformation.

Clearly, in the as-welded condition, the Ti-6Al-4V alloy had undergone complete dynamic recrystallization in the weld zone (200 µm wide) under the thermomechanical conditions employed, namely the combination of straining at elevated temperatures and high strain rates. Beyond the weld region, an abrupt transition to a TMAZ consisting of mixed recrystallized and deformed grains is observed, followed by a further transition to the original large β grains. While the large equiaxed and deformed grains display a variety of orientations, it can be seen that, within the recrystallized zone, the β grains are predominantly oriented with their <111> directions normal to the sample surface. This represents the direction parallel to the weld oscillation direction and in the plane of the weld joint. This re-orientation to a preferred texture is probably due to the alignment during oscillation of the primary slip system in this phase, {110}<111>, with the Burgers vector parallel to the oscillation direction.

7.6.2 Textures in welded Ti-5553

After welding, a very fine-grained (1 to 5 µm diameter) recrystallized zone was observed in the Ti-5553 weld centre (Figure 5-23), ranging in thickness from 240 to 380 µm for the process conditions tested (Figure 5-19, Figure 5-21, and Figure 5-24). These grains consisted exclusively of the β phase, as the α phase was almost entirely missing from the welded structure [81]. Within this recrystallized zone (Figure 5-23), the β grains were almost all oriented with their <111> directions normal to the sample surface, i.e. parallel to the weld oscillation direction. This is attributed to the fact that oscillation was ongoing during the recrystallization process, causing the preferred slip direction of the β phase to become aligned with the oscillation direction. A definite reduction in thickness of the recrystallized zone was observed with increasing specific heat input rate (i.e. from sample Ti-5553#3 to Ti-5553#9), although the number of weld conditions tested was insufficient to determine whether the relationship explored for Ti-6Al-4V (Eq.7.9) holds with this alloy.

The α depletion noted in the weld zone indicates that the fast cooling rate experienced by the material did not permit an equilibrium phase fraction to develop; instead, metastable β was retained in preference to the formation of α. It is worth noting that, based on the accuracy of the TSL OIM Analysis software suggested in the literature [82, 83], points with a confidence index below 0.2 were removed from the data set. It was observed that these points were nearly always indexed as α due perhaps to the large number of lines available in the pattern. Nonetheless, manual examination of the Kikuchi pattern and the index assigned to it led to the conclusion that the indexing was incorrect.

Removing the low confidence index points has the potential to bias the data set. Points not indexed are very likely to be either: in grain boundaries where two (or more) patterns are overlaid; or highly deformed, since heavily deformed material is in general more difficult to index. Since it has been established that the recrystallization occurred while the material was in the β temperature range it can be assumed that within the weld zone there would not be a concentration of deformation in one phase or the other (since only the β phase was present during deformation). Therefore it seems likely that the unindexed or badly indexed points would not belong predominantly to either the β or the α fraction. If this is the case then no bias has been introduced and the remaining points can be considered as representative of the entire dataset.

It has been reported [84] that, in near-β Ti alloys, the mechanical properties are dependent on the size of the α particles. Small α particles like the ones seen in the present work act as typical dispersion-hardening agents. With these fine particles, the α volume fraction controls the ductility. On the other hand, large α particles behave like soft incoherent particles, the volume fraction having little effect on the ductility of the material.

In all samples the TMAZ was observed to consist of large deformed β grains with some recrystallization localized at the grain boundaries; the volume fraction of recrystallized material increased as the recrystallized weld centre was approached. Figure 7-12 shows close-ups of the transition region bordering the recrystallized zone in Ti-5553#3. It can be seen that some of the deformed former β grains have begun to develop subgrain boundaries prior to undergoing recrystallization.

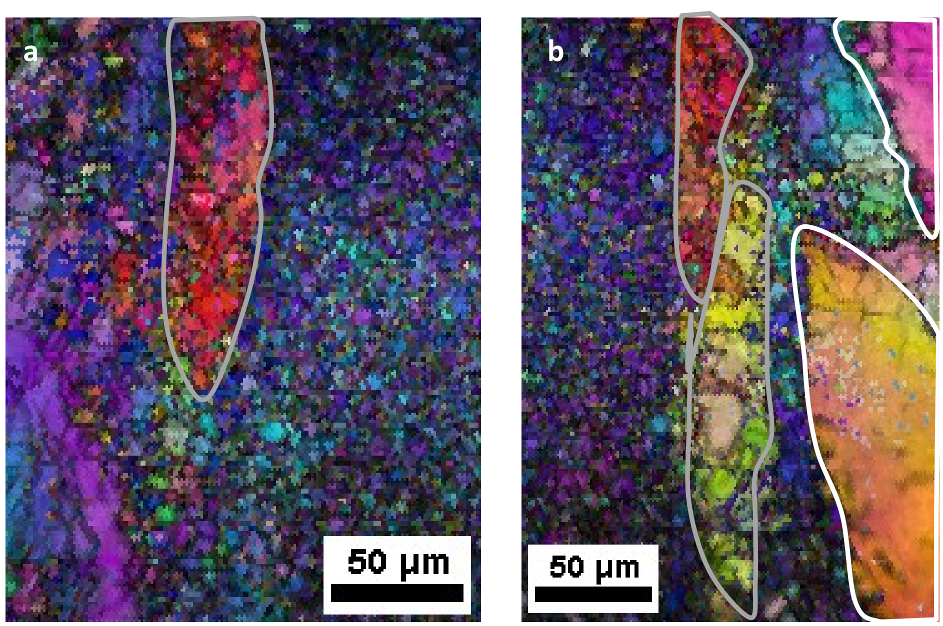

Figure 7-12: Detail of transition between deformed and recrystallized zones in Ti-5553#3: the original deformed grains are outlined in white, while the grains that have begun to break down are outlined in grey; a) left and b) right of the weld centre.

The former β grains remain close to their original orientations (indicated by their colour), in contrast to the adjacent weld zone (appearing mainly blue in these images), where high temperature deformation has caused the new grains to reorient themselves into a consistent texture in response to the oscillations of welding. Regions similar to Figure 7-12 are illustrated in Figure 7-13; these depict sample Ti-5553#9, welded at higher specific heat input rate. In Figure 7-13a, a grain adjacent to the recrystallized zone subjected to a large amount of deformation (high dislocation density) is visible. In Figure 7-13b, a grain that has partially broken down into subgrains can be seen; unlike the Ti-5553#3 example, in this grain there is a large expanse of the original (pinkish-orange) hue, confirming that these weld-adjacent grains containing substructures have retained their original orientations. In the un-heat-treated samples, less than 1% volume fraction of the α phase was observed in the TMAZ and weld zone following welding.

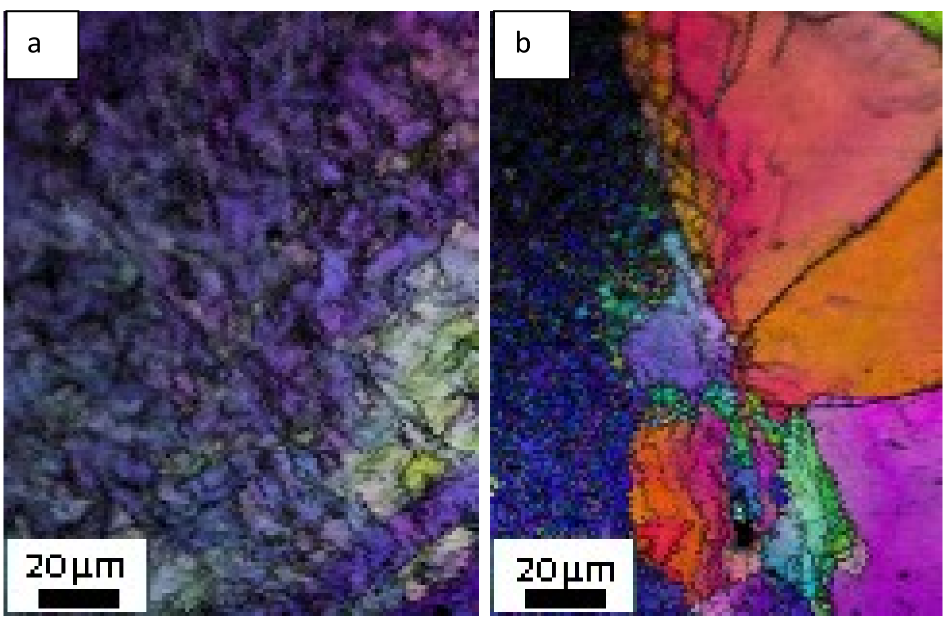

Figure 7-13: Detailed view of the (a) left and (b) right sides of the recrystallized weld zone in Ti-5553#9; EBSD inverse pole figure maps.

In order to examine the alloy in a more useful condition, the heat treatments described earlier were applied to both unwelded and welded specimens. No microtexture was measured on the heat-treated unwelded samples but phase maps for the welded samples revealed a significant increase in α fraction over a similar welded specimen that had not been subjected to heat treatment (Figure 5-20, Figure 5-22, Figure 5-27, and Figure 5-30). Solution treatment alone, as in Ti-5553#14 (Figure 5-27) did not restore much α but solution treatment followed by aging had a dramatic effect on α content and particle morphology. An overview of the TMAZ and weld zone is illustrated in Figure 5-30, with the red regions representing the α phase. A detailed view of the inverse pole figure map of the recrystallized region is presented in Figure 5-32, while Figure 5-33 shows an inverse pole figure map for the α phase only. The α phase has been dramatically restored by comparison with the previous un-aged specimens, and has developed at the new recrystallized β grain boundaries. In some instances, it surrounds the grains entirely. Interestingly, the orientations of these α regions are not all the same, despite the uniformity of the β texture, indicating that several variants must be forming.

7.7 Mechanical Properties

The hardness values reported for the LFWed samples of Ti-6Al-4V in Figure 4-29 and Figure 4-30 and the microstructures of these samples are in agreement with previous findings for material welded under similar conditions. It is clear from the present results that welding parallel versus perpendicular to the rolling direction does not significantly influence either the hardness or the weld microstructure.

In the case of the Ti-5553, rather than a hardening in the weld centre, a drop in hardness was observed. Microhardness profiles (visible in Figure 5-4 and Figure 5-5) revealed a softened area at the weld centre extending 2 mm on either side of the weld centre line. This drop is readily explained by the fact that no post-weld heat treatment (PWHT) was performed on these samples. The solution treatment of Ti-5553 is usually carried out below the β transus, so that some globular α remains, much of it on grain boundaries. Without this treatment, the strengthening and grain boundary pinning effects (as well as the detrimental effect on fracture toughness) of the globular α that would have formed are absent. Although an increase in strength in the weld region might have been possible due to the grain refining effects of heavy deformation combined with recrystallization at elevated temperature, this increase was not observed, perhaps obscured by the greater effect of softening due to the loss of α.

The reduction in tensile strength of the welded samples can be explained by the presence of the softened region in the weldment with a microstructure depleted of α. Also, there is a distinct difference in tensile properties between sample Ti-5553#3, welded using the baseline axial pressure and frequency, and sample Ti-5553#6, welded at higher pressure and lower frequency; the Ti-5553#3 displayed higher YS and UTS as well as greater elongation (see Table 5-2). The better mechanical performance of Ti-5553#3 compared to Ti-5553#6 can be attributed to the decreased amount of material affected thermomechanically (weld zone and TMAZ), as indicated by the microhardness profile.

On the other hand, once heat treatment is introduced, only the elongation values show appreciable degradation in the welded samples, while the UTS and YS are almost identical to those of the as-received heat treated material. This is in keeping with results observed for other materials (see Chapter 4, Ti-6Al-4V), wherein a stronger weld region leads to lower elongation values due to the strain concentration effect when the strength of the material is not constant along its length.

In both as-received and welded specimens, there is a dramatic difference between the ST and the STA conditions. This is borne out in the texture findings, where it can be seen that solution treatment alone does not restore the α volume fraction necessary for strengthening of this alloy. On the other hand, solution treatment and aging does appear to restore the α fraction satisfactorily.

Fracture of the welded specimens during tensile testing occurred in the TMAZ within 1 mm of the recrystallized weld zone. The consistent failure of the welded samples in the TMAZ (rather than in the recrystallized weld centre) is most likely due to a combination of α depletion and the retained (though deformed) coarse microstructure. Although the weld centre is similarly depleted in α, the finer grains make it a less likely location for fracture initiation.

In the weld-free tested samples, the average uniform strain is approximately 12%, rising to about double that at the location of the eventual fracture. The localization is much more pronounced in the welded specimens, with an average strain in the majority of the material of only 2%. This rises sharply to 5% just outside the TMAZ and thence steadily but rapidly to a maximum of 9.3%, almost 5 times the average, at the fracture location adjacent to the weld line.

Both microhardness analysis and tensile evaluation of the welded specimens lead to the conclusion that a softened region exists at and on either side of the weld line. This soft region, depleted of the strengthening α phase, as revealed by the microstructural and textural examinations, represents an area where the strain concentrates. An object is strongest when the strain is evenly distributed over its volume. Here, there is strain concentration caused by the inhomogeneity of the phase distribution and therefore in the flow stress; this results in a local increase in the strain during deformation. Of future interest for welded Ti-5553 components is the use of a post-weld heat treatment to promote precipitation of the strengthening α phase. The present study indicates that a solutionizing and aging cycle would be beneficial in improving the properties of the weld.

Chapter 8

8 Conclusions

1. Oscillating parallel or perpendicular to the rolling direction in the rolled Ti-6Al-4V alloy does not make a difference in terms of post-weld microstructure and texture.

2. For a given material with characteristic thermal conductivity and thermal diffusivity, the welding time (if not explicitly specified in process control) is determined by the upset requested and by the heat input rate. If weld thickness is to be minimized, high heat input rate should be combined with a low welding time. Thus if welding time is not specified but left dependent on the upset distance requested, then the lowest possible upset distance that still produces a sound weld should be chosen.

3. Weld centre temperatures in both titanium alloys surpassed the β transus temperature for the alloy in question and the calculated strains and strain rates exceeded the critical levels required for the initiation of dynamic recrystallization at super-transus temperatures. The microstructures produced in this work are in

agreement with the weld centre temperature estimates based on both temperature measurements and heat transfer calculations.

4. The Ti-6Al-4V weld centre consisted of fine 1 to 5 μm recrystallized grains (revealed by EBSD) containing an apparent martensitic structure (revealed by BSE imaging). The Ti-5553 material also displayed a recrystallized, 1 to 5 μm grain size weld zone. The thicknesses of the recrystallized and TMAZ zones for Ti-6Al-4V were proportional to welding time and inversely proportional to axial pressure, frequency and amplitude of oscillation. Axial pressure was found to have a greater influence on weld thickness than did frequency or amplitude.

5. Hardness and UTS in the recrystallized weld zone increased relative to parent material hardness and UTS for the Ti-6Al-4V but *decreased* relative to the parent material for the as-welded Ti-5553. The hardening in the Ti-6Al-4V is due to grain refinement, while the softening in the Ti-5553 is due to α phase depletion.

6. The flash morphology in the Ti-5553 welded samples does not exhibit the clear traces of oscillation that are present in the Ti-6Al-4V material. This is attributed to the larger number of slip systems in the near-β alloy, and thus to a lower flow stress in the Ti-5553 than in the Ti-6Al-4V at a given temperature and strain rate. This difference is considered to be responsible for the thicker, less elongated flash in the former material.

7. The tensile properties of the Ti-6Al-4V material were not identical along the RD and TD axes. In both the unwelded and welded specimens, the UTS was lower along the RD, averaging 930 MPa, than along the TD, averaging 995 MPa. All the welded specimens fractured in the parent metal at some distance from the welded region.

8. The texture of the Ti-6Al-4V samples in the *deformed zone* between the parent material and the recrystallized weld centre mainly retains the texture of the parent material with some contribution from the new recrystallized grains in this region. Grains in this zone developed subgrain boundaries as they approached the critical level of temperature and deformation for dynamic recrystallization but until the grains actually recrystallized the texture did not change significantly.

9. The texture in the *recrystallized zone* of the Ti-6Al-4V samples is characterized by basal peaks oriented towards the NWD (direction normal to the plane of welding) angled 30° towards the TWD (direction transverse to the welding, or oscillation, direction), as well as basal peaks in the TWD. Weaker components towards the WD (welding, or oscillation, direction) angled ±30° towards the TWD also appear. These textures are all much weaker than those in the parent material and in the deformed (unrecrystallized) zones. The prismatic pole figures for this zone are almost random, displaying very weak peaks of only 2 to 3 times random with no consistent locations from one sample to the next.

10. The microtexture measured in the Ti-5553 weld centre revealed a high concentration of grains with <111> orientations parallel to the oscillation direction. This is attributed to alignment of the preferred <111> slip direction of the β phase with the oscillation direction.

11. The Ti-5553 as-welded samples fractured in the TMAZ within 1 mm of the edge of the recrystallized zone. This is ascribed to the almost complete disappearance of the α phase in the weld zone and TMAZ of the welded samples. Both the weld zone and the TMAZ were weakened by the depletion but the weld zone had the advantage of a finer microstructure, while the TMAZ did not.

12. Applying a *solutionizing* heat treatment to both the as-received and welded Ti-5553 material resulted in lower values for yield strength and ultimate tensile strength but higher elongations. Applying both a *solutionizing* and an *aging* heat treatment resulted in yield strengths and ultimate tensile strengths that were significantly higher than in both the solutionized only and as-received materials; these matched the literature values for this alloy in the heat treated condition. However, the elongation did not improve with heat treatment, due to the inhomogeneity of the properties along the gauge length in the welded samples; this resulted in strain concentration in the weaker regions of the material.

Chapter 9

9 Contributions to Original Science

1. For the first time, a comparison between the linear friction welding of Ti-6Al-4V with the oscillation direction *parallel* to the RD and with the oscillation direction *perpendicular* to the RD was performed. It was determined that the microstructure and texture of the material are similar for these two conditions but that the tensile properties are different.

2. A new heat input expression was developed and a correlation between heat input rate and welding time was discovered.

3. A correlation was observed between the thickness of the weld zone and the welding parameters axial pressure, oscillation frequency, and oscillation amplitude.

4. To the author's knowledge, the near-β titanium alloy Ti-5553 was linear friction welded for the first time.

5. It was discovered that the α phase in Ti-5553 was entirely depleted during welding and that it could not be restored by a solutionizing heat treatment alone.

It was found that solutionizing followed by aging restored the α phase particles necessary for strengthening the material.

6. It was demonstrated that the flash extruded during the welding of Ti-5553 exhibited a morphology that differed from that applicable to the titanium alloys welded previously. It was shown that this is consistent with the bcc type of flow behaviour of this alloy.

7. Texture measurements of linear friction welded Ti-6Al-4V and Ti-5553 have revealed new texture components in the deformed zone of the Ti-6Al-4V and in the recrystallized zone of the Ti-5553. In the texture of the recrystallized zone of the Ti-5553 welded samples, it was shown that the preferred bcc <111> slip direction had become aligned with the oscillation direction for the majority of the grains.

8. For the first time, tensile and microhardness measurements of Ti-5553 linear friction welded samples were performed in both the as-welded and PWHT conditions. It was discovered that the untreated welds were softer and weaker than the unwelded material, but that a solutionizing *and aging* PWHT completely restored the properties of the welded region.

10 References

1. Donachie, M.J.J., *Titanium: a technical guide*. 2nd ed. 2000: ASM International.
2. Merati, A., E. Dalgaard, M. Jahazi, and P. Wanjara, *Mechanical properties of linear friction welded Ti-6Al-4V alloy*, in *XIX International Symposium on Air Breathing Engines 2009 (ISABE 2009)*. 2009, American Institute for Aeronautics and Astronautics (AIAA): Montreal, Canada.
3. Dalgaard, E., M. Jahazi, and J.J. Jonas, *Texture and microstructural evolution during linear friction welding of Ti-6Al-4V*, in *TMS*, R.S. Mishra, M.W. Mahoney, and T.J. Linenert, Editors. 2009, TMS: San Francisco. pp. 55-66.
4. Dalgaard, E., F. Coghe, L. Rabet, M. Jahazi, P. Wanjara, and J.J. Jonas, *Texture evolution in linear friction welded Ti-6Al-4V.* Advanced Materials Research, 2009. **89-91**: pp. 124-129.
5. Karadge, M., M. Preuss, C. Lovell, P.J. Withers, and S. Bray, *Texture development in Ti-6Al-4V linear friction welds.* Mater. Sci. Eng., A, 2007. **459**: pp. 182-191.
6. Wanjara, P. and M. Jahazi, *Linear Friction Welding of Ti-6Al-4V: Processing, Microstructure, and Mechanical-Property Inter-Relationships.* Metall. Mater. Trans. A, 2005. **36A**: pp. 2149-2164.
7. Manufacturing Technology Inc. *Linear Friction Welding*. 2011; Available from: http://www.mtiwelding.com/equipment/1/Linear-Friction-Welding.
8. Thompson Friction Welding. *Linear Friction Welding*. 2011; Available from: http://www.linearfrictionwelding.com.
9. Jones, N., R. Dashwood, D. Dye, and M. Jackson, *The flow behavior and microstructural evolution of Ti-5Al-5Mo-5V-3Cr during subtransus isothermal forging.* Metall. Mater. Trans. A, 2009. **40A**: pp. 1944-1954.
10. Threadgill, P. *Linear Friction Welding Knowledge Summary*. 2007; Available from: http://www.twi.co.uk/content/ksplt001.html.
11. Nicholas, E.D. and W.M. Thomas, *A review of friction processes for aerospace applications.* Int. J. of materials and Product Technology, 1998. **13**(1/2): pp. 45-55.
12. Kallee, S., E.D. Nicholas, and M. Russell, *Friction welding of aero engine components*, in *10th World Conference on Titanium*. 2003: Hamburg, Germany.
13. Godfrey, S., M. Strangwood, and P. Threadgill, *Linear friction welding of a gamma titanium aluminide alloy*, in *SF2M/ONERA conference*. 1996: Paris.
14. Threadgill, P., *The prospects for joining titanium aluminides.* Mater. Sci. Eng., A, 1995. **192/193**: pp. 640-646.
15. Baeslack, W.A., T.F. Broderick, M. Juhas, and H.L. Fraser, *Characterization of solid-phase welds between Ti-6AAl-2Sn-4Zr-2Mo-0.1Si and Ti-13.5Al-21.5Nb titanium aluminide.* Mater. Charact., 1994. **33**: pp. 357-367.
16. Karadge, M., M. Preuss, P.J. Withers, and S. Bray, *Importance of crystal orientation in linear friction joining of single crystal to polycrystalline nickel-based superalloys.* Mater. Sci. Eng., A, 2008. **491**: pp. 446-453.

17. Wanjara, P., E. Dalgaard, J. Gholipour, and J. Larose, *Linear friction welding of a Single Crystal Superalloy*, in *THERMEC*. 2011, TransTech: Quebec City, Quebec, Canada.
18. Wanjara, P., E. Dalgaard, M. Jahazi, N. Piolle, and A. Petiot, "LTR-AMTC-2009-0048: Final report on linear friction welding of Zr702 with 316L stainless steel," Aerospace Manufacturing Technology Centre, National Research Council of Canada, Montreal, 2009.
19. Li, W.-Y., T. Ma, S. Yang, Q. Xu, Y. Zhang, J. Li, and H. Liao, *Effect of friction time on flash shape and axial shortening of linear friction welded 45 steel.* Mater. Lett., 2008. **62**: pp. 293-296.
20. Ma, T., W.-Y. Li, Q. Xu, Y. Zhang, J. Li, S. Yang, and H. Liao, *Microstructure Evolution and Mechanical Properties of Linear Friction Welded 45 Steel Joint.* Adv. Eng. Mater., 2007. **9**(8): pp. 703-707.
21. Wanjara, P., E. Dalgaard, M. Jahazi, and N. Piolle, "LTR-AMTC-2009-0047: Final report on linear friction welding of A42 steel and 316L stainless steel," Aerospace Manufacturing Technology Centre, National Research Council of Canada, Montreal, 2009.
22. Hinkley, D., M. Skinner, and R. Trask, *Advanced linear friction welder bonds aluminum to copper*, in *Americal Welders Society Conference*. 1996: Chicago. pp. 76-77.
23. Wanjara, P., E. Dalgaard, G. Trigo, C. Mandache, G. Comeau, and J.J. Jonas, *Linear friction welding of Al-Cu: part I - process evaluation.* Can. Metall. Q., 2011. **Accepted**.
24. Dalgaard, E., P. Wanjara, G. Trigo, M. Jahazi, G. Comeau, and J.J. Jonas, *Linear friction welding of Al-Cu: part 2 - interfacial characteristics.* Can. Metall. Q., 2011. **Accepted**.
25. Vishwakarma, K., O. Ojo, P. Wanjara, and M. Chaturvedi, *Linear Friction Welding of Allvac® 718 Plus Superalloy*, in *7th International Symposium on Superalloy 718 and Derivatives*. 2010: Pittsburgh, PA.
26. Wilhelm, H., R. Furlan, and K.C. Moloney, *Linear Friction Bonding of Titanium Alloys for Aero-Engine Applications*, in *Titanium '95*. 1996, Institute of Materials: London. pp. 620-627.
27. Vairis, A. and M. Frost, *High frequency linear friction welding of a titanium alloy.* Wear, 1998. **217**(1): pp. 117-131.
28. Rabinowicz, E., *Friction and Wear of Materials*. 1965, New York: John Wiley and Sons.
29. Nicholas, E.D., *Fabricating by Friction.* Engineering, 1985. **225**(4): pp. 254-255.
30. Vairis, A., "High Frequency Linear Friction Welding," Doctor of Philosophy, Mechanical Engineering, Bristol, Bristol, 1997.
31. Hsu, E., P. Wanjara, and M. Jahazi, "Effect of process parameters on linear friction welded Ti-6Al-4V," NRC-IAR-AMTC, Montreal, 2004.
32. Vairis, A. and M. Frost, *On the extrusion stage of linear friction welding of Ti-6Al-4V.* Mater. Sci. Eng., A, 1999. **271**(1): pp. 477-484.

33. Vairis, A. and M. Frost, *Modelling the linear friction welding of titanium blocks.* Mater. Sci. Eng., A, 2000. **292**: pp. 8-17.
34. Sathiya, P., S. Aravindan, and A. Haq, *Mechanical and metallurgical properties of friction welded AISI 304 austenitic stainless steel.* International Journal of Advanced Manufacturing Technology, 2003. **26**: pp. 505-511.
35. Wanjara, P., C. Booth-Morrison, E. Hsu, and M. Jahazi. *Process optimization for linear friction welding of Ti6Al4V*. in *Trends in Welding Research*. 2005. Pine Mountain, Georgia, USA: ASM International.
36. Weiss, I. and S.L. Semiatin, *Thermomechanical processing of alpha titanium alloys - an overview.* Mater. Sci. Eng., A, 1999. **263**: pp. 243-256.
37. Germain, L., "Contribution à l'études des hétérogénéités de texture des billettes d'IMI 834," Docteur, Ecole Doctorale Energie Mécanique Matériaux, l'Université Paul Verlaine de Metz, Metz, 2005.
38. Lütjering, G. and J.C. WIlliams, *Titanium*. 2003, Berlin: Springer-Verlag.
39. Mateo, A., M. Corzo, M. Anglada, J. Mendez, P. Villechaise, J.-P. Ferte, and O. Roder, *Welding repair by linear friction in titanium alloys.* Mater. Sci. Technol., 2009. **25**(7): pp. 905-913.
40. Partridge, P.G., *The crystallography and deformation modes of hexagonal close-packed metals.* Metall. Reviews, 1967. **12**: pp. 169-194.
41. Kocks, U.F., C.N. Tomé, and H.-R. Wenk, *Texture and anisotropy: preferred orientations in polycrystals and their effect on materials properties*. 1998, Cambridge: Cambridge University Press.
42. Panza-Giota, R., "Ti-5Al-5V-5Mo-3Cr after solution heat treatment and ageing in the alpha-beta range," Doctor of Philosophy, Materials Science Engineering, McMaster University, Hamilton, 2006.
43. Glavicic, M.G., B.B. Bartha, S.K. Jha, and C.J. Szczepanski, *The origins of microtexture in duplex Ti alloys.* Mater. Sci. Eng., A, 2009. **513-514**: pp. 325-328.
44. Stanford, N. and P. Bate, *Crystallographic variant selection in Ti-6Al-4V.* Acta Mater., 2004. **52**: pp. 5215-5224.
45. Gey, N., H. Humbert, and H. Moustafid, *Study of the α->β phase transformation of a Ti-6Al-4V sheet by means of texture change.* Scripta Mater., 2000. **42**: pp. 525-530.
46. Lütjering, G., *Influence of processing on microstructure and mechanical properties of (alpha + beta) titanium alloys.* Mater. Sci. Eng., A, 1998. **243**: pp. 32-45.
47. Dillamore, I.L. and W.T. Roberts, *Preferred orientation in wrought and annealed materials.* Metall. Reviews, 1965. **10**(39): pp. 271-380.
48. Schechtman, D. and D. Brandon, *Orientation dependent slip in polycrystalline titanium.* J. Mater. Sci., 1973. **8**: pp. 1233-1237.
49. Boyer, R., *An overview on the use of titanium in the aerospace industry.* Mater. Sci. Eng., A, 1996. **213**: pp. 103-114.
50. Attallah, M., M. Preuss, and S. Bray, *Microstructural Development during Linear Friction Welding of Titanium Alloys*, in *Trends in Welding Research, Proceedings of the 8th International Conference*. 2009, ASM International. pp. 486-491.

51. Clyne, T. *DoITPoMS Micrograph Library, University of Cambridge*. 2001; Available from: http://www.doitpoms.ac.uk/miclib/full_record.php?id=54.
52. MatWeb. *TIMET TIMETAL 834*. 2010; Available from: http://www.matweb.com/search/DataSheet.aspx?MatGUID=e5ed359418914348a1146ac55acd2a35&ckck=1.
53. Jahazi, M., *Note regarding IMI834.* personal communication to E. Dalgaard; 2011.
54. Kostrivas, T., L. Smith, and M. Gittos, *Sustained load cracking of titanium alloy weldments*, in *24th International Conference on Offshore Mechanics and Arctic Engineering (OMAE 2005)*. 2005: Halkidiki, Greece.
55. Boyer, R. and R. Briggs, *The Use of β Titanium Alloys in the Aerospace Industry.* J. Mater. Eng. Perform., 2005. **14**(6): pp. 681-685.
56. Nyakana, S., J. Fanning, and R. Boyer, *Quick Reference Guide for β Titanium Alloys in the 00s.* J. Mater. Eng. Perform., 2005. **14**(6): pp. 799-811.
57. Musi, D., *An Update on Properties and Applications for Ti-5Al-5Mo-5V-3Cr*, in *The 21st Annual ITA Conference & Exhibition*. 2005: Scottsdale, AZ.
58. Fanning, C., *Properties of TIMETAL 555 (Ti-5Al-5Mo-5V-3Cr-0.6Fe).* J. Mater. Eng. Perform., 2005. **14**(6): pp. 788-792.
59. Mary, C. and M. Jahazi, *Multi-Scale Analysis of IN-718 Microstructure Evolution During Linear Friction Welding.* Adv. Eng. Mater., 2008. **10**(6): pp. 573-578.
60. MTS, *MTS Operation Manual: Linear friction welding process development system*. 2003.
61. Oliver, W.C. and G.M. Pharr, *An improved technique for determining hardness and elastic modulus using load and displacement sensing indentation experiments.* J. Mater. Res., 1992. **7**(6): pp. 1564-1583.
62. Chromik, R., R. Vinci, S. Allen, and M. Notis, *Nanoindentation measurements on Cu-Sn and Ag-Sn intermetallics formed in Pb-free solder joints.* J. Mater. Res., 2003. **18**(9): pp. 2251-2261.
63. Dalgaard, E., P. Wanjara, J. Gholipour, X. Cao, and J.J. Jonas. *Linear friction welding of Ti-5Al-5V-5Mo-3Cr*. in *Conference of Metallurgists 2010*. 2010. Vancouver, BC.
64. Fischer-Cripps, A., *Nanoindentation*. Mechanical Engineering, ed. F.F. Ling. 2002, New York: Springer-Verlag. 197.
65. Séraline, D., "Finite Element Modeling of the linear friction welding process," Aerospace Manufacturing Technology Centre, 2007.
66. Massimo, M., "Project scope - FEM modeling of the LFW process - phase IV," unpublished.
67. Niu, J., Z. Liu, C. Jin, and G. Zhou, *Numerical computation of a linear friction welding process.* Mater. Sci. Forum, 2008. **575-578**: pp. 811-815.
68. Ding, R., Z. Guo, and A. Wilson, *Microstructural evolution of a Ti–6Al–4V alloy during thermomechanical processing.* Mater. Sci. Eng., A, 2002. **327**: pp. 233-245.
69. Seshacharyulu, T., S.C. Medeiros, W.G. Frazier, and Y.V.R.K. Prasad, *Microstructural mechanisms during hot working of commercial grade Ti-6Al-4V with lamellar starting structure.* Mater. Sci. Eng., A, 2002. **325**: pp. 112-125.

70. Dalgaard, E., P. Wanjara, X. Cao, J. Gholipour, and J.J. Jonas, *Linear friction welding of a near-β titanium alloy.* Acta Mater., 2011. **in press**.
71. Furuhara, T., B. Poorganji, H. Abe, and T. Maki, *Dynamic recovery and recrystallization in titanium alloys by hot deformation.* JOM Journal of the Minerals, Metals and Materials Society, 2007. **59**(1): pp. 64-67.
72. Humphreys, F.J. and M. Hatherly, *Recrystallization and Related Annealing Phenomena, Second Edition*. 2004, Oxford: Elsevier.
73. Moiseyev, V.N., *Titanium alloys: Russian aircraft and aerospace applications*. 2005: Taylor & Francis.
74. Serajzadeh, S. and A.K. Taheri, *Prediction of flow stress at hot working condition.* MeReC, 2003. **30**: pp. 87-93.
75. Mirzadeh, H. and A. Najafizadeh, *Flow stress prediction at hot working conditions.* Mater. Sci. Eng., A, 2010. **527**: pp. 1160-1164.
76. Schroeder, G. and T.W. Duerig, *Forgeability of beta-titanium alloys under isothermal forging conditions*, in *Fifth International Conference on Titanium*, G. Lütjering, Editor. 1985: Munich, Germany. pp. 585-592.
77. Sluzalec, A., *Thermal effects in friction welding.* IJMS, 1990. **32**(6): pp. 467-478.
78. Francis, A. and R.E. Craine, *On a model for frictioning stage in friction welding of thin tubes.* Int. J. Heat Mass Transfer, 1985. **28**(9): pp. 1747-1755.
79. Jonas, J.J., *LFW heat equation.* personal communication to E. Dalgaard; 2009.
80. Li, W.-Y., T. Ma, and S. Yang, *Microstructure evolution and mechanical properties of linear friction welded Ti-5Al-2Sn-2Zr-4Mo-4Cr (Ti17) titanium alloy joints.* Adv. Eng. Mater., 2010. **12**(1-2): pp. 35-43.
81. Dalgaard, E., P. Wanjara, X. Cao, J. Cuddy, A. Birur, and J.J. Jonas. *Effect of heat treatment on linear friction welded Ti-5553*. in *Conference of Metallurgists 2011*. 2011. Montreal, Canada.
82. Draper, U. (2010) *OIM Version 3.0. On-line help.*
83. Sharma, H., S.M.C. van Bohemen, R.H. Petrov, and J. Sietsma, *Three-dimensional analysis of microstructures in titanium.* Acta Mater., 2010. **58**(7): pp. 2399-2407.
84. Hamajima, T., G. Lütjering, and S. Weissman, "Importance of slip mode for dispersion-hardened beta titanium alloys," Air Force Materials Laboratory, Wright-Patterson Air Force Base, Ohio, 1972.